Alma Mater Studiorum – Università di Bologna

DOTTORATO DI RICERCA IN CHIMICA - Ciclo XXXII

Coordinatore: Prof.ssa Domenica Tonelli

Curriculum: Scienze Chimiche - SSD CHIM/03 - SC 03/B1

NOVEL PHOTO- AND ELECTRO-RESPONSIVE SUPRAMOLECULAR SYSTEMS AND MOLECULAR MACHINES

Candidato: Lorenzo CASIMIRO

Relatore: Prof.ssa Serena SILVI

Co-relatore: Prof. Alberto CREDI

Esame finale anno 2020

Abstract

The work presented in this thesis deals with the investigation of new prototypes of light- and electro-activated supermolecules and molecular machines. The discussion will be divided in two main parts.

Part A concerns the exploration of single- and multi-component structures or supramolecular complexes involving light-responsive units.

In **Chapter 1**, novel molecular axles for a light-activated supramolecular pump will be shown. Such molecular motor is based on a pseudorotaxane, whose ring is a crown ether, whereas the axle is composed of an ammonium site, recognition site for crown ethers, linked to a photoswitchable azobenzene unit and to a pseudostopper, which possesses a steric hindrance intermediate between those of the *E* and *Z* isomers of the azobenzene. Such a device is able to unidirectionally move rings along the axle, thanks to the photoswitching of the azobenzene moiety. In order to improve the efficiency of the pump and allow its implementation in more complex structures, the molecular axles have been modified according to three strategies, *i.e.* (i) functionalization of the azobenzene, (ii) examination of different pseudostoppers, (iii) relocation of the ammonium linker in *meta* or *ortho* position on the azobenzene. The photochemical and supramolecular characterization of several axles will be presented, as well as the demonstration of the dissipative operation cycle of the pump. In addition, kinetical simulation will be shown to support the experimental data.

In **Chapter 2**, an example on how the formation of a supramolecular complex affects the photochemical behaviour of a photochrome will be reported. In this study, terarylenes bearing an imidazolium bridge are reported as new guests for crown ethers hosts. Upon irradiation with UV light, the terarylene photochromes undergo isomerization, followed by a very fast thermal cycloreversion reaction. However, complexation of the imidazolium unit by the host stabilizes the closed form, thus demonstrating a supramolecular enhancement of photochromism.

Chapter 3 shows the functionalization of fullerene with either a *para* or *meta* bis-(ethylmalonate)azobenzene derivative. The two malonates attack the fullerene in *equatorial* position, and the configuration of the azo bond changes accordingly. Interestingly, in the case of the *para* derivative, the *Z* isomer becomes the most stable form, whereas in the case of the *meta*, the azobenzene is locked in the *E* isomer and photoisomerization does not occur.

In **Chapter 4**, new single and multicomponent derivatives of dicyanomethylenepyran (DCM) fluorophore will be shown. A thorough investigation of the photoisomerization of the central double bond will be reported for three DCM derivatives. Moreover, the photophysical and photochemical characterization of a mannose scaffold bearing three DCM units will be reported.

Part B concerns the investigation of electro-responsive pseudorotaxanes and rotaxanes.

In **Chapter 5**, new prototypes of calix[6]arene-bipyridinium supermolecules will be investigated. A first study will show the photophysical and photochemical characterization of a diphenylureido-calix[6]arene and of the related pseudorotaxanes and rotaxanes obtained upon inclusion of a bipyridinium-based axle. A second study regards the electrochemical characterization of scorpiand-like pseudorotaxanes and rotaxanes, where the axle engulfed in the cavity is also covalently linked to the calix[6]arene itself.

Contents

Introduction 3

Part A

Chapter 1. Light-driven supramolecular pumps

1.1 Introduction and aim 25

1.2 Azobenzene functionalization: cyanoazobenzene derivatives 30

1.3 Pseudostopper replacement: dimethylbenyl stoppers and pseudostoppers 34

1.4 Pseudostopper replacement: non-symmetrical axles and statistical considerations 40

1.5 Linker relocation: ortho- and meta-derivatives and dissipative behaviour 45

1.6 Dissipative behaviour simulations 51

1.7 Conclusion and perspectives 61

1.8 References 63

Chapter 2. Supramolecular tuning of photochromism in terarylene-based pseudorotaxanes

2.1 Introduction and aim 65

2.2 Photochromism of the isolated axles 67

2.3 [2]Pseudorotaxanes formation 72

2.4 Photochromism of the [2]pseudorotaxanes 74

2.5 Mechanism hypotheses 77

2.6 Conclusion and perspectives 81

2.7 References 82

Chapter 3. Molecular locking of photochromism in azobenzene-derivatized fullerenes

3.1 Introduction and aim 85

3.2 Bis-ethylmalonate derivatives of azobenzene 88

3.2 Photochromism of azobenzene - C_{60} bisadducts 91

3.3 Conclusion 99

3.4 References 100

Chapter 4. Single- and multi-component photochromic and luminescent DCM derivatives

4.1 Introduction and aim 101

4.2 Single component DCM derivatives 103

4.3 Multicomponent DCM derivatives 116

4.4 Conclusion and perspectives 121

4.5 References 122

Part B

Chapter 5. New geometries for calixarene-bipyridinium rotaxanes and pseudorotaxanes

5.1 Introduction and aim 127

5.2 Diphenylureido - calixarenes as hosts for rotaxanes and pseudorotaxanes 130

5.3 Pseudorotaxanes and rotaxanes with scorpiand-like motifs 137

5.4 Conclusion and perspectives 143

5.5 References 144

Conclusion 149

Experimental section 153

Appendix

Appendix A. Dimethylazobenzene as a chemical actinometer i

Appendix B. List of symbols and abbreviations vii

Appendix C. List of publications ix

A brief Jew tale on light xiii

Acknowledgements xv

Introduction

Introduction

Machines and motors at the molecular level: concepts, state of the art and future perspectives

Despite the extremely complex processes and reactions which lie at the basis of life have not been fully understood yet by humankind, the progresses in science and technology in the last century have enabled scientists to discover the molecular building blocks of which all living organism and, eventually, humans themselves, are composed. As a matter of fact, in Nature, most of the fundamental functions are operated by powerful and precise nanometric devices, called *molecular machines*.[1–4] In analogy with their macroscopic counterparts, each component of a molecular machine possesses individual features that ultimately contribute to accomplish a function. Nevertheless, even though this comparison provides a helpful tool to visualize what molecular machines are and why they exist, the physics of such nanoscale devices is substantially different from that of the macroscopic ones. Indeed, at the molecular level, classical forces like gravity or friction are negligible, whereas the motion is governed by viscosity and Brownian motion, *i.e.*, by random fluctuations of the molecules in the medium, itself composed of molecules.[5] Thus, to achieve a good performance, molecular machines must bias the Brownian motion and operate a precise control on the movement, rectifying an erratic behaviour. The most fascinating models of molecular machines can be found in biological systems. For instance, the human body is composed of more than 10000 machines of different degrees of complexity and different functions.[1] Undoubtfully, the most stunning example is the ATP-synthase, a protein assembly engulfed in the mitochondrial membrane, responsible for the synthesis of adenosine triphosphate (ATP).[2,6] Its structure (figure 1) can be schematized as a rotary device composed of two units, a stator (γ) and a rotor. A gradient of pH between the interior of the mitochondrion and the cellular cytosol triggers a flux of H^+ ions, which penetrate the channels of the rotor and are stabilized by anionic receptors. In this way, a rotation of this subunit is caused, which eventually displaces the protons from one compartment of the cell to another, in order to minimize the pH gradient. As a result, the stator moves as well, and deforms the three proteic sites (α and β in figure 1) where ATP is synthesized in a three-step mechanism, as schematized in figure 1. Interestingly, the ATP-synthase can operate in a reversed manner, *i.e.*, if ATP is cleaved, the rotor pumps protons against the pH gradient.

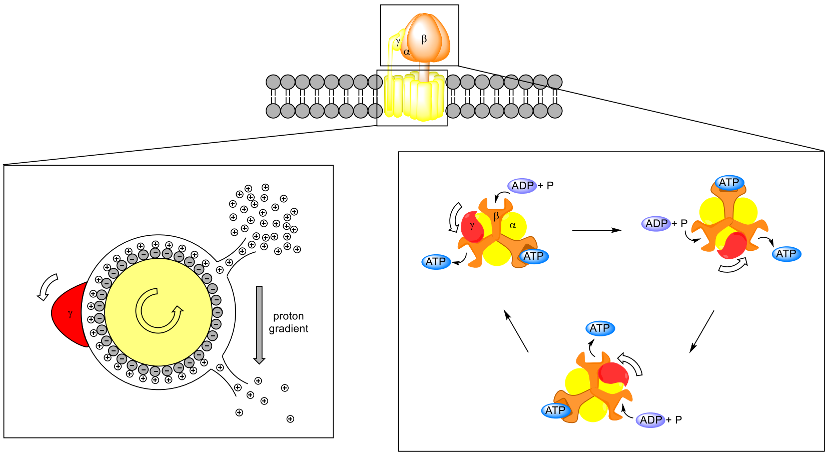

Figure 1: Schematic representation of the working cycle of ATP-synthase. For further information, interested readers can refer to the works of D. Goodsell[2] and of Ballmoos et al.[6]

Other interesting examples of motor proteins are those able to "walk" on cellular microtubules and filaments to carry vesicles, as in the case of kinesines,[7] or to interpenetrate each other to extend or contract the muscular fibres, as for actin and myosin.[8] It must be underlined that, in all these cases, the Brownian motion is not cancelled, but overcome by the overall cooperative effect of the molecular components.

Inspired by the beauty of the natural molecular machines, in the last decades, chemists have begun to design and realize artificial prototypes of molecular machines.[1,5,9–15] In his famous lecture in 1959 "*There's plenty of room at the bottom*", the physicist Richard Feynman foresaw the possibility to exploit molecules to construct manmade operating machines.[16] Nevertheless, only in late 1970s, the first examples of artificial molecular machines began to appear, with the development of the field of *supramolecular chemistry*, pioneered by the Nobel laureate Jean-Marie Lehn.[17–19] Among the first and most investigated fields of supramolecular chemistry, a pivotal role is played by *host-guest* chemistry,[18–25] which deals with supramolecular assemblies, or *supermolecules*, formed by the inclusion of a *guest* molecule into a *host*, namely a cavitand. If the host and the guest possess complementary features, in terms of structure and geometry, a spontaneous assembly occurs between the two, on account of an energetic stabilization related to the formation of the supermolecule.[22,23] The first supermolecules formed according to this approach were based on the recognition between anions or small molecules and cavitands like crown ethers,[25] calixarenes,[26,27] cyclodextrines,[28] cucurbiturils[29] or related compounds. Afterwards, this field grew up continuously, and new examples of hosts and guests eventually formed the basis for the design of the first prototypes of artificial molecular machines.[30] Among the interesting artificial supramolecular architectures reported in the last decades, multicomponent structures with peculiar topologies, like *mechanically interlocked molecules* (*MIM*s), are unquestionably noteworthy.[19,31–34] A great contribution to the study of such supramolecular architectures arose from the development by James Fraser Stoddart of the concept of *mechanical bond*.[33,34] In order to clarify these definitions, a simple supramolecular assembly, called [2]*pseudorotaxane* can be considered (figure 2).

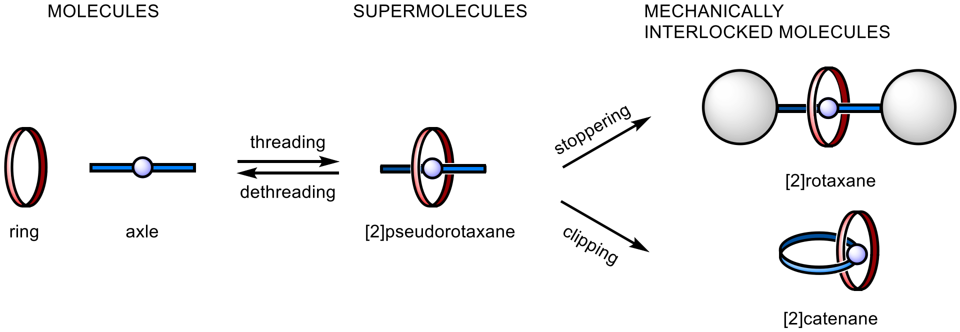

Figure 2: Schematic representation of simple supramolecular systems and mechanically interlocked molecules.

This supermolecule is formed by the insertion of a threadlike component, henceforth called "axle" or "thread", into a cavitand, also called "ring" or "macrocycle". The total number of molecular components is described by the digit in brackets. The threading of the axle into the ring is triggered by the presence of a recognition motif, which stabilizes the interaction between the two components. If the recognition motif is switched off, disassembly takes place, as the supermolecule is not stable anymore (figure 2). Further chemical functionalization can be carried out on the axle: if both the extremities are covalently bound to a hampering group, called "stopper", whose steric hindrance is sufficient to prevent the transit of the ring, a *rotaxane* is formed. In another scenario, if the two extremities of the axle are bound together, a *catenane* is formed. If in the latter two species the recognition site is switched off, the two components cannot be separated. While the supramolecular assembly is an equilibrium process, thus the complexed species coexist with the uncomplexed components, a mechanically interlocked molecule keeps its two components linked together only by means of topology, and they can be separated only by a chemical cleavage of one of them.[31]

So far, a large number of artificial molecular machines have been reported, spanning on several kinds of design and operating features, and most of them are based on supramolecular systems and mechanically interlocked molecules.[1,10–14] Remarkably, the ground-breaking research contributions by James Fraser Stoddart, Jean Pierre Sauvage and Bernard Feringa lead them to the Nobel prize in Chemistry in 2016. Nevertheless, a large number of groups have given important contributions to the field of molecular machines, among whom it is worth mentioning those of Vincenzo Balzani,[35] David Leigh,[36] Takuzo Aida,[37] Makoto Fujita,[38] He Tian,[39] Nathan McClenaghan,[40] Stephen Loeb,[41] Françisco Raymo[42] and Nicolas Giuseppone.[43]

Artificial molecular machines can be defined on the basis of several parameters. Among them, the most important features are:

- The chemical design
- The type of energy supply
- The function performed

Chemical design

As already said, a molecular machine can consist of a single molecule or a supramolecular system. Up to this time, most of the single-molecule artificial molecular machines are based on overcrowded alkenes, and behave as rotary motors thanks to isomerization reactions.[31,44–48] On the other hand, many examples of supramolecular architectures which behave as molecular machines and motors have been reported (*vide infra*).[1,9–11,14] The supramolecular approach is often preferred due to its versatility of design, arising from the great variety of reversible interactions between the components of the supermolecule, which can be even switched off to allow several kinds of movement and, eventually, functions.

Energy supply

In order to perform a function, a power supply must be provided to the device from the exterior. In most of the cases, the action operated by a single input transforms the device from a state into another, and to restore the initial state an opposite input must be sent. Thus, for a complete working cycle, at least two different stimuli must be provided sequentially. Nevertheless, in some cases, a single input can induce both the forward and the backward processes, and the device keeps on operating as long as the energy source is available. Such devices are called *autonomous*.[1,10,14] However, the design of autonomous devices and motors is a challenging task, and, so far, only a few examples of completely autonomous artificial molecular machines have been reported.[35,49–51]

Regarding the nature of the energy supply, three main types of stimuli can be provided to the system, namely chemical, electrical and optical. Even though the kind of input depends on the design of the system, in some instances more than one stimulus can be required. In this case, they must be *orthogonal*, *i.e.*, the outcome of the first must not be cancelled out by the following one(s). Chemical stimulation enables the use of a large number of reactants able to induce a modification on the studied system, but in some case, reaction products will accumulate in the reaction media. All the natural molecular machines work under a chemical stimulus, usually related to a catalytic process, and the waste products are often recycled and involved in other biological processes.[2–4,6,7,52,53] Electrical stimulation can be carried out either by adding a chemical redox species or by applying an electrical potential to the system, which should be endowed with electro-responsive moieties in order to perform a motion.[54] In the case of the application of a redox potential, in principle, the stimulus does not cause the formation of any subproduct. In addition, electrochemistry represents an easy tool to both operate and investigate molecular devices, even in other media than solution, like, for instance, on solid surfaces by means of electron microscopy. Optical stimuli are nowadays the most preferable tools to activate molecular machines. Light is a largely available, renewable and long lasting source of energy, and, as in the case of electrical stimulation, no formation of side products is caused by photons, and the various optical techniques allow both to operate and investigate the device.[15,55]

The most employed photoresponsive moieties in molecular machines are *photochromes* (figure 3). *Photochromism* indicates the reversible transformation of a molecule between two forms having two different absorption spectra.[56,57] These two forms are usually isomers, that can be obtained via double bond photoisomerization, bond photocleavages or photocycloadditions. The photochromic molecules can be grouped into two main classes, *i.e.*, P-type and T-type photochromes. P-type (photochemical-type) photochromes, like diarylethenes[58] and fulgides can be interconverted between the two forms only upon light irradiation, whereas, T-type (thermal-type) photochromes, like azobenzenes,[59] stilbenes and spiropyrans, can revert to the initial form even at room temperature.

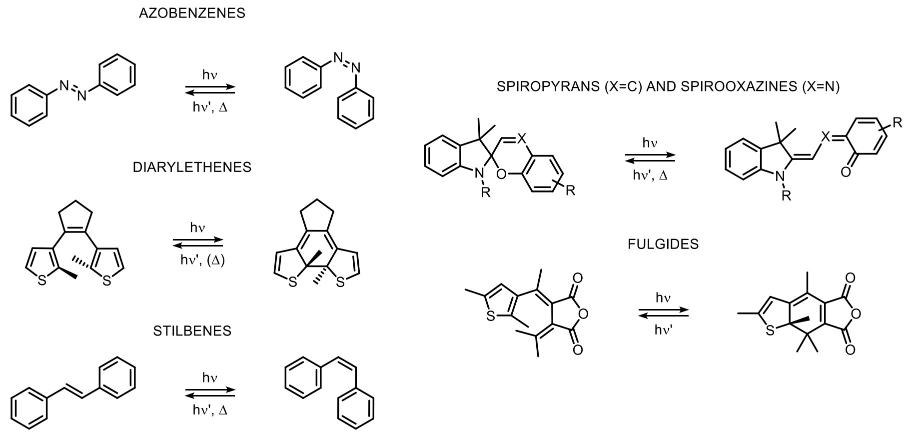

Figure 3: Structures and photoreactions of the main classes of photochromic molecules.

Movements and functions

The movements performed by artificial molecular machines are generally rather simple, but they can be exploited to eventually achieve more complex functions. In figure 4, few examples of molecular motions are depicted. The simplest and most common motions are undoubtfully the shuttling and the rotation. For instance, if the axle of a rotaxane is endowed with two stations for the ring, with different stabilities, an input can be sent to destabilize one station and push the ring to the other.[60,61] In a similar manner, the two rings of a catenane can rotate one with respect to the other.[62,63] An interesting application of the shuttling motion is in [*c*2]rotaxanes, *i.e.*, interlocked hermaphroditic molecules where the axle and the thread are covalently linked. If two stations are present on each thread, an extension or contraction of the whole device is associated to the shuttling motion. Therefore, these supermolecules are usually referred to as molecular muscles.[64] The shuttling can be even coupled with chemical reactions to transport cargos[65] or to synthesize molecules in a controlled order.[66] By combining and amplifying these simple movements, and by implementing them in more complex architectures it is possible to obtain useful functions, even with macroscopic outcomes.[43,67,68]

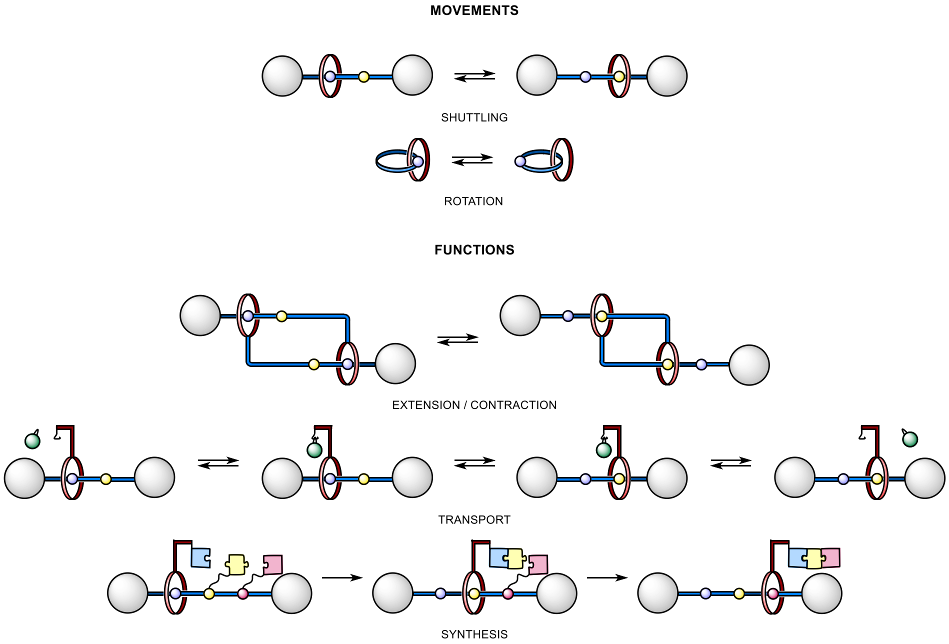

Figure 4: Schematic representation of some examples of functions operated by molecular machines based on rotaxanes and catenanes.

A keypoint in the description of a molecular machine is the difference between *switches* and *motors*. According to the commonly accepted definitions at the present moment,[1,34,69] a molecular switch can be defined as a bi- or multistable molecular device, whose states can be interconverted one into another upon an external stimulus. A pictorial representation of the operation of a switch is reported in figure 5, left: the input required to switch the lever from state *0* to state *1*, is the opposite of the one required to reset the system to the initial state. Since, in this manner, the work done in the forward process is erased by the backward one, a molecular switch is not able to perform useful work. Contrarywise, in a molecular motor, the path along the states is unidirectional, thus useful work can be obtained from the sum of the works obtained in each process. In figure 5, right, an example of motor is depicted. In this case, due to the peculiar ratchet-like shape of the wheel, the movement is allowed only in the counter-clockwise direction, and, in order to restore the initial position of the lever, a complete rotation must be performed.

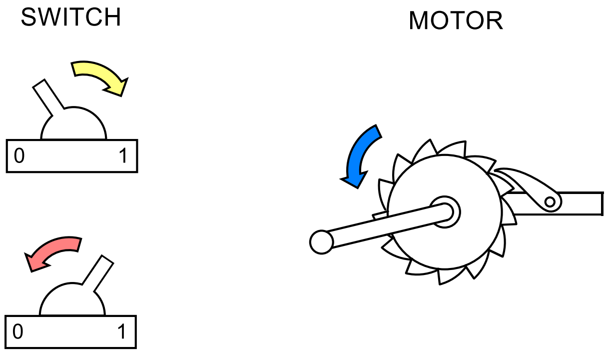

Figure 5: Left: schematic representation of the operation of a switch; right: schematic representation of a motor.

In order to achieve unidirectionality, the molecular building blocks must be properly designed both in terms of structure and properties. First and foremost, at least one of the components should be non-symmetric, in order to define a direction of the motion. In a properly designed self-assembled system where one component is non-symmetric, the formation of the supermolecule occurs in a preferential direction, *i.e.*, on the reaction coordinate displaying the lower energetic barrier. In absence of a kinetic control, the direction of the disassembly process is the opposite of the assembly one. As a result, the forward and backward processes follow the same path on the reaction coordinate, in two opposite directions. However, to obtain a molecular motor, the direction of disassembly must be the same of the assembly one. In this regard, besides the bias given by the modulation of the recognition site, which controls the formation of the complex, a second energetic bias should be applied on the kinetic barriers to disfavour the movement on the direction of entry and prompt instead the movement in the opposite direction. This mechanism, that aims at exploiting and rectifying the random Brownian motions to achieve controlled and precise movements, is called *Brownian ratchet*.[4,5,10,12,36,49,70] The term *ratchet* stands for the similarity between this quantum mechanism and the macroscopic gears and wheels that guarantee the unidirectionality in macroscopic motors and engines. Obviously, at the nanoscopic level, the behaviour of a particle or a system is dictated by the asymmetry of the maxima and minima on the potential energy surfaces. Therefore, the ratchet mechanism must deal with the modification of the energy of the system under an external stimulus. Physically speaking, many different kinds of ratchet mechanism can be conceived.[4,5,12] The mathematical treatment and the physical principles related to these concepts are not straightforward[5] and will not be discussed here. However, a simplified description of two ratchet mechanisms, namely the *energy ratchet* and the *information ratchet*, will be presented (figure 6).

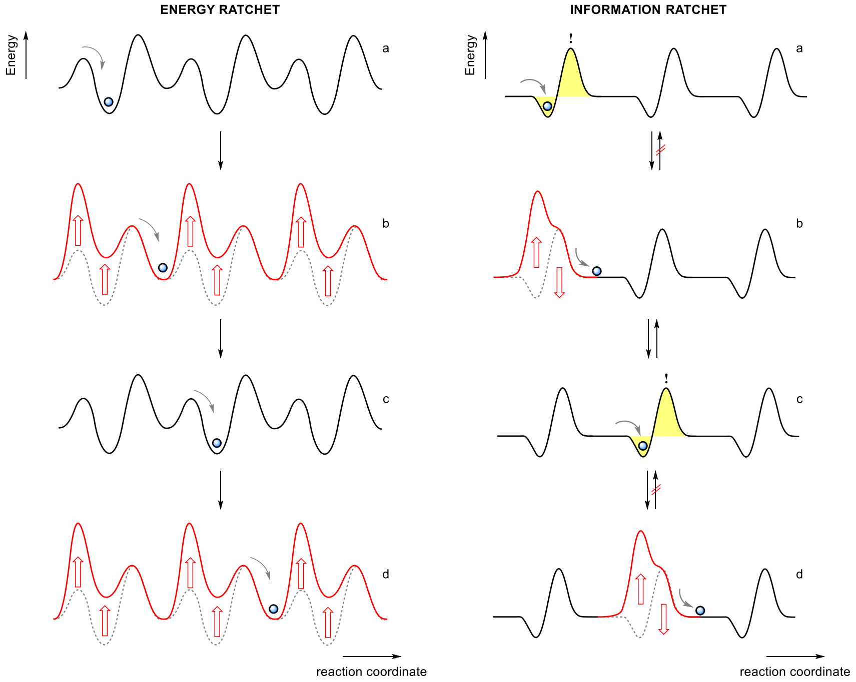

Figure 6: Operation of energy (left) and information (right) ratchet mechanisms.

The energy ratchet[5,12,70] mechanism consists in the perturbation of both the minima and the maxima of the potential energy surface as a result of an external input. As schematized in figure 6, left, the particle reaches spontaneously the potential well, corresponding to the energetic global minimum (*a*). When an input is sent to the system (*b*), the lowest energy maxima and minima increase (red arrows), thus inverting the relative height and depth of barriers and wells and the potential well becomes a local minimum. As a consequence, the particle tends to move to the present global minimum, *i.e.*, towards the right (*c*). When the initial state is restored the progression continues in the same direction (*d*), as long as the potential energy surface is modulated. The overall result is the motion of the particle along a single direction. In this scheme, the modulation of the energy profile occurs independently on the position of the particle along the profile. The energy ratchet mechanism is the simplest example of Brownian ratchet, and represents the basis of the operation of several kinds of molecular machines and motors based on mechanically interlocked molecules[50,61,71] and supermolecules[49,72–75].

The information ratchet mechanism[5,12,36,70] is of higher complexity with respect to the energy ratchet. In this regime, the energy of the system is perturbed only in presence of information, which, in most of the cases, is represented by the position of the particle. Figure 6, right, depicts how the input acts on the potential energy surface in this case: only when the particle is in the potential well and close to the barrier (*a*), the energy increases (*b*, red arrows), triggering the movement of the particle itself towards the right. After the reset (*c*), the particle cannot overcome the energetic barrier on the left, and it reaches the second potential well, where a second input can prompt the energy increase and continue the motion towards the right (*d*). The similarity with Maxwell's demon paradox[36,70,76] is straightforward. In 1867, James Clerk Maxwell conceived a thought experiment to demonstrate a possible route to violate the second principle of thermodynamics, that, in the last two centuries has been proven to be an absurd conjecture. In this experiment, two boxes, both full of gas particles at the same temperature, are separated by a door. A demon can pinpoint a particle that is accidentally moving faster and open the door to let it go inside the other box. In this way, the average agitation of the particles in the first box decreases, whereas it increases in the second box, conferring to the latter a higher temperature. Nonetheless, it must be underlined that, notwithstanding the demon operates an information ratchet, where the information is the velocity of the particle, the two boxes are initially at the thermal equilibrium and no energy is supplied from the exterior. In molecular machines, the energy involved is sent within the input, thus the system is not at the chemical equilibrium yet, and the second law of thermodynamic is not violated. The first example of molecular device operating according to an information ratchet has been reported by Leigh in 2007 (figure 7).[36]

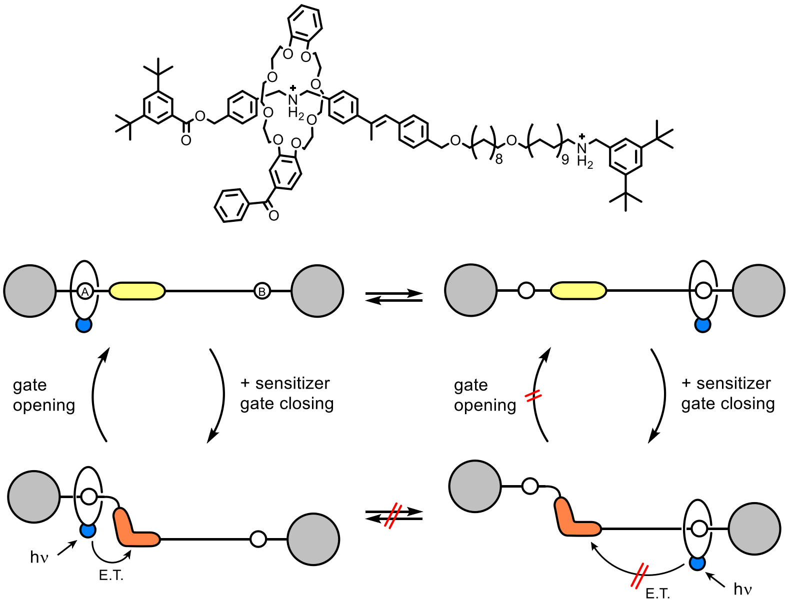

Figure 7: Molecular structure and simplified schematization of the molecular information ratchet by Leigh.[36]

In this paper, Leigh reported a non-symmetric rotaxane with two ammonium stations (*A* and *B* in figure 7) separated by a photoswitchable gate (methylstilbene), where the ring is a crown-ether endowed with a benzophenone moiety. As long as the gate is open, the ring can shuttle between the two stations according to a statistical distribution dictated by the difference in energy of the two sites. Upon irradiation in presence of an external sensitizer (benzil), photoisomerization occurs, and the gate is closed. In these conditions, upon light irradiation, if the ring is on the ammonium site *A*, *i.e.*, close to the gate, energy transfer takes place from the benzophenone to the methylstilbene, and the gate is opened again. Conversely, if the ring is on the station *B*, *i.e.*, far from the gate, no energy transfer can occur and the gate remains closed. Consequently, the population of rotaxanes bearing the ring on the station *B* is increased, regardless of the initial statistical distribution. In the following two decades, only few additional examples of machines[50,60] and motors[49] operated by an information ratchet mechanism have been reported. As already anticipated above, it is noteworthy that a ratchet mechanism always guarantees unidirectionality but is not sufficient to obtain a molecular motor. Indeed, if only one process is ratcheted, the reset can cancel the work already done.[36] Instead, in a molecular motor all the components of the working pathway are ratcheted and proceeding in the same direction.

As an example of molecular rotary motor, it is worth mentioning the very first prototype, reported by Feringa and co-workers in 1999.[44] It consists of an overcrowded alkene with chiral helicity, which can unidirectionally rotate the two substituents of the double bond, conventionally called *rotor* and *stator*, upon light irradiation, acting as a single molecule light-driven rotary motor (figure 8). Under UV light, the (*P,P*)-*E* isomer photoisomerizes to the (*M,M*)-*Z*, then the helicity is switched at room temperature (20°C). The resulting (*P,P*)-*Z* isomer is unstable under UV light and photoconverts to the (*M,M*)-*E* form, which, at higher temperatures, can give a second helix inversion to restore the initial state. Many generations of molecular motors based on this design were realized in the last years[45–48] and applied in smart materials.[43,67,77]

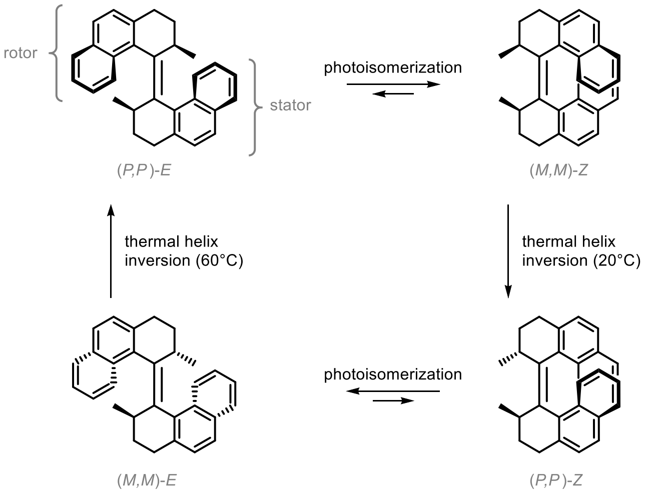

Figure 8: Structure and mechanism of the unidirectional motion of the motor reported by Feringa in 1999.[44]

Due to the very large number of molecular machines and motors present in the literature so far and their high complexity, no further examples will be discussed herewith. Interested readers can refer to the several reviews cited within this chapter. Nonetheless, the progress in the field of molecular machines is still in continuous growth. In point of fact, there is large room for improvement of many aspects at the basis of the molecular machines. For instance, only a few examples of operating molecular motors have been reported until now, which represent impressive proofs-of-concept, but which are rather far from a practical application in everyday life. In this regard, both the performance and the design must be improved and rationalized to allow their implementation in smart materials. Furthermore, the elementary functions executed so far by artificial molecular machines have not allowed yet to accomplish profitable work. In summary, to develop intriguing molecular machines and motors which can really improve the human life and the environment, performing useful functions with clean and sustainable sources of energy, a great research contribution is still required from the scientific community.

The research presented in this work deals with the study of the improvement of electro- and photoactivated molecular machines already reported in literature and with the characterization of new prototypes, with a particular emphasis on the study of how the behaviour of the photo- and electro-responsive moieties changes between the molecular components and the assemblies.

References

1. V. Balzani, A. Credi, and M. Venturi, *Molecular Devices and Machines– A Journey into the Nano World,* Wiley-VCH, Weinheim, **2004**.
2. D. S. Goodsell, *Bionanotechnology: Lessons from Nature*, Wiley-Liss, Inc., **2004**.
3. R. A. L. Jones, *Soft Machines - Nanotechnology and Life,* Oxford University Press, Oxford, U.K., **2008**.
4. P. Hoffmann, *Life's Ratchet. How Molecular Machines Extract Order*

from Chaos, Basic Books, **2012**.

5. R. D. Astumian, *Phys. Chem. Chem. Phys.*, **2007**, *9*, 37, 5067–5083.
6. C. von Ballmoos, G. M. Cook, and P. Dimroth, *Annu. Rev. Biophys.*, **2008**, *37*, 1, 43–64.
7. N. Hirokawa, Y. Noda, Y. Tanaka, and S. Niwa, *Nat. Rev. Mol. Cell Biol.*, **2009**, *10*, 10, 682–696.
8. B. J. Foth, M. C. Goedecke, and D. Soldati, *Proc. Natl. Acad. Sci.*, **2006**, *103*, 10, 3681–3686.
9. J. F. Stoddart, *Acc. Chem. Res.*, **2001**, *34*, 6, 410–411.
10. S. Erbas-Cakmak, D. A. Leigh, C. T. McTernan, and A. L. Nussbaumer, *Chem. Rev.*, **2015**, *115*, 18, 10081–10206.
11. V. Balzani, A. Credi, F. M. Raymo, and J. F. Stoddart, *Angew. Chem. Int. Ed.*, **2000**, *39*, 19, 3348–3391.
12. E. R. Kay, D. A. Leigh, and F. Zerbetto, *Angew. Chem. Int. Ed.*, **2007**, *46*, 1-2, 72–191.
13. W. R. Browne and B. L. Feringa, *Nat. Nanotechnol.*, **2006**, *1*, 1, 25–35.
14. M. Baroncini, S. Silvi, and A. Credi, *Chem. Rev.*, **2019**, DOI: 10.1021/acs.chemrev.9b00291.
15. M. Baroncini, M. Canton, L. Casimiro, *et al.*, *Eur. J. Inorg. Chem.*, **2018**, *42*, 4589–4603.
16. R. B. Feynman, R. P. Leighton and M. Sands, *The Feynman Lectures on Physics; Vol. 1, Chapter 46,* Addison-Wesley: Reading, MA, **1963**.
17. J. M. Lehn, *Nobel Lecture,* **1987**.
18. J. M. Lehn, *Supramolecular Chemistry - Concepts and Perspectives,* Wiley-VCH, Weinheim, Germany, **1995**.
19. J. W. Steed and J. L. Atwood, *Supramolecular Chemistry*, 2nd ed. Wiley, **2009**.
20. T. Kusukawa and M. Fujita, *J. Am. Chem. Soc.*, **2002**, *124*, 45, 13576–13582.

21. M. V Rekharsky, T. Mori, C. Yang, *et al.*, *Proc. Natl. Acad. Sci.*, **2007**, *104*, 52, 20737–20742.

22. D. J. Cram and J. M. Cram, *Science*, **1974**, *183*, 4127, 803–809.

23. H.-J. Schneider and A. K. Yatsimirsky, *Chem. Soc. Rev.*, **2008**, *37*, 2, 263–277.

24. A. Dalla Cort, P. De Bernardin, G. Forte, and F. Yafteh Mihan, *Chem. Soc. Rev.*, **2010**, *39*, 10, 3863–3874.

25. J. R. Moran, S. Karbach, and D. J. Cram, *J. Am. Chem. Soc.*, **1982**, *104*, 21, 5826–5828.

26. L. Mandolini and R. Ungaro, Eds., *Calixarenes in Action*, Imperial College Press, London, **2000**.

27. Z. Asfari, V. Bohmer, J. Harrowfield, and J. Vicens, Eds., *Calixarenes 2001*, Kluwer, Dordrecht, **2001**.

28. G. Crini, *Chem. Rev.*, **2014**, *114*, 21, 10940–10975.

29. S. J. Barrow, S. Kasera, M. J. Rowland, J. del Barrio, and O. A. Scherman, *Chem. Rev.*, **2015**, *115*, 22, 12320–12406.

30. P. R. Ashton, V. Balzani, O. Kocian, L. Prodi, N. Spencer, and J. F. Stoddart, *J. Am. Chem. Soc.*, **1998**, *120*, 43, 11190–11191.

31. J.-C. Chambron and D. K. Mitchell, *J. Chem. Edu.*, **1995**, *72*, 12, 1059-1064.

32. P. R. Ashton, E. J. T. Chrystal, P. T. Glink, *et al.*, *Chem. Eur. J.*, **1996**, *2*, 6, 709–728.

33. J. F. Stoddart, *Chem. Soc. Rev.*, **2009**, *38*, 6, 1802–1820.

34. C. J. Bruns and J. F. Stoddart, *The Nature of the Mechanical Bond*, Wiley, Hoboken, New Jersey, **2017**.

35. see e.g.: V. Balzani, M. Clemente-León, A. Credi, *et al.*, *Proc. Natl. Acad. Sci.*, **2006**, *103*, 5, 1178–83.

36. V. Serreli, C.-F. Lee, E. R. Kay, and D. A. Leigh, *Nature*, **2007**, *445*, 7127, 523–527.

37. see e.g.: T. Muraoka, K. Kinbara, and T. Aida, *Nature*, **2006**, *440*,

7083, 512–515.

38. see e.g.: W.-Y. Sun, T. Kusukawa, and M. Fujita, *J. Am. Chem. Soc.*, **2002**, *124*, 39, 11570–11571.

39. see e.g.: S. Chen, Y. Wang, T. Nie, *et al.*, *J. Am. Chem. Soc.*, **2018**, *140*, 51, 17992–17998.

40. see e.g.: A. Tron, I. Pianet, A. Martinez-Cuezva, *et al.*, *Org. Lett.*, **2017**, *19*, 1, 154–157.

41. see e.g.: K. Zhu, G. Baggi, and S. J. Loeb, *Nat. Chem.*, **2018**, *10*, 6, 625–630.

42. see e.g.: S. Silvi, A. Arduini, A. Pochini, *et al.*, *J. Am. Chem. Soc.*, **2007**, *129*, 44, 13378–13379.

43. Q. Li, G. Fuks, E. Moulin, *et al.*, *Nat. Nanotechnol.*, **2015**, *10*, 161-165.

44. N. Koumura, R. W. J. Zijlstra, R. A. van Delden, N. Harada, and B. L. Feringa, *Nature*, **1999**, *401*, 6749, 152–155.

45. M. M. Pollard, M. Klok, D. Pijper, and B. L. Feringa, *Adv. Funct. Mater.*, **2007**, *17*, 5, 718–729.

46. M. M. Pollard, A. Meetsma, and B. L. Feringa, *Org. Biomol. Chem.*, **2008**, *6*, 3, 507–512.

47. J. C. M. Kistemaker, P. Štacko, J. Visser, and B. L. Feringa, *Nat. Chem.*, **2015**, *7*, 11, 890–896.

48. S. J. Wezenberg and B. L. Feringa, *Nat. Commun.*, **2018**, *9*, 1, 1984.

49. G. Ragazzon, M. Baroncini, S. Silvi, M. Venturi, and A. Credi, *Nat. Nanotechnol.*, **2015**, *10*, 1, 70–75.

50. M. R. Wilson, J. Solà, A. Carlone, S. M. Goldup, N. Lebrasseur, and D. A. Leigh, *Nature*, **2016**, *534*, 235-240.

51. C. Biagini, F. Di Pietri, L. Mandolini, O. Lanzalunga, and S. Di Stefano, *Chem. – A Eur. J.*, **2018**, *24*, 40, 10122–10127.

52. S. Kozuch and S. Shaik, *Acc. Chem. Res.*, **2011**, *44*, 2, 101–110.

53. G. Ragazzon and L. J. Prins, *Nat. Nanotechnol.*, **2018**, *13*, 10, 882–889.

54. A. E. Kaifer, *Supramolecular Electrochemistry*. John Wiley & Sons, Ltd, **2000**.

55. P. Ceroni, A. Credi, and M. Venturi, *Chem. Soc. Rev.*, **2014**, *43*, 12, 4068–4083.

56. H. Rau, *Photochromism. Molecules and Systems,* Elsevier, Amsterdam, **1990**.

57. Y. Yokoyama and K. Nakatani, Eds., *Photon-Working Switches*. Springer, **2017**.

58. M. Irie, *Chem. Rev.*, **2000**, *100*, 5, 1685–1716.

59. H. M. D. Bandara and S. C. Burdette, *Chem. Soc. Rev.*, **2012**, *41*, 5, 1809–1825.

60. M. Alvarez-Pérez, S. M. Goldup, D. A. Leigh, and A. M. Z. Slawin, *J. Am. Chem. Soc.*, **2008**, *130*, 6, 1836–1838.

61. T. Avellini, H. Li, A. Coskun, *et al.*, *Angew. Chem. Int. Ed.*, **2012**, *51*, 7, 1611–1615.

62. D. A. Leigh, J. K. Y. Wong, F. Dehez, and F. Zerbetto, *Nature*, **2003**, *424*, 6945, 174–179.

63. A. Livoreil, C. O. Dietrich-Buchecker, and J.-P. Sauvage, *J. Am. Chem. Soc.*, **1994**, *116*, 20, 9399–9400.

64. C. J. Bruns and J. F. Stoddart, *Acc. Chem. Res.*, **2014**, *47*, 7, 2186–2199.

65. C. Schäfer, G. Ragazzon, B. Colasson, M. La Rosa, S. Silvi, and A. Credi, *Chem. Open*, **2015**, *5*, 2, 120–124.

66. G. De Bo, M. A. Y. Gall, M. O. Kitching, *et al.*, *J. Am. Chem. Soc.*, **2017**, *139*, 31, 10875–10879.

67. J.-F. Morin, Y. Shirai, and J. M. Tour, *Org. Lett.*, **2006**, *8*, 8, 1713–1716.

68. B. K. Juluri, A. S. Kumar, Y. Liu, *et al.*, *ACS Nano*, **2009**, *3*, 2, 291–300.

69. B. L. Feringa and W. R. Browne, Eds., *Molecular Switches*, 2nd ed. Wiley-VCH, Weinheim, Germany, **2011**.

70. M. N. Chatterjee, E. R. Kay, and D. A. Leigh, *J. Am. Chem. Soc.*, **2006**, *128*, 12, 4058–4073.

71. S. Erbas-Cakmak, S. D. P. Fielden, U. Karaca, *et al.*, *Science*, **2017**, *358*, 6361, 340 LP – 343.

72. M. Baroncini, S. Silvi, M. Venturi, and A. Credi, *Angew. Chem. Int. Ed.*, **2012**, *51*, 17, 4223–4226.

73. C. Cheng, P. R. McGonigal, S. T. Schneebeli, *et al.*, *Nat. Nanotechnol.*, **2015**, *10*, 547–553.

74. C. Cheng, P. R. McGonigal, W.-G. Liu, *et al.*, *J. Am. Chem. Soc.*, **2014**, *136*, 42, 14702–14705.

75. C. Pezzato, M. T. Nguyen, D. J. Kim, O. Anamimoghadam, L. Mosca, and J. F. Stoddart, *Angew. Chem. Int. Ed.*, **2018**, *57*, 30, 9325–9329.

76. *Nature*, **1879**, *20*, 501, 126.

77. R. Eelkema, M. M. Pollard, J. Vicario, *et al.*, *Nature*, **2006**, *440*, 7081, 163.

Part A

Molecular and supramolecular structures involving photochromic units

Chapter 1.

Light-driven supramolecular pumps

1.1 Introduction and aim

In living organisms, biological functions critically depend on the concentration and the flux of ions and chemicals through different cells and tissues, which are usually compartmentalized environments. Carrier proteins represent a beautiful example of molecular motors endowed in cellular membranes, through which nature is able to move unidirectionally one species from the exterior to the interior and *vice versa*, most of the times against the concentration gradient.[1] Inspired by nature and aiming at mimic its stunning creations, supramolecular chemists have been able to realize, in the last decade, similar but much simpler prototypes of artificial molecular machines that are able to pump chemicals in one direction. A supramolecular pump can be defined as a molecular-level motor able to move one component with respect to the others in a unidirectional fashion, as a response to an external stimulus.[2–4] So far, only a few examples of operating molecular pumps based on pseudorotaxanes have been reported by the groups of Credi[5–7] and Stoddart.[8–11] In a molecular pump, the presence of a recognition site, which biases the brownian motion and triggers the assembly of the components, is not sufficient to guarantee unidirectionality, which must be instead achieved through a ratchet mechanism.[12–15] As a simple scenario, let us consider a pseudorotaxane composed of a non-symmetric axle and a macrocycle. The assembly of the supermolecule occurs in a preferential direction, which, in absence of any stimulus, represents also the preferred direction for the disassembly. Thus, a modification of the energy surface must be operated, in order to disfavour the motion through the site of entrance and prompt the disassembly from the other extremity, *i.e.,* pump the two components along a unidirectional path.

In one of his artificial molecular pumps, Stoddart realized a ratchet mechanism through alternated redox stimuli (figure 1.1). The pseudorotaxane is formed by a cyclobis(paraquat-*p*-phenylene) ring (**BB**$^{4+}$, blue-box) and a non-symmetric modular axle composed, in this sequence, by a pyridinium (**P**$^{+}$), a bipyridinium station (**BP**$^{2+}$), an isopropylphenyl hampering group (**IPP**), a triazole (**T**), a ring reservoir (**R**) and a stopper (**S**).

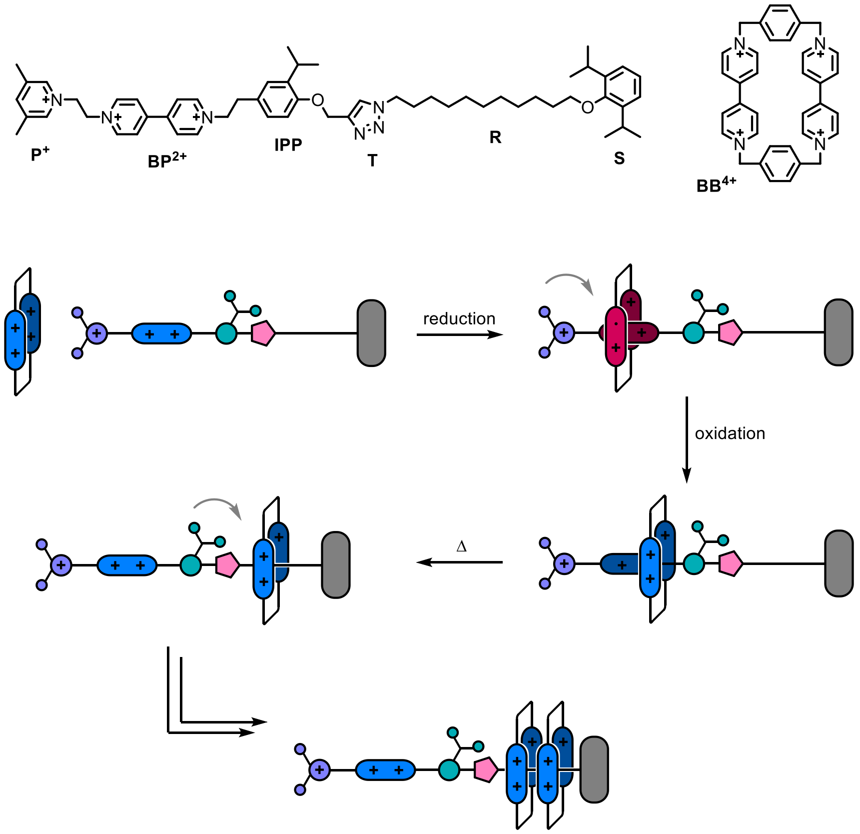

Figure 1.1: Top: molecular structures of the axle (left) and the ring (right) of the molecular pump by Stoddart;[10] *bottom: scheme of the operation mechanism of the molecular pump.*

After reduction of the system operated by an external chemical reductant, the bireduced ring **BB**$^{2(+\cdot)}$ threads on the axle and gives a stable interaction with the monoreduced station **BP**$^{+\cdot}$. When the system is re-oxidized, a strong charge repulsion occurs between the ring and the station. However, the dethreading is less favourable over the charged **P**$^{+}$ extremity, thus the ring moves over the **IPP** moiety. The repulsion between the positive charge is at the basis of the ratchet mechanism, as it both forces the dethreading of the ring and disfavours the motion through the entrance site. Once the ring reaches the reservoir station, the operation can be repeated: when the system is reduced a second time, a free ring and the one already threaded compete to move on the **BP**$^{+\cdot}$ station, but the motion of the latter is impeached by the **IPP** moiety. In this manner, Stoddart and coworkers were able to store up to two rings in the device.[10]

The molecular pump by Credi et al.[6] is based on a crown ether – ammonium pseudorotaxane (figure 1.2). The crown ether is a dinaphtho-[24]crown-8 (**DN24C8**), whereas the axle is a non-symmetric ammonium salt composed of an azobenzene as photoswitchable unit at one extremity and a methylcyclopentyl as a *pseudostopper* at the other. The steric hindrance of the *Z* isomer of the azobenzene is much larger than the one of the *E* isomer, thus the *Z*-azobenzene behaves as a stopper for the ring.[5,16,17] On the other hand, the kinetic barrier related to the methylcyclopentyl is intermediate between those of the two forms of the azobenzene, hence the name. The operating cycle of this molecular pump is schematized in figure 1.2. In suitable non-protic solvents (CH_2Cl_2, CH_3CN), the system assembles on account of the stabilization of the hydrogen bonding between the ammonium and the oxygen atoms of the crown ether. Since the kinetic barrier associated to the transit on the pseudostopper is larger than that of the *E*-azobenzene, the ring threads exclusively from the azobenzene extremity. In this device, the ratcheting is obtained photochemically: when the azobenzene is converted from the *E* to the *Z* isomer, the kinetic barrier related to the transit on this side increases, *i.e.,* this gate is locked. At the same time, the potential well associated to the pseudorotaxane is decreased in depth, since the *Z*-pseudorotaxane is less stable than the *E* one. As a result, to fulfil the *Z* association constant, some of the complexed systems have to disassemble, but the transit can occur exclusively over the pseudostopper side. Once this unidirectional motion of the ring along the axle is obtained, the system can be reset thermally or photochemically and restarted.

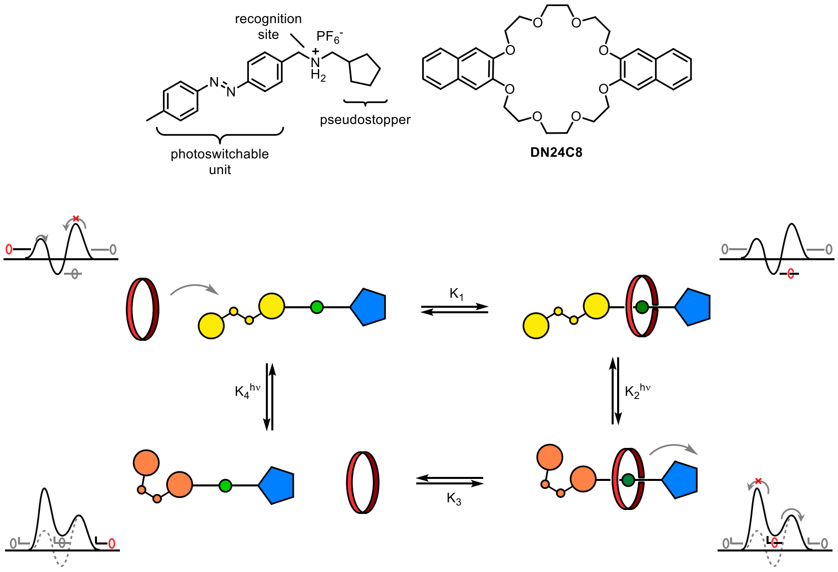

Figure 1.2: Top: molecular structures of the axle (left) and the ring (right) of the molecular pump by Credi;[6] *bottom: scheme of the operation cycle and of the reaction curves of the molecular pump.*

This molecular device possesses two interesting features, namely it works autonomously and in a dissipative manner. The autonomy[4] is achieved thanks to the optical properties of the azobenzene. Indeed, since the absorption spectra of the two configurational isomers are overlapped on the whole absorption region, photons of the same wavelength can induce either the *E*-*Z* and the *Z*-*E* photoisomerization. Thus, a single stimulus can operate the whole cycle. The dissipative behaviour is a consequence of the photo-driven operation cycle, which breaks the detailed balance.[14,18] In a square network of reactions (figure 1.3, left), the microscopic reversibility principle states that, at the chemical equilibrium, the product of the thermodynamic constants of the vertical processes must be equal to that of the horizontal ones, and that the rates of all the reactions must be equal and equal to zero. However, in the present case, the vertical processes are photoreactions, thus energy is provided through light (figure 1.3 right). As a consequence, the detailed balance is broken and the system reaches a stationary state, *i.e.*, the dissipative state, where all the reactions have an equal non-zero rate and the concentrations are constant, but at values not compatible with those of the equilibrium. In other words, the whole system is kept out of the chemical equilibrium by light, and tends to reach the equilibrium by dissipating the energy provided from the exterior.[19]

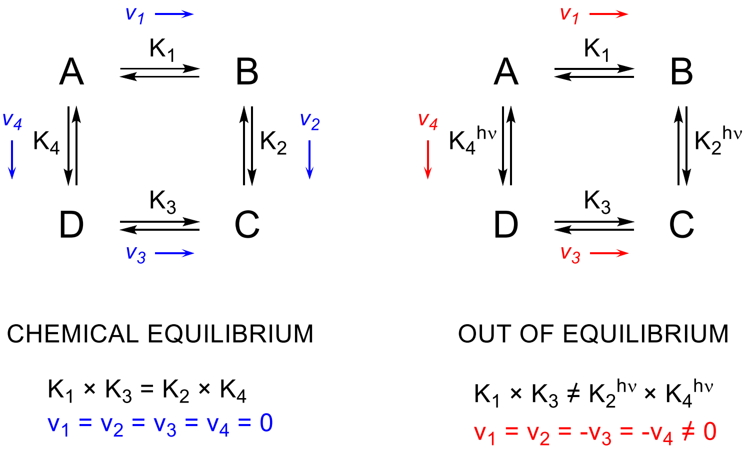

Figure 1.3: Scheme of a square network of reactions at the equilibrium (left) and out of equilibrium (right).

Interestingly, this prototype of molecular pump can operate either via energy ratchet and information ratchet mechanisms (table 1.1). Indeed, when visible light (436 nm) is employed the two vertical processes have equal efficiency, but $K_1 > K_3$, therefore the system cycles clockwise according to a pure energy ratchet. *Vice versa*, if UV light is employed, the ratcheting is given also by the presence of a piece of information, namely whether the ring and the axle are associated or not. Indeed, at 365 nm the *E*-pseudorotaxane absorbs more than the sum of the free ring and *E*-axle, whereas, upon irradiation at 287 nm, the ring absorbs and transfers energy only to the E-azobenzene and only in the *E*-pseudorotaxane. In both cases, $K_2^{h\nu}$ is larger than $K_4^{h\nu}$, meaning that a contribution from an information ratchet mechanism is present.

λ_{irr} / nm	$K_2^{h\nu}$	$K_4^{h\nu}$	$K_2^{h\nu}$ / $K_4^{h\nu}$	*Ratchet mechanism*
287	0.45	0.32	1.4	Energy + information
365	99	24	4.1	Energy + information
436	0.19	0.19	1	Energy

Table 1.1: Ratchet mechanisms at the different irradiation wavelengths.

The work here presented has been devoted to the design and study of new prototypes of molecular pumps based on this design.[6] In particular, new molecular axles were studied, in order to improve the efficiency of the device and allow further derivatizations to insert the pumping module in more complex architectures. The design of new axles followed three different strategies: (i) azobenzene functionalization, (ii) pseudostopper replacement, (iii) linker displacement (figure 1.4). All the axles were studied in association with either dinaphtho-[24]crown-8 (**DN24C8**) or dibenzo-[24]crown-8 (**DB24C8**) rings and either in CH_2Cl_2 or CH_3CN. In addition, kinetic simulations were carried out in order to elucidate the dissipative behaviour and the best operation conditions of the pump.

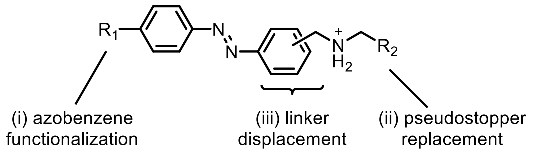

Figure 1.4: Strategies for the design of new molecular axles.

1.2 Azobenzene functionalization: cyanoazobenzene derivatives

The first strategy adopted for the design of new axles for the molecular pump is a derivatization of the *para* position of the azobenzene moiety. This functionalization aims at both improving the performance of the molecular motor and allowing further functionalizations. From previous preliminary studies,[20] it was found out that the most suitable compound is derivative **1.1**H⁺, bearing a cyano group on the *para* position of the azobenzene (figure 1.5).

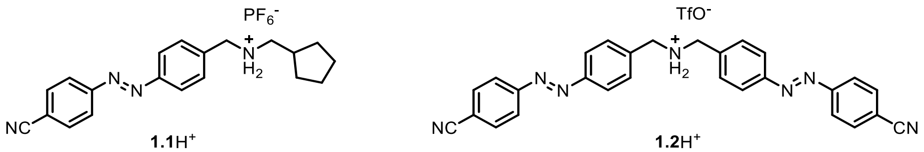

1.1H⁺

1.2H⁺

*Figure 1.5: Molecular structures of axles **1.1**H⁺ and **1.2**H⁺.*

The absorption spectra of compound **1.1** and of its related symmetric compound **1.2**, in their protonated and neutral form, are reported in figure 1.6. The main π-π* band in the UV region of **1.1**H$^+$ possesses a larger absorption coefficient (ε = 31000 M^{-1} cm^{-1} at 323 nm) and a more structured band with respect to similar azobenzene-type compounds.[21,22] Moreover, the ratio between the π-π* and n-π* bands (ε = 650 M^{-1} cm^{-1} at 451 nm) is higher with respect to related compounds. Regarding the symmetric compound **1.2**H$^+$, due to its poor solubility in CH_2Cl_2 in its PF_6^- salt form, the neutral compound **1.2** was protonated in situ with triflic acid (TfOH). The spectral features are similar to the ones of **1.1**H$^+$ (ε = 44000 M^{-1} cm^{-1} at 326 nm, ε = 990 M^{-1} cm^{-1} at 453 nm) and in line with the presence of two chromophoric units. In both cases, the neutral forms **1.1** and **1.2** are redshifted with respect to the corresponding protonated ones.

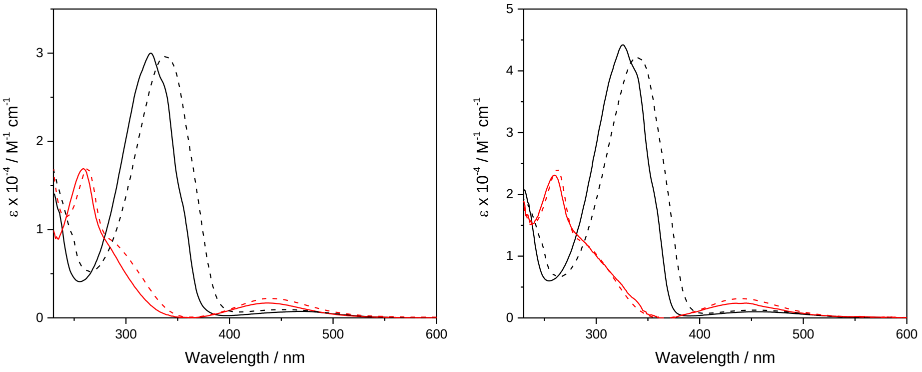

Figure 1.6: Absorption spectra in CH_2Cl_2 of the E (black line) and Z (red line) isomers of the protonated (solid line) and neutral (dashed line) forms of ***1.1*** *(left) and* ***1.2*** *(right).*

A supramolecular investigation, conducted in association with crown ether **DN24C8**, evidenced a fast threading (k_{in} = 1000 M^{-1} s^{-1}) of *E*-**1.1**H$^+$ with the crown, and a slow threading (k_{in} = 1.2 M^{-1} s^{-1}) of *Z*-**1.1**H$^+$. The value of the kinetic constant for the threading of *Z* isomer is comparable to those of model compounds,[6] thus signifying that the ring transits on the cyclopentil unit. On the other hand, the larger rate constant of threading in the *E* isomer would indicate that the crown transits on the azobenzene unit. In addition, the rate of this process is larger than in the cases already reported,[6] on account of the electronic effects exerted by the cyano group. Moreover, the stability constant drops of one order of magnitude, namely from 3.7×10^6 M^{-1} for the *E* complex to 3.6×10^5 M^{-1} for the *Z* complex. Therefore, **1.1**H^+ appears to be an interesting candidate for the supramolecular pump. Nevertheless, the photochemistry of this compound resulted to be erratic and not reproducible.[20] In particular, under UV irradiation, the compound undergoes a *E*-*Z* photoisomerization and, at some point, the trend is reversed. The complete recovery of the initial spectrum in the dark and the presence of isosbestic points rule out the hypothesis of photodegradation. However, a photostationary state (PSS) is never reached and the maximum photoconversion is not univocal. To further understand this erratic behaviour, the photochemistry of such compound was studied in its deprotonated form and in the complex with **DN24C8** ([**1.1**H⊃**DN24C8**]$^+$), and compared to that of the corresponding symmetric axle **1.2**H^+.[7] Irradiations at 365 nm produced, in both the deprotonated form (**1.1**) and the complex [**1.1**H⊃**DN24C8**]$^+$, absorption variations coherent with a *E*-*Z* photoisomerization, up to a stable PSS rich in *Z* isomer. In the case of **1.2**H^+, a clean *E*/*Z* photoisomerization is displayed for the neutral and the protonated compounds and for the pseudorotaxane. Interestingly, the photoisomerization quantum yields of **1.2**H^+ resulted to be the half of those of **1.1**H^+. These values are in line with the presence of two photoswitchable units that behave independently. Indeed, along the irradiation, only one family of isosbestic points can be identified, meaning that the two photochromic units behave independently and that a statistical mixture of the three possible isomers, namely *EE*, *EZ*, and *ZZ,* is obtained. Thus, the photoisomerization quantum yield is referred to the *E* and *Z* isomers of azobenzene units in the ensemble, and, consequently, if the efficiency is the same for **1.2**H^+ and **1.1**H^+, the quantum yield of **1.2**H^+ is half of that of **1.1**H^+.

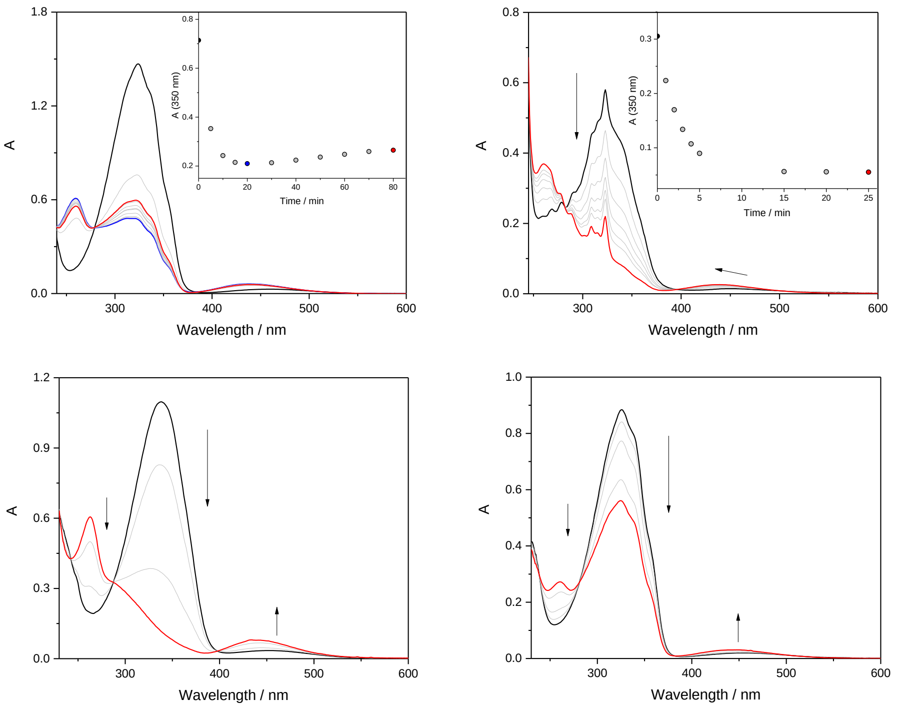

*Figure 1.7: Photoisomerization at 365 nm of **1.1**H$^+$ (top left, 5.0 × 10^{-5} M), [**1.1**H⊃**DB24C8**]$^+$ (top right, 1.7 × 10^{-5} M), **1.1** (bottom left, 3.7 × 10^{-5} M) and **1.2**H$^+$ (bottom right, 2.0 × 10^{-5} M).*

Species	Φ_{EZ} *(365 nm)*	Φ_{ZE} *(365 nm)*	k_{Δ} / s^{-1}
1.1	0.07	0.18	9.4 × 10^{-6}
1.1H$^+$	0.02	N.A.	3.6 × 10^{-6}
*[**1.1**H⊃**DB24C8**]$^+$*	0.06	0.24	9.7 × 10^{-6}
1.2H$^+$	0.01	0.18	3.8 × 10^{-5}

*Table 1.2: Photoisomerization quantum yields at 365 nm and thermal isomerization constants for species **1.1**, **1.1**H$^+$, [**1.1**H⊃**DB24C8**]$^+$ and **1.2**H$^+$.*

On the basis of these considerations, it can be hypothesized that the unusual photoisomerization of compound **1.1**H$^+$ is due to an interference from the acidic proton of the ammonium site, which is absent in the neutral form and involved in the complexation with the crown in the pseudorotaxane. To some extent, the photochemical behaviour is improved in the supramolecular system, as it can happen for related systems (see Chapter 2).[23] Regarding the symmetric compound, the absence of any photochemical issue could be ascribed to the presence of two azobenzene units, each bearing an electron-withdrawing cyano group. Therefore, the symmetry of the molecule could arguably lead to a reduced acidity of the ammonium proton. Despite the favourable kinetic and thermodynamic parameters, the erratic behaviour of the free axle under continuous irradiation prevents the correct operation of the supramolecular pump based on this axle.

1.3 Pseudostopper replacement: dimethylbenzyl stoppers and pseudostoppers

Despite the favourable kinetic features, the methylcyclopentyl group does not allow simple further functionalizations, due to its poor reactivity and the coexistence of more than one conformer. In order to replace the methylcyclopentyl group, a derivatized benzyl ring was chosen as pseudostopper. In order to pinpoint the suitable derivatization, the threading kinetics in CH_2Cl_2 of **DB24C8** with a series of symmetric bis-(dimethyl)benzyl ammonium PF_6^- salts (**1.3**-**1.8**H$^+$) was surveyed. Dibenzylammonium (**DBA**), dimethylcyclopentylammonium (**1.9**H$^+$) and bis-(*p'*-methyl)azobenzeneammonium (**1.10**H$^+$) were taken as reference compounds (figure 1.8). From preliminary NMR studies, it was found out that mixtures of **DB24C8** and compounds **1.6**H$^+$, **1.7**H$^+$ and **1.8**H$^+$ do not yield pseudorotaxanes, neither after several days. In other words, when the aromatic ring is methylated in *3,5-*, *2,6-* or *2,3-* position with respect to the benzylic position, it behaves as a stopper. Compound **1.5**H$^+$ is only poorly soluble in CH_2Cl_2 and does not allow any NMR or UV-vis spectroscopic investigation. Nevertheless, it threads in **DB24C8** in CH_3CN with low kinetic constants (below 10^{-4} M^{-1} s^{-1}).

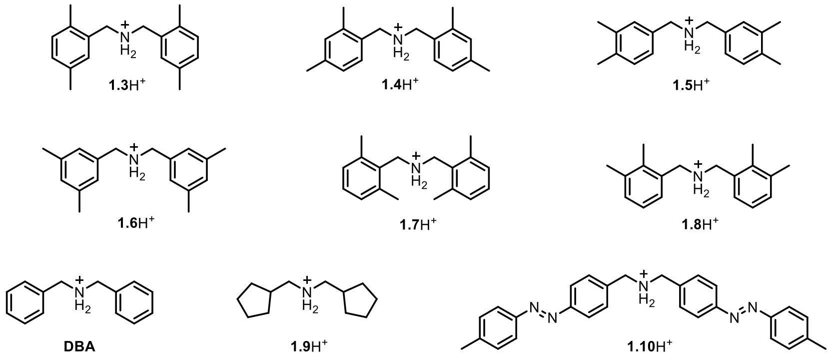

*Figure 1.8: Molecular structures of the symmetric salts **1.3**-**1.8**H$^+$ and of the model compounds dibenzylammonium (**DBA**), **1.9**H$^+$ and **1.10**H$^+$. All the compounds are in form of hexafluorophosphate salts.*

The stability constant of complex **DBA⊃DB24C8** was determined via UV-vis titration, and resulted to be 2.2×10^{6} M^{-1} (figure 1.9).[24] The fast absorbance variations upon mixing of the axle and the crown ether suggest a fast threading kinetics. Therefore, the threading process was studied by means of a stopped-flow apparatus. On low timescales, *i.e.*, few tens of milliseconds, no evidences of processes are visible, meaning that the threading process is completed in less than 2 ms.

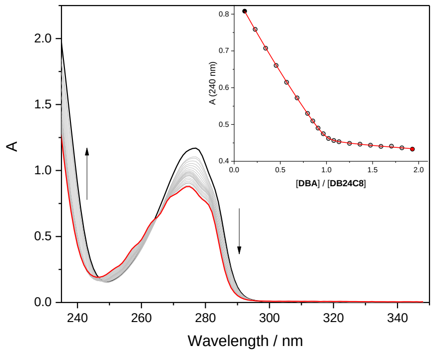

*Figure 1.9: Left: Absorption changes upon titration of a 2.3×10^{-4} M solution of **DB24C8** with concentrated **DBA**; inset: absorbance variations at 240 nm.*

The pseudorotaxane formed by compound **1.9**H^+ and crown ether **DB24C8** resulted to be less stable with respect to those formed with axles containing aromatic units, as already evidenced in related studies.[5,6] The stability constant, determined upon UV-vis titration (figure 1.10), is 6.0×10^4 M^{-1}. The threading occurs with a rate constant of 2.5 M^{-1} s^{-1}, and the dethreading with a rate of 4.2×10^{-5} s^{-1}, as reported in figure 1.10.

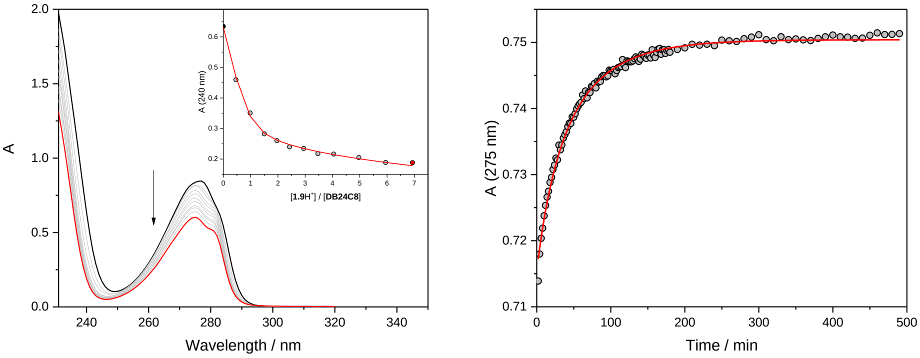

*Figure 1.10: Left: Absorption changes upon titration of a 1.6×10^{-4} M solution of **DB24C8** with concentrated **1.9**H^+; inset: absorbance variations at 240 nm; right: kinetic profile at 275 nm and fitting (red line) upon mixing of **1.9**H^+ and **DB24C8** (final concentrations: [**DB24C8**] = 1.4×10^{-4} M, [**1.9**H^+] = 1.6×10^{-4} M).*

The model compound **1.10**H^+ yields pseudorotaxanes with stabilities comparable to those of **DBA**, *i.e.*, with $K_c = 2.0 \times 10^6$ M^{-1} (figure 1.11), as already reported in previous studies.[5,6,16] The threading kinetics follows a non-trivial profile, which cannot be satisfactorily fitted neither with a mixed order (second order threading, first order dethreading) nor with a second or first order model. It could be supposed that parallel intra- and intermolecular processes are likely to be involved. Nevertheless, an estimation of threading rate can be obtained by fitting the kinetic trace with a pure second order kinetic model, assuming that, on account of the large thermodynamic constant, the dethreading is slow enough to be negligible. The determined value is 69 M^{-1} s^{-1}.

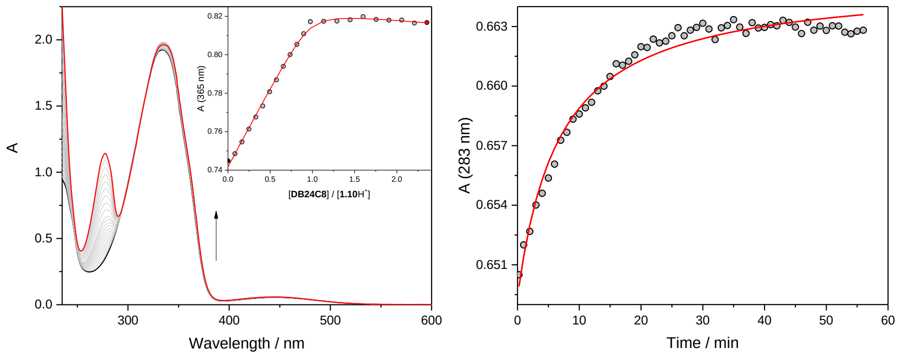

Figure 1.11: Left: Absorption changes upon titration of a solution 4.2 × 10^{-5} M of ***1.10****H^+ with concentrated* ***DB24C8****; inset: absorbance variations at 365 nm; right: kinetic profile and fitting (red line) at 283 nm upon mixing of two equimolar solutions of* ***1.10****H^+ and* ***DB24C8*** *(final concentrations 3.8 × 10^{-5} M).*

A Mauser plot[25] obtained from the absorbance values of the kinetic measurements shows a non-linear trend, most likely due to the presence of more simultaneous processes (figure 1.12, left). A second plot, obtained by dividing the former absorbances for a third one, approaches the linearity (figure 1.12, right). These evidences suggest that the threading process consists in two parallel equilibria or that when the crown ether and the axle are mixed, a second equilibrium besides the threading takes places. Nevertheless, no signal can be ascribed to a third species, and in the UV-vis conditions it is not possible to discriminate between the various processes. On the other hand, the overall kinetics is too fast to be observed via NMR spectroscopy, thus understanding the real mechanism of this process is a challenging task and beyond the scope of this work.

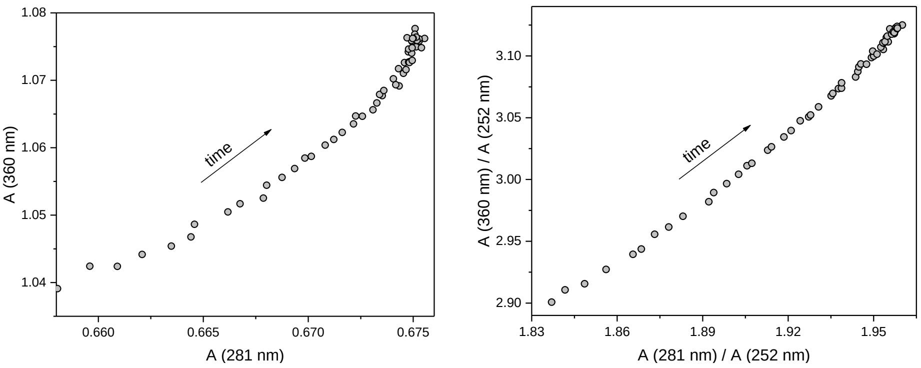

*Figure 1.12: Mauser plots of the absorbances at 360 nm vs 281 nm (left) and of the ratio of the two absorbances and that at 252 nm (right), for the threading kinetics of **1.10**H$^+$ and **DB24C8**.*

The pseudorotaxanes [**1.3**H⊃**DB24C8**]$^+$ and [**1.4**H⊃**DB24C8**]$^+$ possess lower stabilities with respect to the related pseudorotaxane with **DBA** (figure 1.13, left). The thermodynamic constants resulted to be 8.0×10^5 M^{-1} for [**1.3**H⊃**DB24C8**]$^+$ and 1.7×10^5 M^{-1} for [**1.4**H⊃**DB24C8**]$^+$. On the other hand, in both cases the threading kinetics resulted to be much slower than those of **DBA** and **1.10**H$^+$, but larger than that of **1.9**H$^+$. In particular, axle **1.3**H$^+$ threads into the crown ether with a rate of 38 M^{-1} s^{-1}, whereas axle **1.4**H$^+$ with a rate of 12 M^{-1} s^{-1} (figure 1.13, right). As a matter of fact, both the axles **1.3**H$^+$ and **1.4**H$^+$ fulfil the kinetic requirements of a good pseudostopper, as both of them thread in the crown ether with intermediate rates between those of the *E*- and the *Z*-azobenzene.

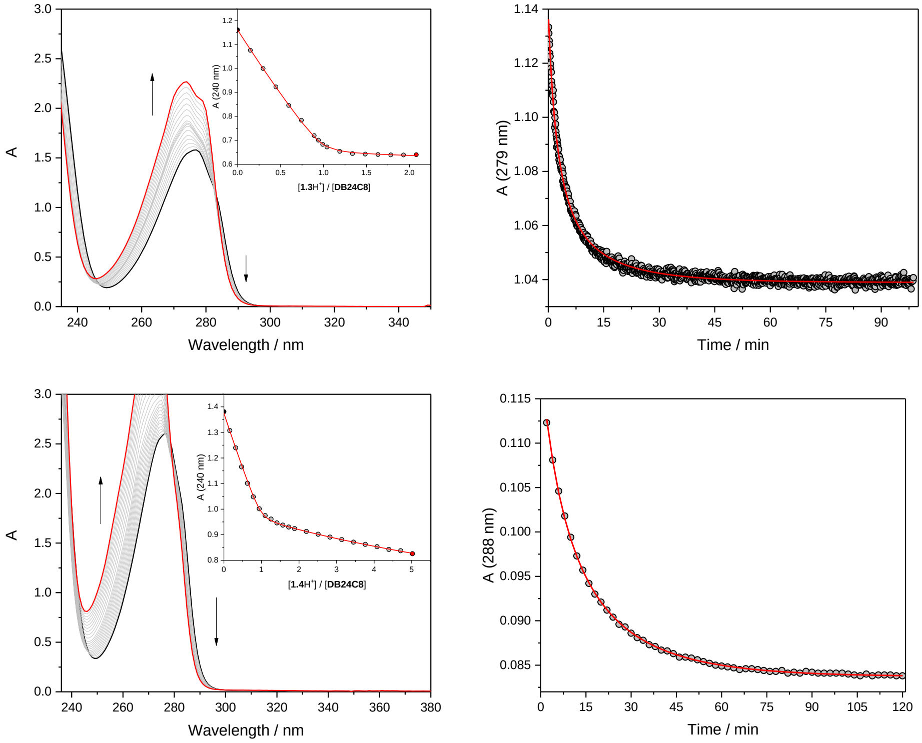

Figure 1.13: Left: Absorption changes upon titration of a 3.0 × 10^{-4} M solution of ***DB24C8*** *with concentrated* ***1.3***H^+ *(top) and of a 4.9 × 10^{-4} M solution of* ***DB24C8*** *with concentrated* ***1.4***H^+ *(bottom); right: kinetic profiles and fitting (red line) upon mixing* ***DB24C8*** *and* ***1.3***H^+ *(top, final concentrations: [**DB24C8**] = [**1.3**H^+] = 1.9× 10^{-4} M) and* ***DB24C8*** *and* ***1.4***H^+ *(bottom, final concentrations: [**DB24C8**] = [**1.4**H^+] = 1.0 × 10^{-4} M).*

In summary, the survey reported above highlighted that the kinetics of threading of a symmetric salt bearing two benzylic units can be drastically influenced or even impeached by the regiochemistry of its functionalizations. The most promising axle resulted to be compound **1.3**H^+.

1.4 Pseudostopper replacement: non-symmetric axles and statistical considerations

On the basis of the results of the survey reported in paragraph 1.3, non-symmetric axle **1.11**H^+, bearing a *2,5*-dimethylbenzyl group as a pseudostopper, was synthesized (figure 1.14). This compound shows the typical features of azobenzene derivatives,[6] but the presence of the benzylic group is responsible of two shoulders at 272 and 280 nm (figure 1.14). The photochemistry of this molecular axle is fully comparable with the already reported compounds bearing a *p*-methylazobenzene photoactive unit,[6] with a *E*-*Z* quantum yield of 0.14.

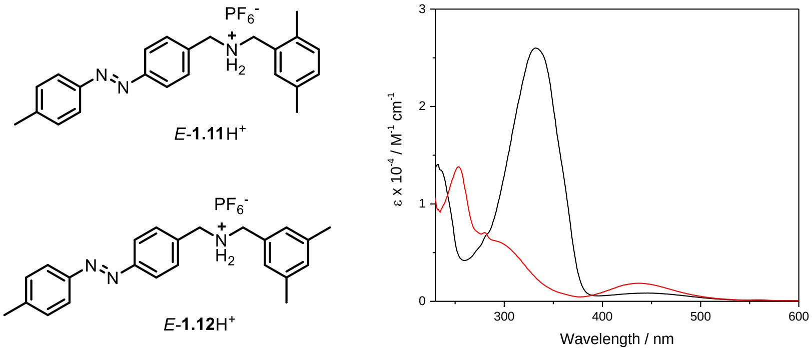

*Figure 1.14: Molecular structures of **1.11**H^+ and **1.12**H^+ (left) and absorption spectra of the E (black) and Z (red) isomers of compound **1.11**H^+ (right).*

The supramolecular characterization was conducted in association with crown ether **DN24C8**. Unexpectedly, by titration of the axle with the crown ether the absorption variation related the association process are not large enough to overcome those obtained by the addition of the crown ether. Therefore, it was not possible to obtain the binding constants of the *E* and *Z* pseudorotaxanes with this experimental set up. Nevertheless, an estimation of these constants was provided by fitting of the kinetic traces obtained upon mixing **DN24C8** with either *E*- and *Z*-**1.11**H^+ (figure 1.15). The experimental data were fitting with a mixed order kinetic model, without any constrain on the values of the threading (k_{in}) and dethreading (k_{out}) kinetic constants. The ratio between k_{in} and k_{out} gave an approximated value of the equilibrium constant K_c. Compound *E*-**1.11**H^+ threads into the crown with a rate constant larger than 90 M^{-1} s^{-1}, and dethreads with a rate constant lower than 4.5×10^{-5} s^{-1} (figure 1.15, left, table 1.3). With these parameters, the stability constant of pseudorotaxane *E*-[**1.11**H⊃**DN24C8**]$^+$ results to be at least 2×10^6 M^{-1}. On the other hand, the kinetics of *Z*-**1.11**H$^+$ gives good-quality fitting with values of k_{in} = 35 – 45 M^{-1} s^{-1} and k_{out} = 1.2×10^{-4} – 4.4×10^{-5} s^{-1}, that correspond to thermodynamic constant between 3×10^5 and 1×10^6 M^{-1} (figure 1.16, right, table 1.3).

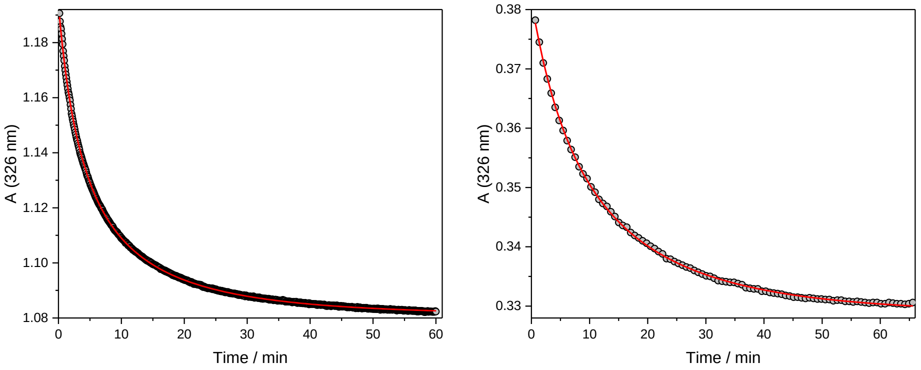

*Figure 1.15: Absorbance changes at 326 nm over time and fitting (red line) upon mixing equimolar 3.9×10^{-5} solutions of **DN24C8** and E-**1.11**H$^+$ (left) or Z-**1.11**H$^+$ (right).*

In order to pinpoint which extremity of the axle the ring transits on, the values reported above were compared with the threading kinetics of **DN24C8** with the corresponding symmetric axles **1.3**H$^+$ and *E*-**1.10**H$^+$, and with a similar compound (**1.12**H$^+$), bearing a *3,5*-dimethylbenzylgroup that behaves as a stopper (figure 1.16). It must be remarked that the kinetic constants are obtained by fitting the experimental data with a mixed order kinetic model, with the constrain that the ratio between the threading and dethreading kinetic constants must be equal to the association constant K_c. According to this method, the values of k_{in} and k_{out} increase as K_c increases. In other words, the transit on the same moiety is faster if the supramolecular complex is more stable. Therefore, the comparison of the threading kinetics between different axles must take into account the discrepancy in the stability constants. The threading kinetics of *E*-**1.12**H$^+$, which can occur only from the azobenzene site, possesses a rate constant comprised between 16 and 30 M^{-1} s^{-1}. In the case of *EE*-**1.10**H$^+$, bearing two identical azobenzene moieties, *i.e.*, two accessible gates, the rate constant is doubled with respect of *E*-**1.12**H$^+$ (69 M^{-1} s^{-1}). When compound **1.11**H$^+$ is in the *Z* form, the ring can thread only through the pseudostopper side, since the *Z*-azobenzene behaves as a stopper.[16] Indeed, the rate constant of this process is slightly larger than the half of the corresponding symmetric axle **1.3**H$^+$. On the other hand, the threading of *E*-**1.11**H$^+$ is unexpectedly fast, despite the azobenzene moiety is identical to previously reported compounds.[6] The rate constant for this process exceeds 90 M^{-1} s^{-1}, indicating that the two gates, *i.e.*, the azobenzene and the benzyl group, have a similar probability to be accessed. Therefore, the ring can transit on both the extremities and selectivity is lost (figure 1.16, table 1.3). As a result, in a molecular machine based on this axle, only the dethreading process is unidirectional, meaning that the complexes which thread from the azobenzene side behave as motors, whereas those threading and dethreading from the pseudostopper are instead autonomous supramolecular switches. In any instance, a dissipative state under continuous irradiation can be reached (see chapter 1.5).

Compound	*K_c / M^{-1}*	*k_{in} / M^{-1} s^{-1}*	*k_{out} / s^{-1}*	*accessible gates*	*gate(s) of access*
EE-**1.10**H$^+$	$> 10^7$	69	$< 7 \times 10^{-6}$	2	azobenzene
1.3H$^+$	4×10^5	53	1.3×10^{-4}	2	pseudostopper
E-**1.11**H$^+$	$> 2 \times 10^6$	> 90	$< 4.5\times 10^{-5}$	2	both
Z-**1.11**H$^+$	$3 – 10 \times 10^5$	35 – 45	$12 – 4.4 \times 10^{-5}$	1	pseudostopper
E-**1.12**H$^+$	$7 – 50 \times 10^5$	16 – 30	$23 – 5.7 \times 10^{-5}$	1	azobenzene

Table 1.3: Stability constants (K_c) and kinetic constants of threading (k_{in}) and dethreading (k_{out}) with crown ***DN24C8*** *and gates of threading for compounds* ***1.10****H$^+$,* ***1.3****H$^+$,* ***1.11****H$^+$ and* ***1.12****H$^+$.*

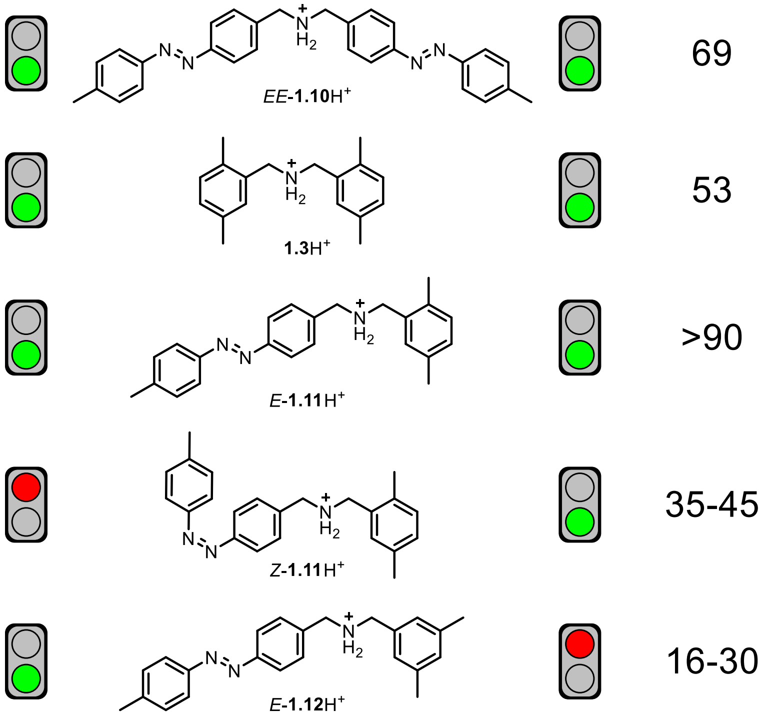

*Figure 1.16: Schematic representation of the gates of threading of compounds **1.10**H^+, **1.3**H^+, **1.11**H^+ and **1.12**H^+.*

The kinetic features of compound **1.11**H^+ suggest that, indeed, the threading occurs according to a statistical factor. From the viewpoint of the ring, as schematized in figure 1.16, each extremity of the axle represents a gate, regardless of the fact that they are linked and the outcome is the same. In this scenario, the kinetic rate quantifies the probability of the ring to thread in that extremity. In a non-symmetric axle with two kinetically different groups, a gate has a larger probability to be accessed then the other, and this leads to selectivity. Conversely, for a symmetric compound, the ring has two accessible gates with the same probability, thus it has a possibility to disappear twice than with a single gate, and the kinetic rate is doubled. When the axle is non-symmetric but the two gates have comparable kinetics, the overall kinetics approaches to the sum of those of the two gates.

The process of threading of a non-symmetric salt *B–C* into a macrocycle *A* can be schematized as follows:

$A + B\text{–}C \rightleftarrows P$ k_1 threading through gate *B*

$A + C\text{–}B \rightleftarrows P$ k_2 threading through gate *C*

The associated kinetic equations are:

$$\frac{d[P]}{dt} = -\frac{d[A]}{dt} = -\frac{d[BC]}{dt} = k_1[A][BC] + k_2[A][BC] = (k_1 + k_2)[A][BC]$$

It can be seen that the overall kinetic constant is the sum of the two components.

In order to find out how large the discrepancy between the two constants should be to have a selective threading, a simulation was conducted with software Berkeley Madonna[26] on a simple bimolecular reaction

$$A + B \overset{k_1+k_2}{\rightarrow} P$$

where $[A]=[B]=10^{-4}$ M, and with different ratios of k_1 and k_2. The resulting half-lives are reported in table 1.4 and figure 1.17.

k_1 / M^{-1} s^{-1}	k_2 / M^{-1} s^{-1}	k_2 / k_1	$t_{1/2}$ / s
100.00	0	0	100
100.00	0.01	1E-4	99.99
100.00	0.10	0.001	99.9
100.00	1.00	0.01	99
100.00	10.00	0.1	90.9
100.00	30.00	0.3	76.92
100.00	50.00	0.5	66.66
100.00	70.00	0.7	58.82
100.00	80.00	0.8	55.55
100.00	90.00	0.9	52.63
100.00	95.00	0.95	51.28
100.00	99.00	0.99	50.25
100.00	99.90	0.999	50.02
100.00	99.99	0.9999	50.00
100.00	100.00	1	50.00

Table 1.4: Half-life times ($t_{1/2}$) for different ratios between k_2 and k_1.

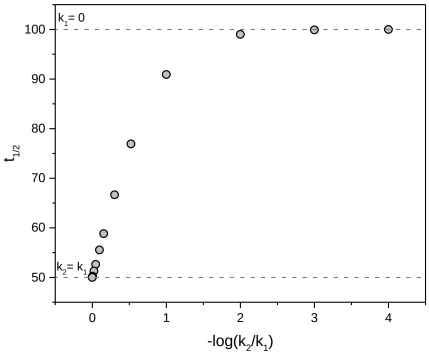

Figure 1.17: Plot of half-life times ($t_{1/2}$) vs antilogarithm of the ratios between k_1 and k_2.

It can be seen that as the value of k_2 approaches that of k_1, the $t_{1/2}$ value is the half of the value, since the kinetic constant is doubled. Moreover, it can be stated that for a 99% selectivity, the value of k_2 must be lower than 0.01 k_1. Thus, in order to have a unidirectional transit, the axle must have a difference between the kinetic constants of at least two orders of magnitude.

1.5 Linker relocation: *ortho*- and *meta*-derivatives and dissipative behaviour

The third strategy adopted for the design of new molecular axles is the change of the substituent position of the ammonium on the azobenzene moiety. Two new axles were synthesized with this approach, namely **1.13**H$^+$ and **1.14**H$^+$ (figure 1.18), which bear the methylenic bridge in *ortho*- and *meta*- position, respectively. The ultimate purpose is to induce a larger sterical destabilization in the *Z* form of the pseudorotaxanes, *i.e.*, increase the difference in the stability constants, and prompt more complexes to dethread upon isomerization.

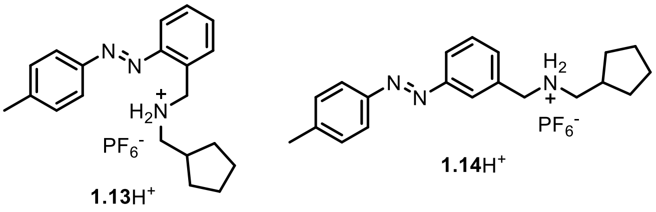

1.13H$^+$

1.14H$^+$

*Figure 1.18: Molecular structures of axles **1.13**$^+$ and **1.14**H$^+$.*

The absorption spectrum in CH_2Cl_2 of compound **1.13**H$^+$ (figure 1.19), bearing the methylenic bridge in *ortho* position with respect to the azo group, shows a rather large overlap between the π-π^* band (λ_{max} = 348 nm, ε = 20000 M^{-1} cm^{-1}) and the n-π^* band. Such overlap is typical of amino-azobenzenes, *i.e.*, azobenzenes with electron-withdrawing groups in *ortho* or *para* position.[21,22] However, in this case, no mesomeric effects are exerted by the substituents directly linked to the aromatic rings. Instead, a weak intramolecular hydrogen bond between the ammonium acidic proton and the azo group can be hypothesized.[27] Indeed, in the absorption spectrum in MeCN, the two bands are more resolved, as this solvent is competitive for the hydrogen bonding (figure 1.19).

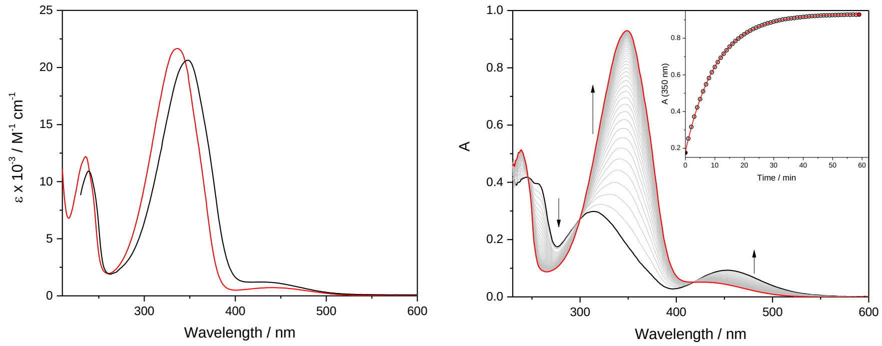

*Figure 1.19: Left: absorption spectra of E-**1.13**H$^+$ in CH_2Cl_2 (black line) and CH_3CN (red line); right: thermal isomerization of a 4.6 × 10^{-5} M solution of **1.13**H$^+$ in CH_2Cl_2, after exhaustive irradiation at 365 nm; inset: absorption changes at 350 nm.*

The *Z* isomer of **1.13**H$^+$ can be obtained upon irradiation in the UV, but it is short-lived and reverts back to the *E* isomer in tens of minutes (k_{Δ} = 1.6 × 10^{-3} s^{-1}, figure 1.19). In the present case, it could be argued that the azo bond is weakly protonated by the ammonium hydrogen, thus its behaviour tends to that of a protonated azobenzene, but its thermal process can still be appreciated in the experimental timescales. The photoisomerization quantum yields could be only estimated, as the recording of the absorption spectrum is largely affected by the fast thermal isomerization. The obtained values are Φ_{EZ} = 0.22 and Φ_{ZE} = 0.39. The thermal isomerization was studied also for the neutral compound (obtained by deprotonation with tributylamine), the pseudorotaxane formed in presence of an excess of **DB24C8** (*vide infra*) and in acetonitrile

(CH_3CN), as reported in table 1.5. As expected, in all the cases, the process is slowed down, most likely due to the absence of the acidic proton (neutral compound), the solvent competition (CH_3CN) or the weakening of the hydrogen bonding (pseudorotaxane), despite all the values of k_Δ remain larger than in case of similar compounds.[22] Interestingly, the thermal process is much slower in the rotaxane than in the neutral compound. This result is in line with similar reported compounds (see paragraph 1.2 and Chapter 2), where the supramolecular bond improves the photochromism.

Species	*Solvent*	*k_Δ / s^{-1}*
1.13H^+	CH_2Cl_2	1.6×10^{-3}
1.13H^+	CH_3CN	8.3×10^{-3}
1.13	CH_2Cl_2	1.6×10^{-4}
[**1.13**H⊃**DB24C8**]$^+$	CH_2Cl_2	2.5×10^{-5}

*Table 1.5: Kinetic constants (k_Δ) of thermal isomerization reactions for compound **1.13**H^+ and related species.*

In the case of pseudorotaxane [**1.13**H⊃**DB24C8**]$^+$, which shows the slowest thermal isomerization, it was possible to obtain the photoisomerization quantum yields without significant errors. The obtained values are $\Phi_{EZ} = 0.20$ and $\Phi_{ZE} = 0.40$, practically unchanged with respect to the isolated axle. A preliminary supramolecular characterization of this compound in association with crown **DB24C8** was conducted in CH_2Cl_2. The stability constant obtained from UV-vis titration was found to be 2.5×10^4 M^{-1}. Interestingly, the threading kinetics of *E*-**1.13**H^+ into **DB24C8** resulted to be slow, with values of the rate constants ($k_{in} = 0.55$ M^{-1} s^{-1}, $k_{out} = 2.2 \times 10^{-5}$ s^{-1}) compatible with those of the methylcyclopentyl group.[6]

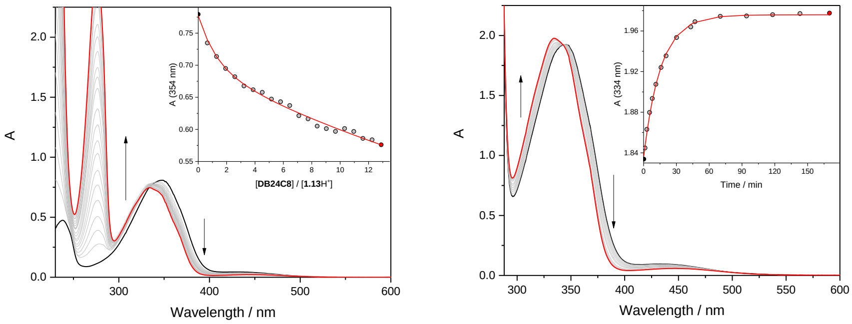

*Figure 1.20: Titration of a 4.0×10^{-5} M solution of **1.13**H^+ with concentrated **DB24C8**; right: absorption variations and kinetic profile (inset) with fitting (red line) of a 3.1×10^{-4} M solution of **1.13**H^+ in excess of **DB24C8** (3.9×10^{-4} M).*

Thus, it was hypothesized that either the molecule in the *E* form is folded enough to prevent the threading from the azobenzene extremity, or the kinetic constant for the threading on the two gates are comparable, thus the ring cannot discriminate between the two. In the first case, the molecular machine cannot be considered a motor, but only a switch, whereas in the second case, as for compound **1.11**H⁺, only a portion of the supermolecules works as a molecular motor and the reminder as an autonomous supramolecular switch.

Compound **1.14**H⁺ was studied in CH_3CN and in association with crown **DB24C8**, as these conditions allow to follow the dissipative operation by NMR experiments,[28] where higher concentrations and lower association constants are required. The absorption spectrum of **1.14**H⁺ is comparable with those of previously reported compounds[5] (figure 1.21). As expected, the derivatization in *meta* position does not significantly affect the optical properties of the azobenzene.[29–31]

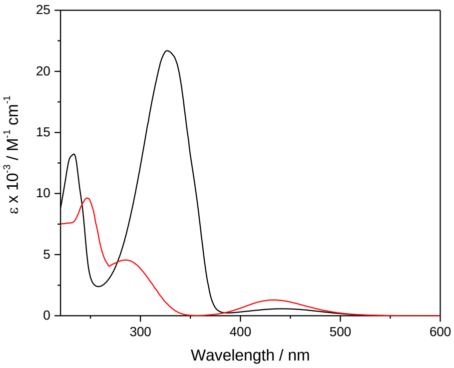

*Figure 1.21: Absorption spectra of E-**1.14**H⁺ (black line) and Z-**1.14**H⁺ (red line) in CH_3CN.*

Upon irradiation at 365 nm, **1.14**H⁺ undergoes an efficient *E*-*Z* isomerization, with spectral features comparable with those of related compounds[5,6] but with larger photoisomerization quantum yields, namely $\Phi_{EZ} = 0.23$ and $\Phi_{ZE} = 0.58$ (figure 1.22). The thermal isomerization occurs with a rate of 1.9×10^{-6} s^{-1}.

Single point NMR titrations evidenced a low association constant ($K_c = 260$ M^{-1}), as it usually happens for these systems in polar protic solvents.[5,32] Therefore, the energetic parameters and the photochemistry of the pseudorotaxane were studied in conditions of large excess (100 equivalents) of crown ether, in order to maximize the percentage of complexed species. The photochemistry of the pseudorotaxane resulted to be fully comparable to that of the isolated axle (figure 1.22), with photoisomerization quantum yields $\Phi_{EZ} = 0.22$ and $\Phi_{ZE} = 0.59$ and $k_{\Delta} = 4.8 \times 10^{-6}$ s^{-1}.

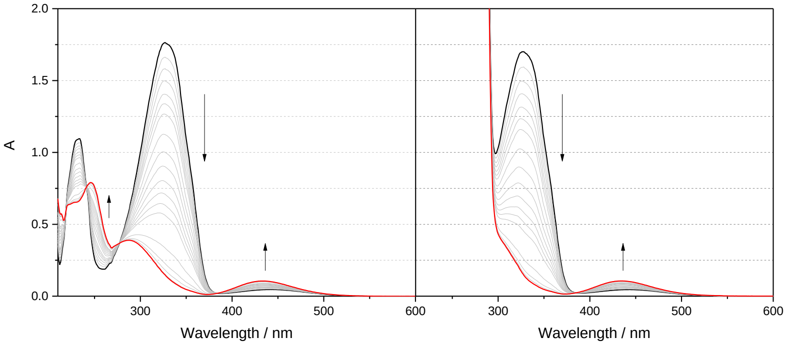

Figure 1.22: Absorption variations of a 7.7 × 10^{-5} M solution of ***1.14**H$^+$* *(left) and of a 7.7 × 10^{-5} M solution of* ***1.14**H$^+$* *in presence of 100 equivalents of* ***DB24C8**, corresponding to 82% of complexation (right) upon irradiation at 365 nm.*

The threading kinetics of *E*-**1.14**H$^+$ and **DB24C8** was investigated by means of a stopped-flow apparatus, since to reach an appreciable amount of pseudorotaxane the concentrations of the two components must be larger than 10^{-4} M and, consequently, the process is completed in few seconds. The values obtained from the kinetic trace (figure 1.23) were fitted according to a mixed order model, and the ratio between the threading and dethreading constants was set equal to the K_c. The obtained values are $k_{in} = 22$ M^{-1} s^{-1} and $k_{out} = 8.5 \times 10^{-2}$ s^{-1}.

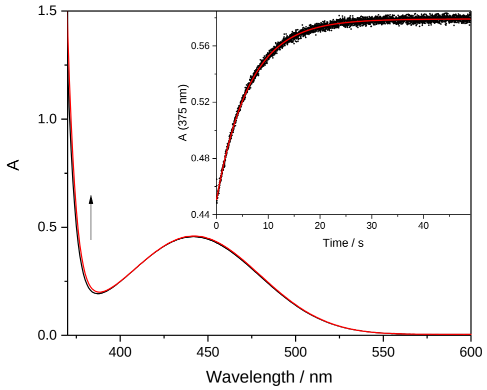

*Figure 1.23: Absorption spectra and absorbance changes at 375 nm (inset) with fitting (red line) upon rapid mixing of **1.14**H^+ and **DB24C8**. Final concentrations: [**1.14**H^+] = 9.5×10^{-4} M, [**DB24C8**] = 3.0×10^{-3} M.*

Due to the low association constant ($K_c = 100$ M^{-1}) and the small spectral variations, the threading kinetics of *Z*-**1.14**H^+ could not be followed via UV-vis techniques. Nevertheless, NMR studies provided a value of 2.3×10^{-2} M^{-1} s^{-1} for the threading and 2.3×10^{-4} s^{-1} for the dethreading.

On the basis of the promising energetical parameters of this supramolecular system, *i.e.*, a good selectivity in the threading and a suitable energetic gap between the association constants of the *E* and *Z* complexes, the photoinduced dissipative state was investigated via time-resolved NMR techniques. The experimental apparatus consists in one optic fibre as light source inserted inside the NMR tube, where the spectra are collected over several hours. Two different sets of data were collected. In the first (figure 1.24, left) a first powerful light input is used to achieve exhaustive *E*-*Z* photoisomerization, then the light intensity is lowered and maintained during the kinetic experiment. In the second (figure 1.24 right), after the first powerful impulse, the light is turned off and the kinetics is followed in the dark. These two complementary experiments incontrovertibly display the discrepancy between the trend of the system moving towards the chemical equilibrium (*i.e.*, when the light is turned off) and of the system operating out of equilibrium in the dissipative regime (*i.e.*, under continuous irradiation). A clear evidence of this dichotomy is provided by the free **DB24C8** concentration. The concentration of the free ring before the irradiation, *i.e.*, when only the *E* species are present, is represented by the continuous lines in the figures. After a fast and powerful light irradiation, that induces *E*-*Z* isomerization, part of the complexed systems must disassemble to fulfil the lower association constant of the *Z* pseudorotaxane, and the concentration of free ring increases (figure 1.24, right). However, when the system is operating under continuous light irradiation, the free ring concentration is dictated by the kinetic features of the dissipative state. As it can be seen in figure 1.24, left, the value of this concentration is lower than both the values at the *Z* and *E* equilibrium. As a matter of fact, this state is not compatible with any *E*/*Z* mixture at chemical equilibrium and can only be accessed by the system when it dissipates the energy (*i.e.*, light) provided from an external source.

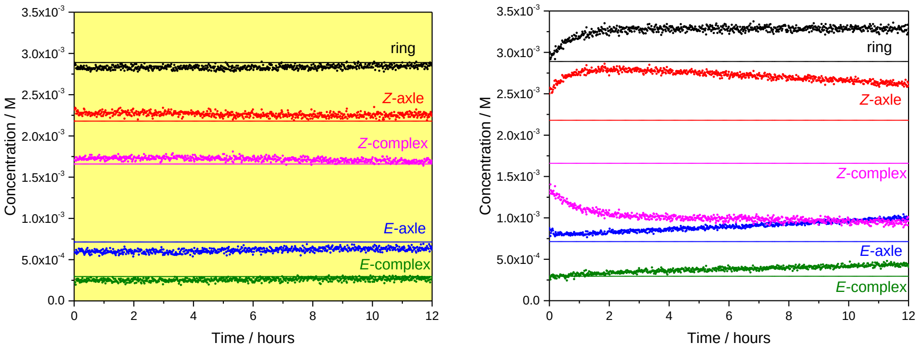

Figure 1.24: Concentration profiles over time, obtained via time-resolved NMR techniques, under continuous irradiation at 365 nm (left) and in the dark after exhaustive irradiation at 365 nm (right) of a solution of ***1.14***H^+ *and* ***DB24C8***. *Initial concentrations: [**DB24C8**] = [**1.14**H^+] = 5.0×10^{-3} M.*

1.6 Dissipative behaviour simulations

In order to simulate the dissipative behaviour of all the prototypes of pumps here reported and eventually corroborate the experimental data for the system based on axle **1.14**H^+ and **DB24C8** which allow a full characterization, simulations have been carried with software Berkeley Madonna.[26] Simulation have also been performed on the model system reported by Credi et al. in 2015.[6] In the general reaction scheme, reported below, *C* represents the free ring, *E* the free *E* axle, *Z* the free *Z* axle, and *CE* and *CZ* the *E* and *Z* complexes, respectively:

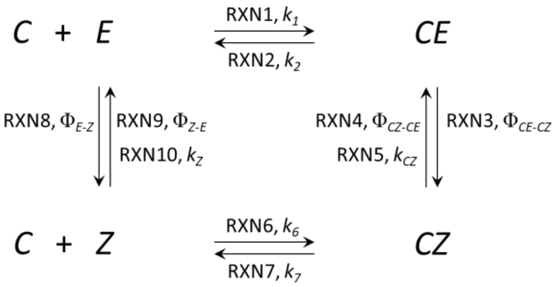

The differential kinetic equations are:

$$RXN1 = k_1[C][E]$$

$$RXN2 = k_1[CE]$$

$$RXN3 = \frac{\Phi_{CE-CZ} \times q \times [CE] \times \varepsilon_{CE} \times b \times (1 - 10^{-A})}{V \times A}$$

$$RXN4 = \frac{\Phi_{CZ-CE} \times q \times [CZ] \times \varepsilon_{CZ} \times b \times (1 - 10^{-A})}{V \times A}$$

$$RXN5 = k_{CZ}[CZ]$$

$$RXN6 = k_6[C][Z]$$

$$RXN7 = k_7[CZ]$$

$$RXN8 = \frac{\Phi_{E-Z} \times q \times [E] \times \varepsilon_{E} \times b \times (1 - 10^{-A})}{V \times A}$$

$$RXN9 = \frac{\Phi_{Z-E} \times q \times [Z] \times \varepsilon_{Z} \times b \times (1 - 10^{-A})}{V \times A}$$

$$RXN10 = k_Z[Z]$$

$$\frac{d[C]}{dt} = -RXN1 + RXN2 - RXN6 + RXN7$$

$$\frac{d[E]}{dt} = -RXN1 + RXN2 - RXN8 + RXN9 + RXN10$$

$$\frac{d[Z]}{dt} = -RXN6 + RXN7 + RXN8 - RXN9 - RXN10$$

$$\frac{d[CE]}{dt} = RXN1 - RXN2 - RXN3 + RXN4 + RXN5$$

$$\frac{d[CZ]}{dt} = RXN3 - RXN4 - RXN5 + RXN6 - RXN7$$

$$J = RXN1 + RXN3 + RXN7 + RXN9 + RXN10 - RXN2 - RXN4 - RXN5 - RXN6 - RXN8$$

where q is the incident photon flux in Einstein/s, A is the absorbance of the mixture, V is the volume, b the optical path, ε the absorption coefficient at the wavelength of irradiation.

The parameter J represents the net flux of matter in the clockwise direction, and is defined as the difference between the rates of the clockwise reactions and the rates of the counter-clockwise reactions. As a matter of fact, this value defines if the pump works out of equilibrium, since it goes to zero when the system reaches the equilibrium, but it is non-zero if a dissipative stationary state is reached.

A first simulation was carried out on all the axles in the standard UV-vis experimental setup, *i.e.*,:

$[C]_0$ = 5.0 x 10^{-5} M

$[E]_0$ = 1.5 x 10^{-4} M

b = 1 cm

V = 3 mL

In these experimental conditions the photon flux is 2.8 x 10^{-8} Einstein/s for 5 minutes, in order to prompt an exhaustive E/Z photoisomerization, then it is reduced to 1.7 x 10^{-9} Einstein/s and eventually switched off in order to show the processes occurring in the dark. The simulations for all the species in solution and an inset with the concentration of free ring [C] are gathered in figure 1.25. The values of fluxes J and the difference between the concentration of free ring at the dissipative state and at the equilibrium are reported in table 1.6.

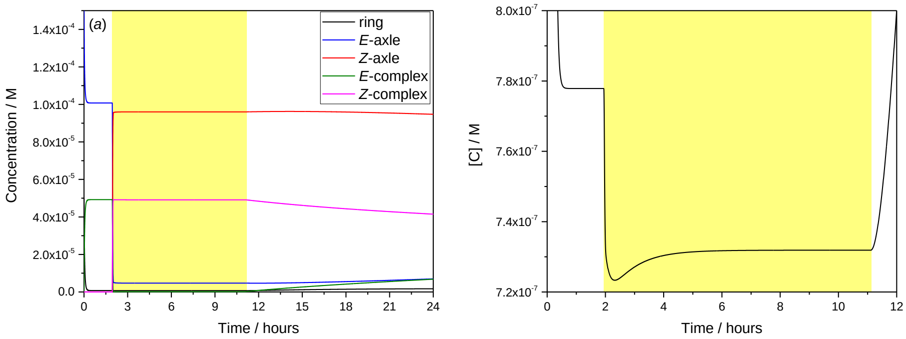

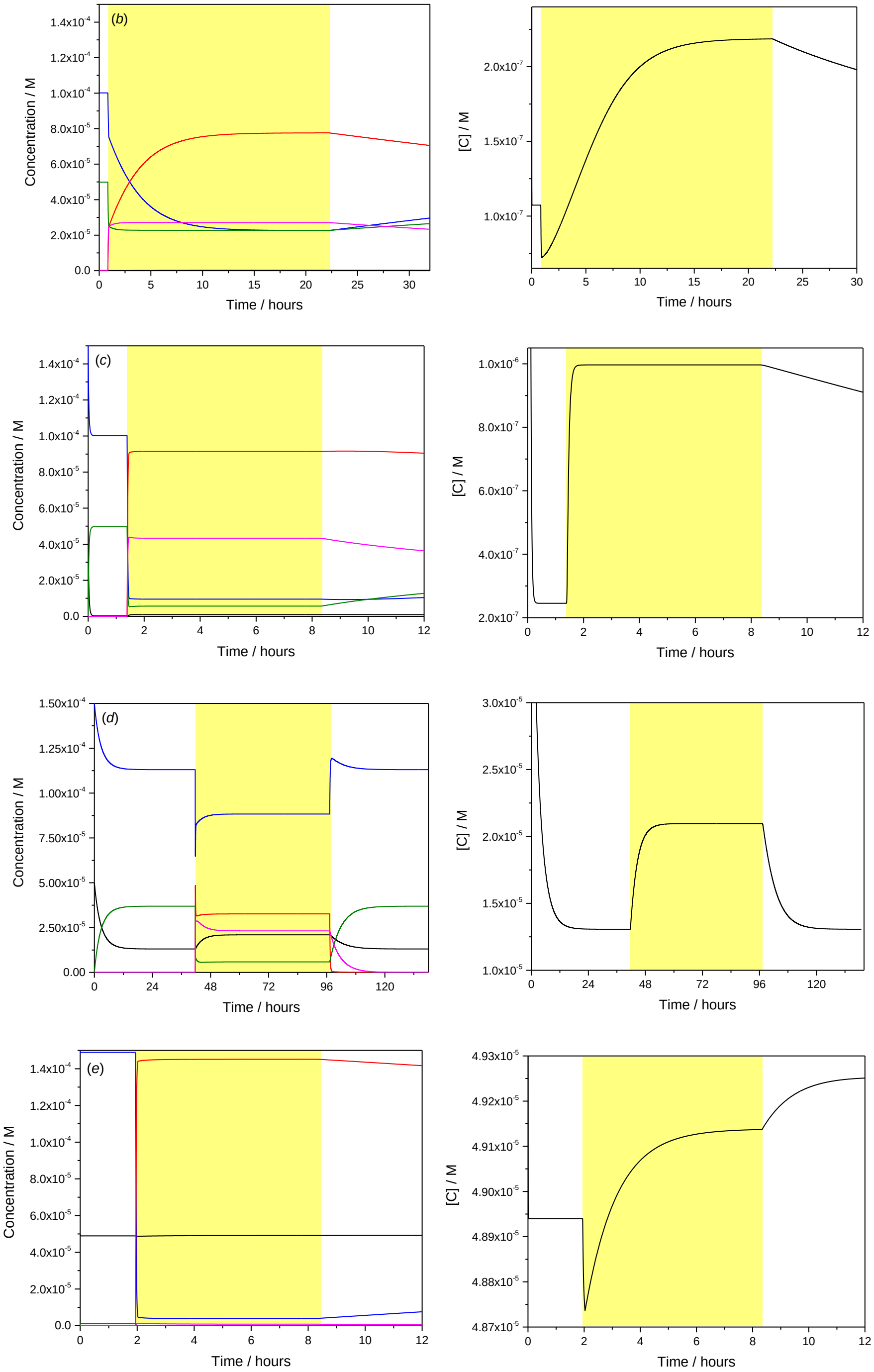

Figure 1.25: Concentrations over time of all the species (left) and of the free ring (right) for the model system[6] *(a),* ***1.1***H^+ *-* ***DN24C8*** *in* CH_2Cl_2 *(b),* ***1.11***H^+ *-* ***DN24C8*** *in* CH_2Cl_2 *(c),* ***1.13***H^+ *-* ***DB24C8*** *in* CH_2Cl_2 *(d) and* ***1.14***H^+ *-* ***DB24C8*** *in* CH_3CN *(e). The yellow part indicates the continuous irradiation.*

Axle	*Ring*	*Solvent*	*J / M s^{-1}*	*$[C]_{eq}$ / M*	*$[C]_{diss}$ / M*	*$\Delta[C]$ / M*	*$\Delta[C]/[C]_{eq}$*
Model	**DN24C8**	CH_2Cl_2	6.96×10^{-10}	7.78×10^{-7}	7.32×10^{-7}	$- 4.60 \times 10^{-8}$	- 0.059
1.1H$^+$	**DN24C8**	CH_2Cl_2	2.76×10^{-10}	1.07×10^{-7}	2.19×10^{-7}	1.12×10^{-7}	+ 1.047
1.11H$^+$	**DN24C8**	CH_2Cl_2	2.44×10^{-9}	2.45×10^{-7}	9.96×10^{-7}	7.51×10^{-7}	+ 3.065
1.13H$^+$	**DB24C8**	CH_2Cl_2	3.56×10^{-9}	1.31×10^{-5}	2.09×10^{-5}	7.80×10^{-6}	+ 0.611
1.14H$^+$	**DB24C8**	CH_3CN	1.10×10^{-10}	4.89×10^{-5}	4.91×10^{-5}	2.00×10^{-7}	+ 0.004

Table 1.6: Flux (J) and concentration of free ring at the equilibrium ($[C]_{eq}$), at the dissipative state ($[C]_{diss}$) and the absolute ($\Delta[C]$) and relative ($\Delta[C]/[C]_{eq}$) variation of concentration between dissipative and equilibrium states.

In order to explore the effect of the concentration and/or of the photon fluxes on the dissipative behaviour, simulations have been performed on all the systems at two set of concentrations, to mimic the NMR or UV-vis experimental setup:

"NMR": $[C] = [E] = 1 \times 10^{-3}$ M

"UV-vis": $[C] = 5.0 \times 10^{-5}$ M; $[E] = 1.5 \times 10^{-4}$ M

Three sets of photon fluxes were computed, as reported below:

"Standard": $q = 2.8 \times 10^{-8}$ Einstein/s for 5 minutes, then 1.7×10^{-9} Einstein/s

"High": $q = 2.8 \times 10^{-8}$ Einstein/s

"Low": $q = 1.7 \times 10^{-9}$ Einstein/s

In the following discussion, for the sake of simplicity, only the concentration of free ring will be analysed. The profiles at different photon fluxes will be compared within the same experimental set.

In the model system (figure 1.26) the concentration of free ring in the UV-vis simulation is below the equilibrium concentration. As already reported, this state is not compatible with any *E*/*Z* mixture and can only be accessed under continuous light irradiation. Moreover, the higher is the photon flux, the lower is the concentration. Interestingly, when the photon flux is low, before reaching the dissipative regime, the concentration of free ring drops significantly. However, in the NMR simulation, if the photon flux is high, the concentration of free ring is below that at the equilibrium, whereas if the flux is low, the concentration is much higher. Despite in this last condition it is less straightforward to demonstrate that the system operates out of equilibrium, the gap between the final concentration and the initial one is large enough to produce a clear signal with the experimental technique. The *J* fluxes are reported in table 1.7. For further insights on this model system, interested readers can refer to the latest work of Ragazzon et al.[28]

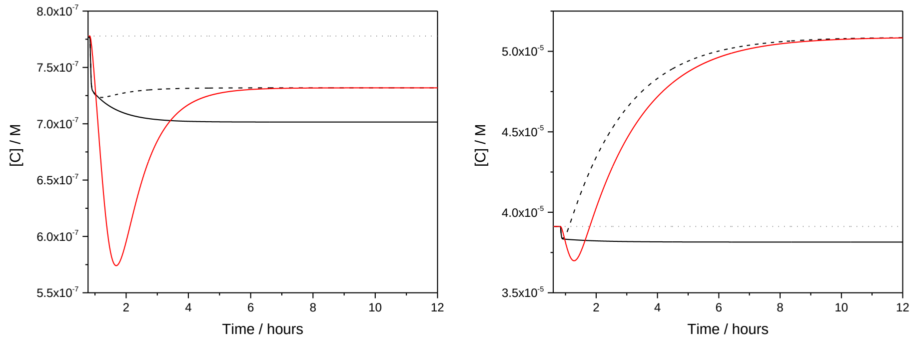

Figure 1.26: UV-vis (left) and NMR (right) simulations for the model system. The dotted grey line represents the equilibrium value, the dashed black line the standard curve, the full black line the high flux curve and the full red line the low flux curve.

Set	***q / Einstein s^{-1}***	***Δ[C] / M***	***Δ[C] / [C]$_{eq}$***	***J / M s^{-1}***
UV-vis standard	2.8×10^{-8} then 1.7×10^{-9}	$- 4.6 \times 10^{-8}$	- 0.059	6.96×10^{-10}
UV-vis high	2.8×10^{-8}	$- 7.5 \times 10^{-8}$	- 0.096	7.08×10^{-10}
UV-vis low	1.7×10^{-9}	$- 4.6 \times 10^{-8}$	- 0.059	6.96×10^{-10}
NMR standard	2.8×10^{-8} then 1.7×10^{-9}	$+ 1.18 \times 10^{-5}$	+ 0.302	9.57×10^{-9}
NMR high	2.8×10^{-8}	$- 1.00 \times 10^{-6}$	- 0.026	1.36×10^{-8}
NMR low	1.7×10^{-9}	$+ 1.18 \times 10^{-5}$	+ 0.302	9.57×10^{-9}

Table 1.7: Photon fluxes (q), J fluxes and the absolute (Δ[C]) and relative (Δ[C]/[C]$_{eq}$) variation of concentration between dissipative and equilibrium states for all the set of data for the model system.

In the system based on axle **1.1**H$^+$ and **DN24C8** in CH_2Cl_2 (figure 1.27), in both the UV-vis and the NMR setups, the concentration of free ring at the dissipative state is higher than the equilibrium one, but in the first few hours of irradiation the value is lower. Moreover, when the photon flux is high, the time required to reach the dissipative state is lower, thus signifying that, in this case, the photochemical processes are the rate determining steps. In the UV-vis simulation, the *J* flux (table 1.8) is unexpectedly higher when the photon flux is lower, and in any case the values are lower than for the model compound, in contrast with the more favourable kinetic and thermodynamic parameters.

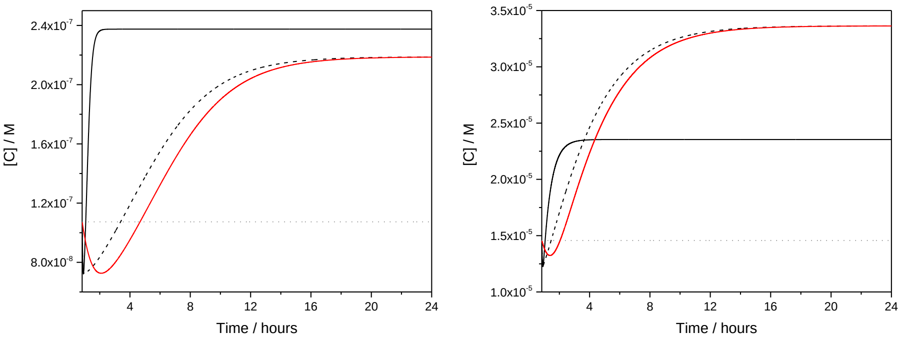

*Figure 1.27: UV-vis (left) and NMR (right) simulations for the system **1.1**H$^+$ - **DN24C8** in CH_2Cl_2. The dotted grey line represents the equilibrium value, the dashed black line the standard curve, the full black line the high flux curve and the full red line the low flux curve.*

Set	*q / Einstein s^{-1}*	*Δ[C] / M*	*Δ[C] / [C]$_{eq}$*	*J / M s^{-1}*
UV-vis standard	2.8×10^{-8} then 1.7×10^{-9}	$+ 1.12 \times 10^{-7}$	+ 1.047	2.76×10^{-10}
UV-vis high	2.8×10^{-8}	$+ 1.31 \times 10^{-7}$	+ 1.224	2.69×10^{-10}
UV-vis low	1.7×10^{-9}	$+ 1.12 \times 10^{-7}$	+ 1.047	2.76×10^{-10}
NMR standard	2.8×10^{-8} then 1.7×10^{-9}	$+ 1.90 \times 10^{-5}$	+ 1.301	1.98×10^{-9}
NMR high	2.8×10^{-8}	$+ 8.90 \times 10^{-6}$	+ 0.609	4.86×10^{-8}
NMR low	1.7×10^{-9}	$+ 1.90 \times 10^{-5}$	+ 1.301	1.98×10^{-9}

*Table 1.8: Photon fluxes (q) and J fluxes for all the set of data for the system **1.1**H$^+$ - **DN24C8** in CH_2Cl_2.*

The system formed by axle **1.11**H$^+$ and **DN24C8** in CH_2Cl_2 (figure 1.28), in the UV-vis setup, reaches a dissipative state whose concentration is substantially unchanged by the photon flux and larger than equilibrium concentration, but the time required is larger for low photon fluxes. In the NMR setup, a similar scenario is displayed, even though high photon fluxes produce slightly lower concentrations of free ring. As it happens for compound **1.1**H$^+$, even in this system the photochemical processes are the rate determining steps. In addition, the relative concentration variation (*Δ[C]/[C]$_{eq}$*, table 1.9) reaches very high values, up to 3.08 in the UV-vis. The *J* fluxes, reported in table 1.9, are overall larger than for the model compound, suggesting that the efficiency of this system is larger, despite the lack of selectivity.

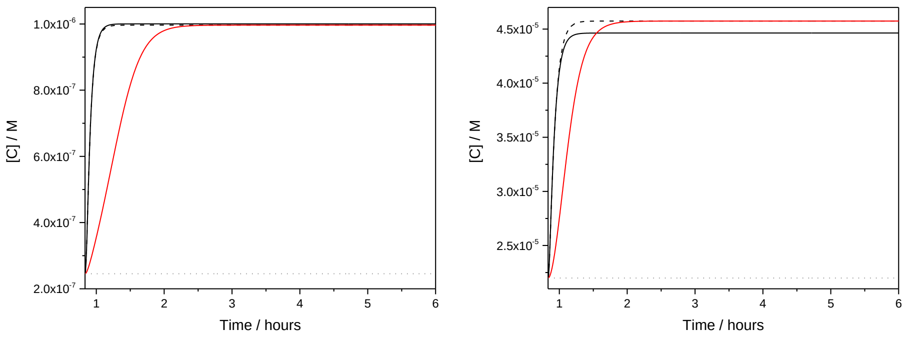

*Figure 1.28: UV-vis (left) and NMR (right) simulations for the system **1.11**H$^+$ - **DN24C8** in CH_2Cl_2. The dotted grey line represents the equilibrium value, the dashed black line the standard curve, the full black line the high flux curve and the full red line the low flux curve.*

Set	*q / Einstein s^{-1}*	*Δ[C] / M*	*Δ[C] / [C]$_{eq}$*	*J / M s^{-1}*
UV-vis standard	2.8×10^{-8} then 1.7×10^{-9}	$+ 7.51 \times 10^{-7}$	+ 3.065	2.44×10^{-9}
UV-vis high	2.8×10^{-8}	$+ 7.55 \times 10^{-7}$	+ 3.081	2.55×10^{-9}
UV-vis low	1.7×10^{-9}	$+ 7.51 \times 10^{-7}$	+ 3.065	2.44×10^{-9}
NMR standard	2.8×10^{-8} then 1.7×10^{-9}	$+ 2.37 \times 10^{-7}$	+ 1.077	1.56×10^{-8}
NMR high	2.8×10^{-8}	$+ 2.26 \times 10^{-7}$	+ 1.027	4.41×10^{-8}
NMR low	1.7×10^{-9}	$+ 2.37 \times 10^{-7}$	+ 1.077	1.56×10^{-8}

*Table 1.9: Photon fluxes (q), J fluxes and the absolute (Δ[C]) and relative (Δ[C]/[C]$_{eq}$) variation of concentration between dissipative and equilibrium states for all the set of data for the system **1.11**H$^+$ - **DN24C8** in CH_2Cl_2.*

The system **1.13**H$^+$ - **DB24C8** in CH_2Cl_2 (figure 1.29) shows similar features in the UV-vis and NMR setups. Indeed, in both cases the concentration at the dissipative state is higher than that of the equilibrium and increases with the photon fluxes. Due to the low kinetic constants, however, the time required to the system to reach the dissipative state is more than two days in the UV-vis setup and more than one day in the NMR simulation. Remarkably, despite the large operating timescales and the lack of evidences of a possible selectivity, this system shows the highest net flux, up to 1×10^{-7} M s^{-1} in the UV-vis setup (table 1.10).

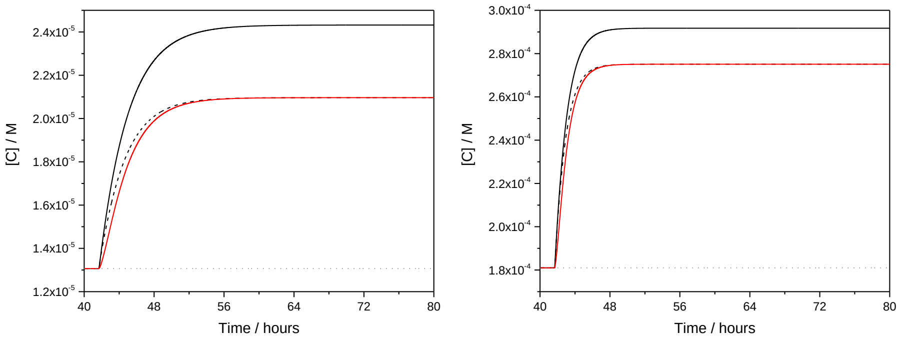

Figure 1.29: UV-vis (left) and NMR (right) simulations for the system ***1.13**H$^+$ - **DB24C8*** *in* CH_2Cl_2. *The dotted grey line represents the equilibrium value, the dashed black line the standard curve, the full black line the high flux curve and the full red line the low flux curve.*

Set	***q / Einstein s^{-1}***	***Δ[C] / M***	***Δ[C] / [C]$_{eq}$***	***J / M s^{-1}***
UV-vis standard	2.8×10^{-8} then 1.7×10^{-9}	$+ 8.00 \times 10^{-6}$	+ 0.611	3.56×10^{-9}
UV-vis high	2.8×10^{-8}	$+ 1.13 \times 10^{-5}$	+ 0.862	3.69×10^{-9}
UV-vis low	1.7×10^{-9}	$+ 8.00 \times 10^{-6}$	+ 0.611	3.56×10^{-9}
NMR standard	2.8×10^{-8} then 1.7×10^{-9}	$+ 9.40 \times 10^{-5}$	+ 0.519	9.85×10^{-8}
NMR high	2.8×10^{-8}	$+ 1.11 \times 10^{-4}$	+ 0.617	1.02×10^{-7}
NMR low	1.7×10^{-9}	$+ 9.40 \times 10^{-5}$	+ 0.519	9.85×10^{-8}

Table 1.10: Photon fluxes (q), J fluxes and the absolute (Δ[C]) and relative (Δ[C]/[C]$_{eq}$) variation of concentration between dissipative and equilibrium states.for all the set of data for the system ***1.13**H$^+$ - **DB24C8*** *in* CH_2Cl_2.

For the last system studied, **1.14**H⁺ - **DB24C8** in CH_3CN (figure 1.30), different photon fluxes produce the higher discrepancy between the dissipative concentrations (table 1.11). Indeed, low photon fluxes lead to a situation where $[C]_{diss} > [C]_{eq}$, while high photon fluxes lead to a situation where $[C]_{diss} < [C]_{eq}$, the latter with a larger gap $\Delta[C] / [C]_{eq}$. As a matter of fact, in the present case it is more convenient to work with high photon fluxes, as in the experiment reported in figure 1.24. It is noteworthy that, for this system, the concentration of the free ring reported in table 1.11 can be accessed only upon light irradiation.

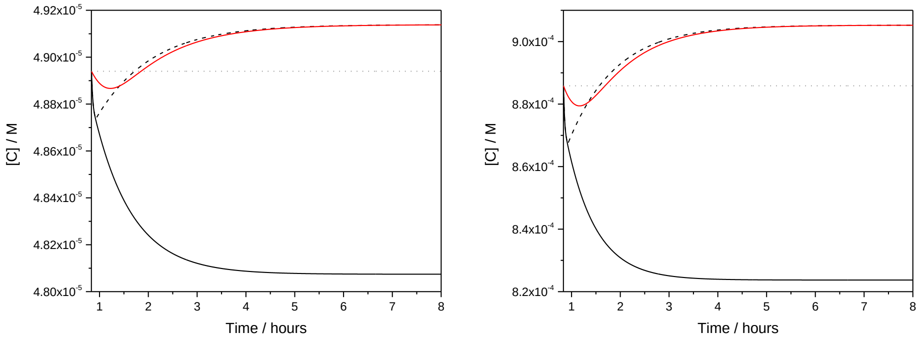

*Figure 1.30: UV-vis (left) and NMR (right) simulations for the system **1.14**H⁺ - **DB24C8** in CH_3CN. The dotted grey line represents the equilibrium value, the dashed black line the standard curve, the full black line the high flux curve and the full red line the low flux curve.*

Set	*q / Einstein s⁻¹*	*Δ[C] / M*	*Δ[C] / [C]$_{eq}$*	*J / M s⁻¹*
UV-vis standard	2.8×10^{-8} then 1.7×10^{-9}	$+ 2.00 \times 10^{-7}$	+ 0.004	1.10×10^{-10}
UV-vis high	2.8×10^{-8}	$- 8.00 \times 10^{-7}$	- 0.016	1.11×10^{-9}
UV-vis low	1.7×10^{-9}	$+ 2.00 \times 10^{-7}$	+ 0.004	1.10×10^{-10}
NMR standard	2.8×10^{-8} then 1.7×10^{-9}	$+ 2.00 \times 10^{-5}$	+ 0.022	1.10×10^{-8}
NMR high	2.8×10^{-8}	$- 6.30 \times 10^{-5}$	- 0.071	9.93×10^{-8}
NMR low	1.7×10^{-9}	$+ 2.00 \times 10^{-5}$	+ 0.022	1.10×10^{-8}

*Table 1.11: Photon fluxes (q), J fluxes and the absolute (Δ[C]) and relative (Δ[C]/[C]$_{eq}$) variation of concentration between dissipative and equilibrium states for all the set of data for the system **1.14**H⁺ - **DB24C8** in CH_3CN.*

1.7 Conclusion and perspectives

In the present work, a series of novel molecular components for a light-driven supramolecular pump have been characterized. In order to improve the efficiency of the motor and allow its possible implementation in more complex smart architectures, three strategies were adopted. The first route is the derivatization of the azobenzene unit in *p′* position. Compound **1.1**H$^+$, bearing a *p′*-cyanoazobenzene resulted to have favourable energetic requirements, but the isolated compound has an erratic behaviour under irradiation, which prevents the correct dissipative operation. However, the pseudorotaxane formed with crown **DN24C8** resulted to be photochemically improved with respect to the free axle. The second strategy deals with the choice of an alternative pseudostopper, and has been preceded by a survey on a series of symmetric ammonium salts. Among them, the *2,5*-dimethylbenzyl group was found to possess the correct kinetic features, and therefore it was implemented in a new generation of molecular axles. Compound **1.11**H$^+$, which differs from the model compound for the pseudostopper moiety, showed similar threading kinetics with the crown on the two extremities of the axle. The supramolecular system based on this compound can operate only partially as a motor, due to the lack of unidirectionality in the threading process, but it can reach in any case a dissipative state under continuous irradiation. Moreover, its behaviour helped to clarify that the threading kinetics of one axle with two accessible gates is the sum of the kinetics of each gate, and that a proper selectivity is achieved if they differ for at least two order of magnitude. The last strategy aimed at prompting a larger destabilization of the *Z* pseudorotaxane, by displacing the methylenic bridge between the ammonium site and the azobenzene in *ortho* or *meta* position. The *ortho* derivative **1.13**H$^+$ exhibited an unusual fast thermal back isomerization ($k_{\Delta} = 10^{-3}\ s^{-1}$), and a slow threading kinetics with crown **DB24C8**, most likely as a consequence of an intramolecular hydrogen bonding between the ammonium and the azobenzene units. Therefore, the threading occurs either through the pseudostopper side or through both the extremity with low rates. The lack of evidences for the threading in the *Z* form does not allow to determine whether the supramolecular system in this axle can work as a molecular switch, or, as for compound **1.11**H$^+$, both as a switch or a motor. On the other hand, the *meta* derivative **1.14**H$^+$ works as a motor in CH_3CN, as it threads into **DB24C8** from the *E*-azobenzene extremity, and dethreads through the pseudostopper when in the *Z* configuration. Indeed, NMR experiments conducted under continuous light irradiation, clearly revealed a stationary dissipative state, where the concentration of each species is not compatible with the chemical equilibrium. Therefore, **1.14**H$^+$ is the most promising candidate for the new generation of light-activated molecular pumps. The experimental findings were supported by kinetic simulations which evidenced that any system possesses a peculiar behaviour and optimal working conditions. In addition, the simulations revealed that the higher values of net flux under dissipative conditions is obtained with the system **1.13**H$^+$ - **DB24C8**, even with the unfavourable energetic features and the lack of selectivity.

These preliminary results are of cardinal importance in understanding the effect that the functionalization exerts on the whole supramolecular systems. Moreover, the implementation of the pumping module cannot disregard a thorough investigation of the molecular components, in order to achieve a high-performance material. On the basis of these findings, high-complexity architectures are being realized in the research group, such as a stoppered rotaxane with a reservoir site for many crown ethers, able to convert and store light into chemical energy and release it in the dark, or a catenate system able to unidirectionally rotate one ring with respect to the other. In a future scenario, the supramolecular pump could be inserted in liposomal membranes in order to pump crown ethers into vesicles against gradient, or endowed with a polymeric chain and travel across the crown ethers of another polymeric chain to weave a supramolecularly-reticulated polymer under light irradiation and unthread it in the dark, like in the myth of the Penelope's canvas.

1.8 References

1. D. S. Goodsell, *Bionanotechnology: Lessons from Nature*, Wiley-Liss, Inc., **2004**.
2. W. R. Browne and B. L. Feringa, *Nat. Nanotechnol.*, **2006**, *1*, 1, 25–35.
3. M. Baroncini, S. Silvi, and A. Credi, *Chem. Rev.*, **2019**, DOI: 10.1021/acs.chemrev.9b00291.
4. M. Baroncini, L. Casimiro, C. de Vet, J. Groppi, S. Silvi, and A. Credi, *Chem. Open*, **2018**, *7*, 2, 169–179.
5. M. Baroncini, S. Silvi, M. Venturi, and A. Credi, *Angew. Chem. Int. Ed.*, **2012**, *51*, 17, 4223–4226.
6. G. Ragazzon, M. Baroncini, S. Silvi, M. Venturi, and A. Credi, *Nat. Nanotechnol.*, **2015**, *10*, 1, 70–75.
7. L. Casimiro, J. Groppi, M. Baroncini, M. La Rosa, A. Credi, and S. Silvi, *Photochem. Photobiol. Sci.*, **2018**, *17*, 734–740.
8. C. Cheng, P. R. McGonigal, W.-G. Liu, *et al.*, *J. Am. Chem. Soc.*, **2014**, *136*, 42, 14702–14705.
9. P. R. McGonigal, H. Li, C. Cheng, *et al.*, *Tetrahedron Lett.*, **2015**, *56*, 23, 3591–3594.
10. C. Cheng, P. R. McGonigal, S. T. Schneebeli, *et al.*, *Nat. Nanotechnol.*, **2015**, *10*, 547–553.
11. C. Pezzato, M. T. Nguyen, D. J. Kim, O. Anamimoghadam, L. Mosca, and J. F. Stoddart, *Angew. Chem. Int. Ed.*, **2018**, *57*, 30, 9325–9329.
12. P. Hoffmann, *Life's Ratchet. How Molecular Machines Extract Order from Chaos,* Basic Books, **2012**.
13. E. R. Kay, D. A. Leigh, and F. Zerbetto, *Angew. Chem. Int. Ed.*, **2007**, *46*, 1-2, 72–191.
14. R. D. Astumian, *Phys. Chem. Chem. Phys.*, **2007**, *9*, 37, 5067–5083.
15. V. Serreli, C.-F. Lee, E. R. Kay, and D. A. Leigh, *Nature*, **2007**, *445,* 7127, 523–527.

16. M. Baroncini, S. Silvi, M. Venturi, and A. Credi, *Chem. Eur. J.*, **2010**, *16*, 38, 11580–11587.

17. G. Tabacchi, S. Silvi, M. Venturi, A. Credi, and E. Fois, *Chem. Phys. Chem.*, **2016**, *17*, 12, 1913–1919.

18. R. D. Astumian, *Nat. Nanotechnol.*, **2012**, *7*, 684–688.

19. G. Ragazzon and L. J. Prins, *Nat. Nanotechnol.*, **2018**, *13*, 10, 882–889.

20. L. Casimiro, *Threadlike components for photoactivated molecular pumps*. Master thesis, **2016**.

21. H. Rau, *Photochromism. Molecules and Systems,* Elsevier, Amsterdam, **1990**.

22. H. M. D. Bandara and S. C. Burdette, *Chem. Soc. Rev.*, **2012**, *41*, 5, 1809–1825.

23. M. Lohse, K. Nowosinski, N. L. Traulsen, *et al.*, *Chem. Commun.*, **2015**, *51*, 48, 9777–9780.

24. P. R. Ashton, E. J. T. Chrystal, P. T. Glink, *et al.*, *Chem. Eur. J.*, **1996**, *2*, 6, 709–728.

25. H. Mauser and G. Gauglitz, *Photokinetics : theoretical fundamentals and applications,* Amsterdam, Elsevier, **1998**.

26. *https://berkeley-madonna.myshopify.com*.

27. H. M. D. Bandara, T. R. Friss, M. M. Enriquez, *et al.*, *J. Org. Chem.*, **2010**, *75*, 14, 4817–4827.

28. A. Sabatino, E. Penocchio, G. Ragazzon, A. Credi, and D. Frezzato, *Angew. Chem. Int. Ed.*, **2019**, DOI: 10.1002/anie.201908026.

29. H. Asanuma, X. Liang, and M. Komiyama, *Tetrahedron Lett.*, **2000**, *41*, 7, 1055–1058.

30. C. Ruslim and K. Ichimura, *J. Mater. Chem.*, **2000**, *10*, 12, 2704–2707.

31. A. A. Beharry and G. A. Woolley, *Chem. Soc. Rev.*, **2011**, *40*, 8, 4422–4437.

32. P. R. Ashton, E. J. T. Chrystal, P. T. Glink, *et al.*, *Chem. Eur. J.*, **1996**, *2*, 6, 709–728.

Chapter 2.

Supramolecular tuning of photochromism in terarylene-based pseudorotaxanes

2.1 Introduction and aim

In molecular devices, photochromism is generally employed to exert light-controlled movements or functions.[1–3] In this regard, a deep investigation on how the photoreactivity of a photochrome is retained or modulated after a chemical or supramolecular modification is of pivotal importance. The chemical modification of the photochromic behaviour, called *gated photochromism*, is rather uncommon, and has been achieved by means of transition metal coordination,[4,5] reversible chemical modification,[6,7] supramolecular self-assembly,[8,9] or formation of inclusion complexes.[10–14] So far, only one photochromic system gated by a [2]pseudorotaxane formation event has been reported. In 2015, Hecht et al. described an azobenzene-based axle whose photoisomerization can be locked and unlocked by threading or dethreading, respectively, in a crown ether host.[15]

The study herewith reported has been conducted in collaboration with the group of Prof. Stephen J. Loeb at the University of Windsor (Canada) on photochromic pseudorotaxanes based on terarylenes.[16] Terarylenes are diarylethenes where the bridging unit (*i.e.*, the central ethylenic bond) is an aromatic (hetero)cycle. In dark conditions, these compounds exist in their *open* form (from now on indicated *o*), where the two arenic units are not linked together. Under UV irradiation, the latter undergo a [4+4] photocycloaddition, leading to the *closed* (*c*) form. Usually, the open form is colourless, whereas the fully conjugated closed form is violet or blue coloured. Irradiation in the visible region can afford the cycloreversion and restore the initial open form. Differently from diarylethenes, which are, in most of the cases P-type photochromes, terarylenes can be also T-type photochromes, meaning that the cycloreversion can be accessed even at room temperature.[17–19]

In the present case, the threadlike components **2.1**-**2.3**H$^+$ are 4,5-bis(benzothienyl)-2-phenylimidazolium ions. In case of compounds **2.2**H$^+$ and **2.3**H$^+$, the hydrogen atom in *para* position on the phenyl ring, is derivatized with a methylesther group or a methoxy group, respectively (figure 2.1). The imidazolium bridging unit can represent a valid recognition site for crown ethers to yield supramolecular adducts, like [2]pseudorotaxanes, [2]rotaxanes and [3]rotaxanes.[20–26] Interestingly, the rigidity of these imidazole-based axles also allowed its incorporation into metal–organic frameworks (MOFs).[27–30] Despite the widespread use of terarylenes as molecular photoswitches,[17,19] only few examples of [2]pseudorotaxanes and [2]rotaxanes[31–33] containing this moiety as a structural component or signalling unit have been reported. As such, the photophysical, photochemical and supramolecular characterization of the isolated axles **2.1**-**2.3**H$^+$ and of their pseudorotaxanes formed with either [24]crown-8 (**24C8**) or dibenzo-[24]crown-8 (**DB24C8**) will be shown. A particular focus will be devoted to how the photochromic properties are changed from the molecular to the supramolecular species.

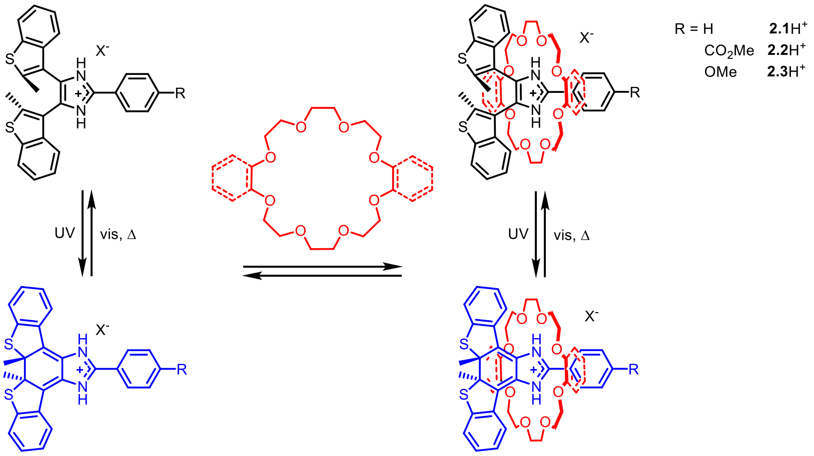

*Figure 2.1: Isomerization reactions (vertical processes) and formation of [2]pseudorotaxanes (horizontal processes) between compounds **2.1**-**2.3**H$^+$ and crown ethers **24C8** or **DB24C8**.*

2.2 Photochromism of the isolated axles

Compounds **2.1**, **2.2**, **2.3** were synthesized in the research group of Prof. S. Loeb (University of Windsor, Canada). The corresponding protonated forms, **2.1**H$^+$, **2.2**H$^+$, **2.3**H$^+$, were synthesized in form of BF_4^- salts. However, due to the poor stability of the latter (*vide infra*), all the studies on the protonated species and the supramolecular complexes were conducted using the corresponding neutral compound and protonating it by means of triflic acid (TfOH) as necessary. All the photochemical and supramolecular characterization was performed in dichloromethane (CH_2Cl_2), as this solvent is not competitive for the formation of the [2]pseudorotaxanes. The stability constants of the supramolecular species were determined also in deuterated acetonitrile (CD_3CN) via NMR by Dr. G. Baggi at the University of Windsor.

The absorption spectrum of the open form **2.1**o (figure 2.2) consists in a main band in the UV region, with an absorption coefficient of 25000 M^{-1} cm^{-1} at 305 nm. The compound is luminescent in the violet region of the spectrum, with an emission centred at 390 nm, a quantum yield (Φ_{em}) of 0.04 and a lifetime of 3.3 ns.

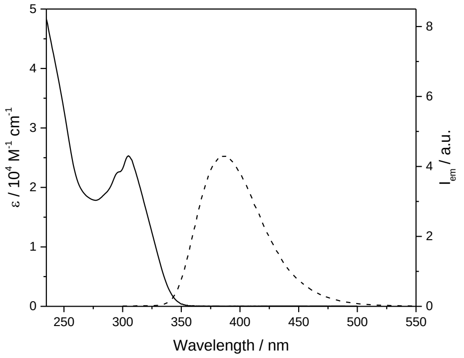

*Figure 2.2: Absorption (full line) and emission (dashed line) spectra of **2.1**o in CH_2Cl_2.*

Irradiation of **2.1**o in the UV region affords the photocycloaddition and produce the closed form **2.1**c, characterized by a large absorption in the visible region (hence the violet colour of the solution), with a main band around 600 nm (figure 2.3, left). However, after a first uprising, prolonged irradiations lead to a decrease and broadening of these bands in the visible region and to the loss of the isosbestic points. This trend would suggest that, under prolonged irradiation, the compound undergoes an irreversible photodegradation.[18]

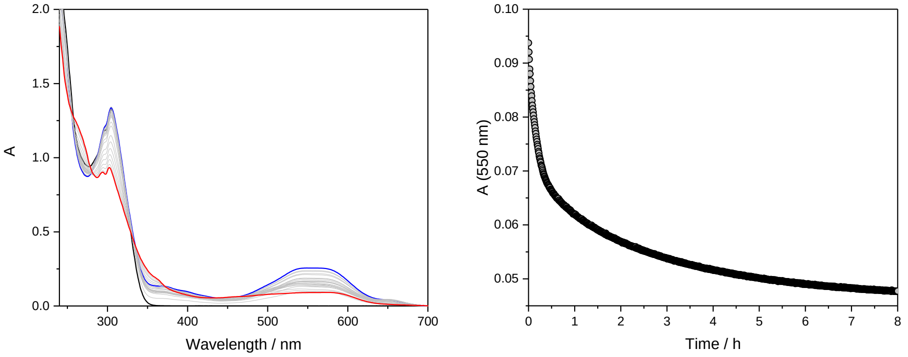

Figure 2.3: Left: absorption variations of a solution 5.6 × 10^{-5} M of ***2.1*** *upon prolonged irradiation. The blue line indicates the maximum conversion reached (t = 90 s), whereas the red line indicates the spectrum obtained after 2 hours of irradiation; right: absorbance changes over time at 550 nm of an irradiated solution of* ***2.1****c.*

The metastable closed form **2.1**c is short-lived and reverts to the open form by thermal cycloreversion within few hours. The kinetic profile of this isomerization reaction is not compatible with a first-order process (figure 2.3, right). Moreover, the initial absorption spectrum is not recovered. These findings would corroborate the hypothesis of the genesis of an irreversible photoproduct of the closed isomer, which absorbs in the visible region and is still present after the cycloreversion reactions.

Compound **2.1**oHBF4 appeared to be unstable in the conditions of the UV-vis spectroscopic experiments, *i.e.*, in CH_2Cl_2 solutions with concentrations ranging from 10^{-4} to 10^{-6} M. In particular, the absorption changes suggest that the imidazolium unit undergoes a deprotonation reaction either in time or by dilution (figure 2.4). From the deconvolution of the absorption spectra at several concentrations, it was possible to obtain the ratio between the protonated and the neutral form in the mixture. Consequently, the acidity constant of the imidazolium was estimated, and resulted to be $K_a = 4.8 \times 10^{-6}$ M ($pK_a = 5.32$).

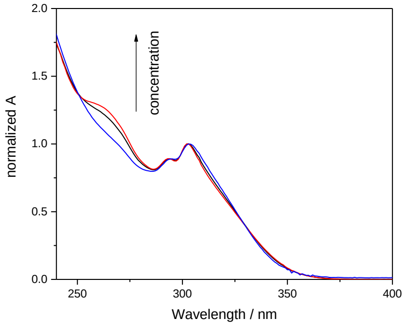

*Figure 2.4: Normalized absorption spectra of 1.0 × 10^{-3} M (red), 1.0 × 10^{-4} M (black) and 1.0 × 10^{-5} M (blue) solutions of **2.1**oHBF$_4$.*

In order to overcome the stability issue, in the measurements reported below, compounds **2.1**o-**2.3**oHTfO were prepared in situ just before performing the experiment, by adding a stoichiometric amount of TfOH to a solution of **2.1**o-**2.3**o. Henceforth, the counterion TfO$^-$ will be omitted for clarity.

The absorption and emission spectra of compounds **2.1**o-**2.3**oH$^+$ are reported in figure 2.5, and their photophysical data are gathered in table 2.1. All the compounds show a strong luminescence, with quantum yields up to 0.41, as for **2.2**oH$^+$ (table 2.1).

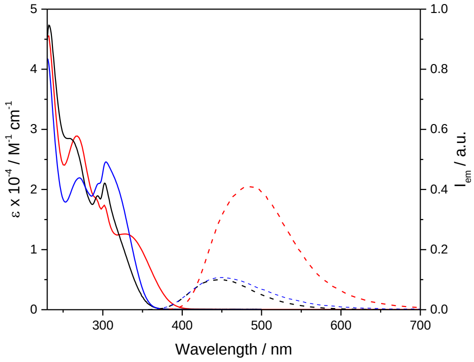

*Figure 2.5: Absorption (full lines) and emission (dashed lines) of compounds **2.1**oH$^+$ (black), **2.2**oH$^+$ (red), **2.3**oH$^+$ (blue) in CH$_2$Cl$_2$.*

	Absorption		*Emission*		
Compound	*λ_{abs} / nm*	*ε / M^{-1} cm^{-1}*	*λ_{em} / nm*	*Φ_{em}*	*τ / ns*
2.1oH$^+$	258 303	28500 21500	450	0.10	2.9
2.2oH$^+$	268 302 330	29000 17400 12600	480	0.41	3.1
2.3oH$^+$	270 304	22000 24600	430	0.11	1.8

*Table 2.1: Photophysical properties of compounds **2.1**oH$^+$, **2.2**oH$^+$ and **2.3**oH$^+$ in CH_2Cl_2.*

Photochemical experiments were performed by irradiation with UV light. As it happened for compound **2.1**, all the protonated compounds exhibit low fatigue resistance: after prolonged irradiation the shape of the absorption spectra changes and the isosbestic points are not maintained anymore. For this reason, it was not possible to reach any photostationary state, but all the compounds were irradiated up to the maximum degree of photoconversion (α_c), and the irradiation was stopped before starting to degrade the molecule. In general, the irradiation time that enables to reach the maximum extent of photoconversion was determined by irradiating the samples for short intervals, and checking the absorption spectra after each interval. In this regard, it was found out that a single long irradiation slot produced larger amounts of closed form with respect to several short irradiation slots. Moreover, since the closed isomers of all the compounds undergo a relatively fast cycloreversion back reaction at room temperature, the percentage of photoconversion could be only estimated from the emission spectra. Since the closed form of none of the compounds is emissive, the ratio between the initial (*i.e.,* before irradiation) and residual (*i.e.,* immediately after irradiation) luminescence intensity provides an estimation of the fraction of the open isomer in the photolyzed mixture (table 2.2).

Compounds **2.1**oH$^+$ and **2.3**oH$^+$ can be converted to the corresponding closed forms upon irradiation at 313 nm: the photoisomerization reactions are accompanied by the appearance of the typical bands in the visible region.[17–19] The closed forms **2.1**cH$^+$ and **2.3**cH$^+$ revert back to the open forms in tens of minutes, but, surprisingly, in both cases the absorbance changes linearly with time, *i.e.*, the cycloreversion reactions follow a zero-order kinetic rate law (figure 2.6). Such mechanism is quite uncommon and can be ascribed to a catalytic chain reaction. For instance, it has been reported for related compounds, that an external oxidant can accelerate the thermal back reaction and the kinetics follow a zero-order reaction dynamic.[34,35] However, in our system no electroactive species are present, and oxidation processes can be ruled out. In order to exclude any effect related to the presence of impurities or humidity in the solvent, control experiments in different batches of CH_2Cl_2, also dried out with molecular sieves, were attempted, but the kinetic traces always followed a zero-order profile. Therefore, it was hypothesized that the proton and/or the counterion play a role in the thermal cycloreversion reaction (see paragraph 2.4).[36–38]

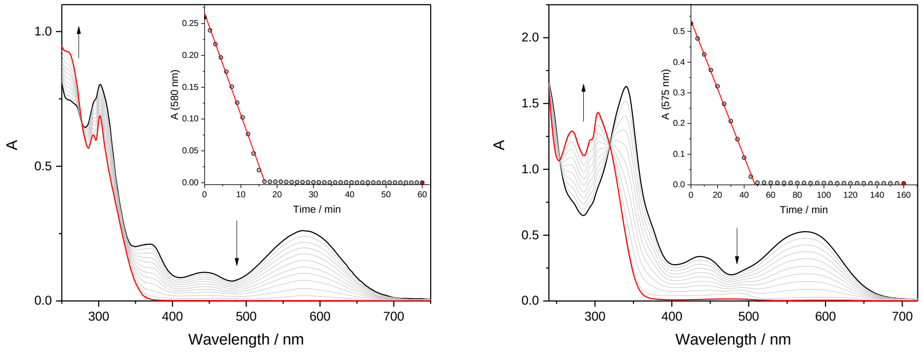

Figure 2.6: Absorption spectra of a 3.2 × 10^{-5} M solution of ***2.1****cH$^+$ (left) and of a 6.0 × 10^{-5} M solution of* ***2.3****cH$^+$ (right) after irradiation at 313 nm; inset: absorption changes over time (empty circles) at 580 nm (left) and at 545 nm (right) with a linear fitting (red line);*

The closed form **2.2**cH$^+$, obtained upon irradiation of **2.2**oH$^+$ in the UV could not be accumulated, since its thermal cycloreversion is very fast and it is completed before the recording of the absorption spectrum. Moreover, the initial spectrum of **2.2**oH$^+$ could never be completely recovered. It is likely that, in this case, the photoreaction quantum yield is lower with respect to compounds **2.1**H$^+$ and **2.3**H$^+$, on consideration of the larger emission quantum yield, and that a severe photodegradation occurs. Nevertheless, the extent of photoconversion (α_c) could be estimated, in analogy with the other compounds, by evaluating the extent of emission quenching at the end of the irradiation experiment (table 2.2).

Compound	*α_c (313 nm)*	*k_Δ / M s^{-1}*	*order*
2.1H^+	0.56	1.8×10^{-8}	0
2.2H^+	0.30	N.A.	--
2.3H^+	0.80	1.7×10^{-8}	0

Table 2.2: Photoconversion (α_c) and cycloreversion kinetics of compounds ***2.1****-****2.3****oH^+.*

2.3 [2]Pseudorotaxanes formation

The formation of [2]pseudorotaxanes with the crown ethers **24C8** and **DB24C8** was investigated by means of UV-vis absorption titrations (figures 2.7 and 2.8, table 2.3). In all cases, the absorption changes upon addition of the crown ether follow an opposite trend with respect to that obtained upon addition of triflic acid. This behaviour is in line with the sharing of the proton between the axle and the macrocycle. Moreover, upon complexation, the emission bands of the open isomers are generally quenched and blueshifted with respect to the corresponding isolated axle (see table 2.3). A global analysis of the absorption spectra obtained from the titration experiments highlighted different trends at different wavelengths. These results would suggest that, besides the 1:1 association, more complex equilibria could be involved, like, for instance, the formation of adducts with more complex stoichiometries or competitions between the crown and the thread for the proton. Nevertheless, these findings are not supported by NMR spectra, where only the formation of a 1:1 complex is evidenced. In order to mimic the conditions of the NMR experiments, UV-vis titrations were repeated on more concentrated solutions (around 10^{-4} M), but without any significant discrepancy. In the absence of other experimental evidences that would support the involvement of other species, the simplest model was used to fit the data in the lower energy region of the absorption spectrum, where the profile of the titration curves is generally consistent with a 1:1 model. The estimated association constants in CH_2Cl_2 are gathered in table 2.3, together with the association constants in CD_3CN determined via NMR.

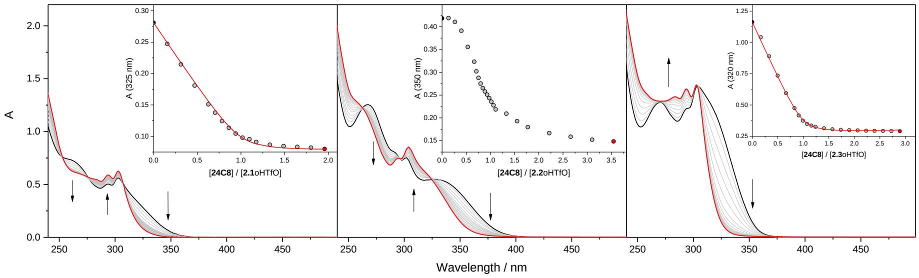

Figure 2.7: Absorption spectra upon titration of solutions of ***2.1****oH$^+$ (left), of* ***2.2****oH$^+$ (centre) and of* ***2.3****oH$^+$ (right) with concentrated* ***24C8****. The insets show the absorption changes (circles) and the fitting (red line) of the experimental data with a 1:1 model. Concentrations: [****2.1****oH$^+$] = 2.6 × 10^{-5} M, [****2.2****oH$^+$] = 4.5 × 10^{-5} M and [****2.3****oH$^+$] = 6.0 × 10^{-5} M.*

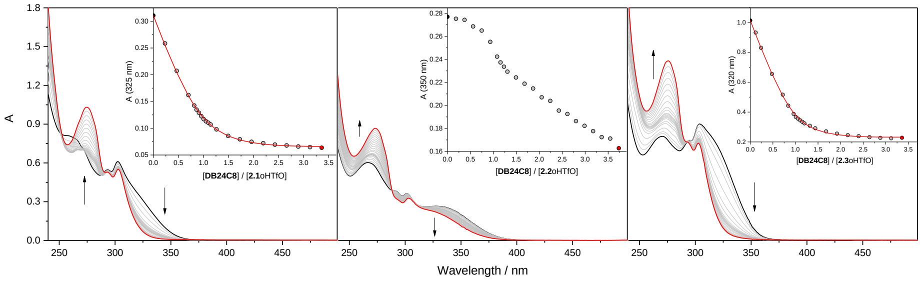

Figure 2.8: Absorption spectra upon titration of solutions of ***2.1****oH$^+$ (left), of* ***2.2****oH$^+$ (centre) and of* ***2.3****oH$^+$ (right) with concentrated* ***DB24C8****. The insets show the absorption changes (circles) and the fitting (red line) of the experimental data with a 1:1 model. Concentrations: [****2.1****oH$^+$] = 3.0 × 10^{-5} M, [****2.2****oH$^+$] = 3.0 × 10^{-5} M and [****2.3****oH$^+$] = 6.0 × 10^{-5} M.*

	Stability		***Emission***	
Pseudorotaxane	***K_c / M^{-1} (CH_2Cl_2)***	***K_c / M^{-1} (CD_3CN)***	***λ_{em} / nm***	***Φ_{em}***
[**2.1**oH⊃**24C8**]$^+$	2.3 × 10^6	380	440	0.05
[**2.1**oH⊃**DB24C8**]$^+$	2.9 × 10^5	300	400	0.03
[**2.2**oH⊃**24C8**]$^+$	N.A.	910	450	0.16
[**2.2**oH⊃**DB24C8**]$^+$	N.A.	800	470	0.17
[**2.3**oH⊃**24C8**]$^+$	9.7 × 10^5	290	370	0.07
[**2.3**oH⊃**DB24C8**]$^+$	2.5 × 10^5	200	430	0.10

Table 2.3: Stability constants and emission parameters of pseudorotaxanes formed between ***2.1****-****2.3****oH$^+$ and crown ethers* ***24C8*** *or* ***DB24C8****.*

On the basis of the electronic effect exerted from the substituent group on the phenyl ring, it could be argued that the complexes of **2.3**oH$^+$ would be the less stable, since the methoxy electron-donor group reduces the acidity of the imidazolium proton and therefore weakens its interaction with the crown ethers.[39] *Vice versa*, compound **2.2**oH$^+$ would form the most stable complexes, on account of the increased acidity due to the electron-withdrawing esther group. Indeed, the association constants in CD_3CN confirmed this order. In the same manner, in CH_2Cl_2, the stability constants of the pseudorotaxanes **2.3**oH$^+$ resulted to be lower with respect to those of **2.1**oH$^+$. Furthermore, for the same axle, the values of the stability constants are always lower for crown **24C8** than for **DB24C8**, most likely due to the larger stiffness of the latter. Once again, **2.2**oH$^+$ showed a different behaviour with respect to the other compounds: the absorption changes are qualitatively similar to the ones of the other compounds, but it is not possible to find any region in the absorption spectrum where the titration can be fitted with a 1:1 model, and therefore it was not possible to estimate the association constant. Apparently, the pseudorotaxanes containing compound **2.2**oH$^+$ are less stable than the other complexes. This observation is in contrast with the NMR results in CD_3CN and with the electron-withdrawing nature of the methyl ester substituent. On the other hand, as suggested also by the titration experiments, the stronger acidity of **2.2**oH$^+$ could promote the establishment of other competing equilibria, in which the proton is either shared in higher stoichiometries complexes or abstracted by the crown ether.

2.4 Photochromism of the [2]pseudorotaxanes

Mixtures of threads and crown ethers in equimolar concentrations were irradiated with UV light in order to assess if and how the complexation of the imidazolium unit affects the photoisomerization of the terarylenic unit, particularly in terms of thermal stability of the closed isomers. It could be argued that the pseudorotaxanes formed starting from the closed form of the axles can possess different association constants, with respect to the pseudorotaxanes in the open form. However, it was not possible to investigate this aspect due to the low thermal stability of the closed form of the free axles. In all cases the same stability issues of the free threads were observed, *i.e.*, degradation occurs upon prolonged irradiation and the PSS is never reached. Therefore, the same precautions as for the free threads were taken when irradiating the pseudorotaxane solutions: the irradiation was kept up to the maximum conversion and stopped before starting to degrade the molecules (figures 2.9 and 2.10).

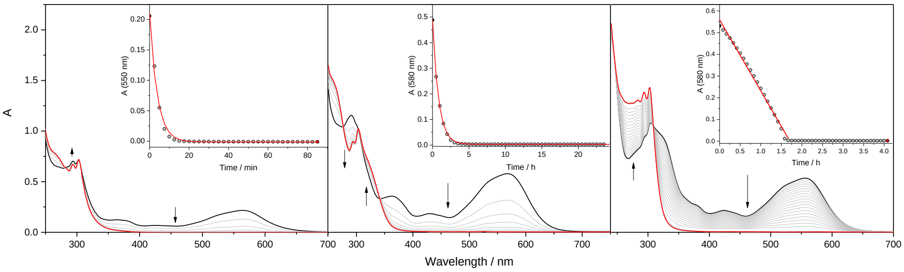

Figure 2.9: Absorption spectra of 1:1 mixtures of ***24C8*** *and* ***2.1****o*H^+ *(left),* ***2.2****o*H^+ *(centre) and* ***2.3****o*H^+ *(right) after irradiation at 313 nm (left, right) or 340 nm (centre). Insets: kinetic profile (circles) and fitting (red line) according to a first (left, centre) or zero-order (right) kinetic model. Concentrations: [****2.1****oH****24C8****] = 2.8 × 10*$^{-5}$ *M, [****2.2****oH****24C8****] = 4.6 × 10*$^{-5}$ *M and [****2.3****oH****24C8****] = 6.0 × 10*$^{-5}$ *M.*

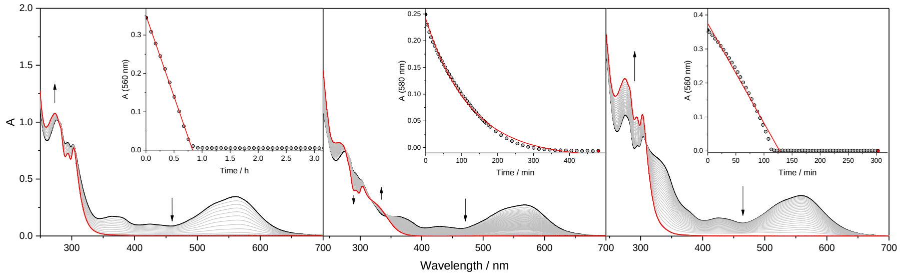

Figure 2.10: Absorption spectra of 1:1 mixtures of ***DB24C8*** *and* ***2.1****o*H^+ *(left),* ***2.2****o*H^+ *(centre) and* ***2.3****o*H^+ *(right) after irradiation at 313 nm. Insets: kinetic profile (circles) and fitting (red line) according to a first (centre) or zero-order (left, right) kinetic model. Concentrations: [****2.1****oH****24C8****] = 4.1 × 10*$^{-5}$ *M, [****2.2****oH****24C8****] = 3.0 × 10*$^{-5}$ *M and [****2.3****oH****24C8****] = 5.8 × 10*$^{-5}$ *M.*

Pseudorotaxane	α_c ***(λ_{irr} / nm)***	k_Δ	***order***
[**2.1**oH⊃**24C8**]$^+$	0.48 (313)	4.3 × 10^{-3} s^{-1}	1
[**2.1**oH⊃**DB24C8**]$^+$	0.53 (313)	8.3 × 10^{-9} M s^{-1}	0
[**2.2**oH⊃**24C8**]$^+$	0.74 (340)	3.4 × 10^{-4} s^{-1}	1
[**2.2**oH⊃**DB24C8**]$^+$	0.50 (313)	1.3 × 10^{-4} s^{-1}	1
[**2.3**oH⊃**24C8**]$^+$	0.76 (313)	7.9 × 10^{-9} M s^{-1}	0
[**2.3**oH⊃**DB24C8**]$^+$	0.61 (313)	4.5 × 10^{-9} M s^{-1}	0

Table 2.4: Photoconversions (α_c*) and cycloreversion properties of pseudorotaxanes formed between* ***2.1****-****2.3****o*H^+ *and crown ethers* ***24C8*** *or* ***DB24C8****.*

Pseudorotaxanes [**2.1**oH⊃**24C8**]$^+$ and [**2.1**oH⊃**DB24C8**]$^+$ photoisomerize to the closed form with percentages of photoconversion similar to the ones of the free thread (table 2.4). The bands in the visible region of the closed isomers are slightly different from the corresponding bands of the free thread, thus suggesting that the dethreading does not occur during irradiation. In the case of [**2.1**oH⊃**24C8**]$^+$, the photochromism was improved: the thermal cycloreversion reaction was completed within 30 minutes, but the kinetic profile was compatible with a first order model, with a rate constant of 4.3×10^{-3} s^{-1}. The experiments were repeated at larger concentrations (4×10^{-4} M), in order to mimic the NMR experimental conditions, but in that case the thermal cycloreversion reaction of [**2.1**oH⊃**24C8**]$^+$ followed a zero-order kinetic. In the case of [**2.1**oH⊃**DB24C8**]$^+$, the thermal cycloreversion reaction follows a zero-order profile at any concentration, although with a larger half-life with respect to the free axle. Similar results were obtained with [**2.3**oH⊃**24C8**]$^+$ and [**2.3**oH⊃**DB24C8**]$^+$, *i.e.*, the thermal cycloreversion reactions follow a zero order kinetics, with similar photoconversion extents and slightly lower rate constants with respect to the free thread. On the other hand, compound **2.2**H$^+$ underwent the greatest improvement of the photochemical properties on complexation: both [**2.2**oH⊃**24C8**]$^+$ and [**2.2**oH⊃**DB24C8**]$^+$ could be photoisomerized to the closed forms, with photoconversions up to 75%. The back thermal cycloreversion reactions are completed within 2 to 4 hours, respectively, and are compatible with a first order mechanism. In the case of [**2.2**cH⊃**DB24C8**]$^+$, better results were obtained in presence of an excess of **DB24C8** (>3 equivalents), *i.e.*, the fitting of the kinetic curve is better with respect to a 1:1 mixture of thread and macrocycle. This finding is not surprising on consideration of the shape of the titration curve, that indicates that the stability constant of this complex is lower with respect to the other pseudorotaxanes. It is possible that, at a lower concentration of crown ether, an interference from a minor percentage of free **2.2**oH$^+$ is observed.

2.5 Mechanism hypotheses

Regarding the unusually fast and zero-order kinetic profile of the thermal processes, two possible mechanisms have been hypothesized. According to the first one, schematized in figure 2.11, the closed form undergoes a tautomerization equilibrium besides the cycloreversion: the imidazolic proton of the closed form *a* could be abstracted from the nearby double bond, to give the tautomer *b*. The latter would eventually lead to the open form, driven by the restorage of the aromaticity. This tautomeric pathway is likely to be prevented in the pseudorotaxanes, since the proton that undergoes tautomerization is now involved in the hydrogen bonding with the crown ether.

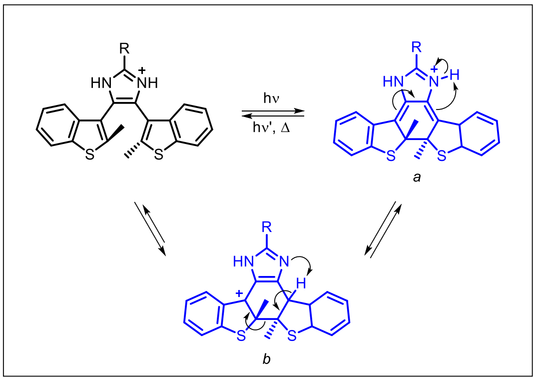

Figure 2.11: Schematic representation of the tautomeric equilibria of the closed form in the free axles.

This mechanism can partially explain why the lifetime of closed form of the pseudorotaxanes is elongated with respect to the free axles. However, it cannot explain the zero-order kinetics, since the tautomeric pathway should follow a first order mechanism, depending on the difference in the rate constants of the two equilibria. Moreover, this hypothesis does not explain why some of the pseudorotaxanes still show a zero-order kinetics. From an experimental viewpoint, besides the low half-life of the closed forms, no signals in the NMR nor in the UV-vis spectra can evidence the presence of the tautomer *b*, thus providing an experimental support to this hypothesis is a challenging task.

A second hypothesis is that the protons and/or the counterions can play a role in the thermal process. In order to probe the influence of these species on the kinetics of cycloreversion, the thermal isomerization reactions of the neutral compound **2.1** were repeated in presence of different ratios of acid, tetrabutylammonium triflate (TBATfO) or both (figure 2.12, table 2.5). Since the absorbance vs time plots resulted to be either first or zero-order like, the following discussion will be focused on the half-lives of the species. Nevertheless, it is worth recalling that in a zero-order kinetics, the rate constant is independent on the concentration, but the lifetime depends on the concentration. In other words, two processes with the same rate constant (*i.e.*, with the same slope of the straight line) but starting from different absorbances will be completed in different timescales. Thus, in the comparison between two different experiments, the analytical concentration of the sample and the amount of closed form produced must be taken into account.

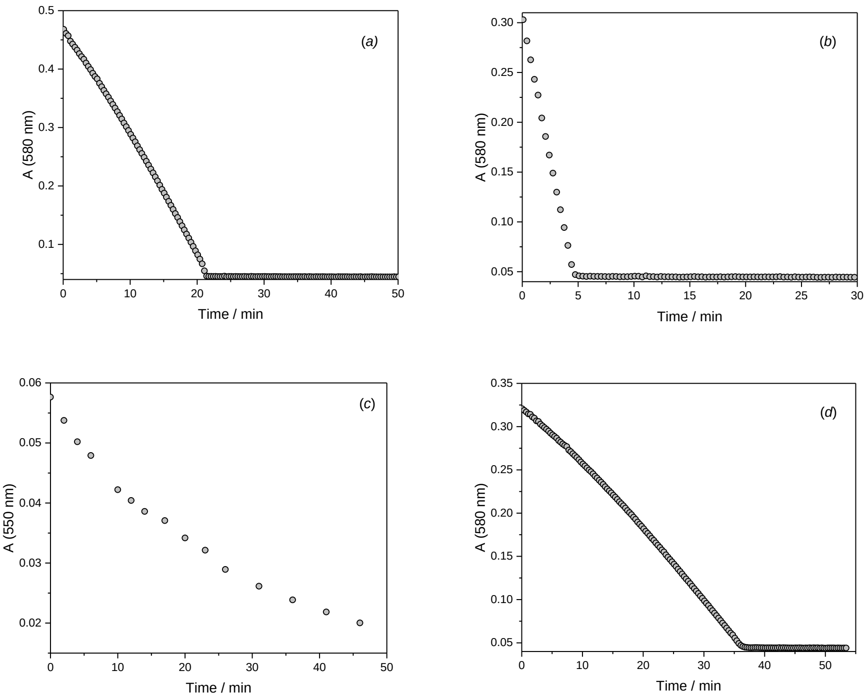

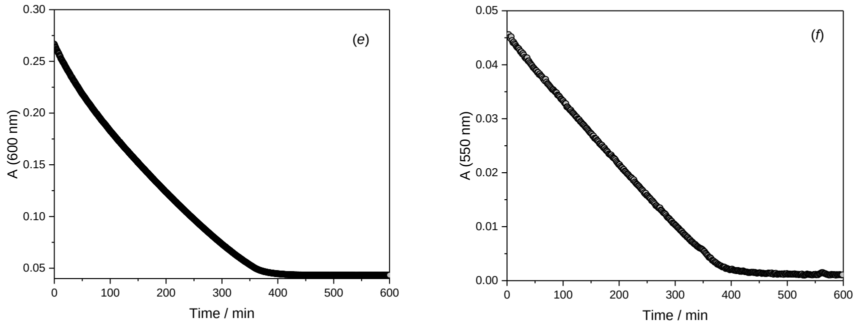

Figure 2.12: Thermal isomerization kinetics after irradiation at 313 nm of compound ***2.1*** *in presence of 1 eq. of TfOH (a), 10 eq. of TfOH (b), 1 eq. of TBATfO (c), 1 eq. of TfOH and 9 eq. of TBATfO (d), 1 eq. of* ***24C8*** *(e) and 5 eq. of TBA (f).*

Sample	*Concentration / M*	*$t_{1/2}$ / min*
2.1c + 1 eq. TfOH	8.2×10^{-5}	13
2.1c + 10 eq. TfOH	8.2×10^{-5}	2.7
2.1c + 1 eq. TBATfO	5.6×10^{-6}	28
2.1c + 1 eq. TfOH 9 eq. TBATfO	8.2×10^{-5}	23
2.1c + 1 eq. **24C8**	3.7×10^{-5}	180
2.1c + 5 eq. TBA	2.1×10^{-5}	190

Table 2.5: Half-lives ($t_{1/2}$) of compound ***2.1c*** *in presence of acid, base, crown ether or triflate ions.*

The kinetics of all the solutions containing triflic acid (figure 2.12a, b, d) follows a zero-order like kinetics, but the slope increases as the amount of acid increases. When only the triflate counterion is present (figure 2.12c), the kinetic profile is compatible with a first order, whereas in presence of 1 equivalent of acid and 9 equivalents of TfO^- (figure 2.12d), the order is still zero-like. In presence of 1 equivalent of crown ether **24C8** (figure e) or 5 equivalents of tributylamine (TBA) (figure 2.12f) the profile is neither a pure first order nor a zero-order, but the half-lives are largely elongated. All these results suggest that the counterion itself is not responsible for the zero-order kinetics. Instead, it is likely that the presence of acid leads both to a zero-order mechanism and to a shortening of the half-life on increasing its concentration. The presence of some free acid in the solvent could be responsible of this behaviour even when it is not added, but these impurities can be scavenged either by a base (TBA) or by the crown, which is not able to associate with the neutral axle, but can host free protons.

The fact that the thermal cycloreversion reactions of the [2]pseudorotaxanes depend on the absolute concentration and/or on the relative ratio of the molecular components supports the hypothesis of multiple processes in the complexation reaction, which could possibly involve the competition of the crown ethers with imidazolium (in the open form) and/or imidazolinium (in the closed form) for the proton. It is worth recalling that in the imidazolinium moiety, which is formed upon isomerization (figure 2.13), the positive charge is more confined than in the imidazolium, and, therefore, the protons should be more acidic and the hydrogen bonding more efficient.[39,40]

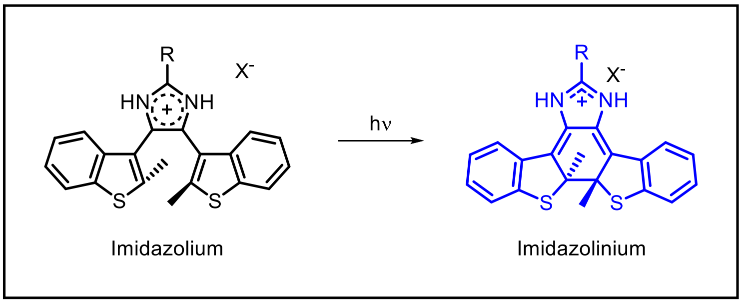

Figure 13: Structures of the imidazolium (left) and imidazolinium (right) ions.

On the other hand, other competing processes could arise, like, for instance, ion pairing, or, as mentioned above, more complex equilibria, wherein the proton is either shared in higher stoichiometries complexes or uptaken by the crown ethers. All these competing equilibria are concentration dependent, and could also be influenced by the nature of the counterions. On consideration of the erratic behaviour of these molecules, only reasonable hypotheses can be made. In the simplest scenario (figure 2.14), the closed and open isomers of the investigated compounds can undergo at least two equilibria each: the acid-base reaction, and the ion-pairing reaction with the counterions. Therefore, three species can be present simultaneously in solution for each isomer: protonated tight ion pair, protonated loose ion pair, and deprotonated. The closed form of each of these species can undergo thermal cycloreversion reactions with different kinetics. Moreover it cannot be excluded that the protonated compounds can resonate with other isomeric forms,[38] or undergo intramolecular proton-transfer reactions. The dependence of the outcomes of the titration and kinetic experiments on the concentration of crown ethers, acid and counterions suggests that indeed these multiple equilibria can play a role. An exhaustive elucidation of all these parallel processes is a challenging task, and is beyond the scope of this work. Nonetheless, a thorough investigation, aimed at unravelling the processes at the basis of these apparently erratic results, is underway in the research group.

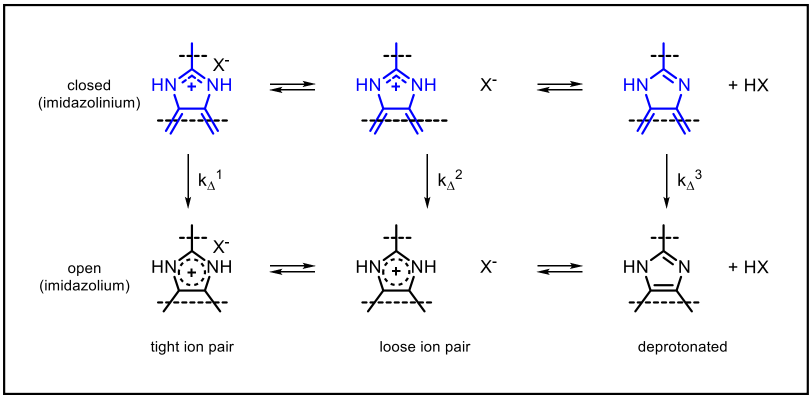

Figure 2.14: Schematic representation of the thermal cycloreversions (vertical processes) and the ion pairing equilibria (horizontal processes).

2.6 Conclusion and perspectives

The study on how the photochromism of a supramolecular system differs from that of the molecular components has been here reported. In this investigation, photochromic terarylenes, whose bridging unit is an imidazolium, able to give pseudorotaxanes with crown ethers, were characterized in their free form and in association with either **24C8** or **DB24C8** crown ethers. The closed form of the free axles, obtained upon UV-irradiation, is very short-lived and reverts to the open isomer within tens of seconds, following, in some cases, a zero-order profile. The nature of this unexpected kinetics is still under study, but it can preliminarily be ascribed to the presence of a tautomerization in the free axles, that is prevented by complexation with the crown, or to different and competitive equilibria involving the proton and the counterion between the open and the closed forms. All the axles gave stable pseudorotaxanes, with stability constants up to 10^6 M^{-1}. The photochromism of the pseudorotaxanes was found to be improved with respect to the isolated axles. The kinetics of thermal isomerization were affected the most, in terms of reaction order, lifetime elongation or both. In summary, this study showed that the photochromic properties of a molecule can be tuned and enhanced by means of supramolecular chemistry. This phenomenon, which can be termed threading-gated photochromism, extends the concept of gated photochromism[15] in the field of supramolecular chemistry. In future, the models herewith reported can be expanded and applied in more elaborated architectures, like for instance rotaxanes or polyrotaxanes, in order to exploit light as an orthogonal stimulus to trigger a mechanical response in the material or, *vice versa*, to change the photochromic properties of a building block by means of supramolecular interactions.

2.7 References

1. P. Ceroni, A. Credi, and M. Venturi, *Chem. Soc. Rev.*, **2014**, *43*, 4068–4083.
2. M. Baroncini, M. Canton, L. Casimiro, *et al.*, *Eur. J. Inorg. Chem.*, **2018**, *42*, 4589–4603.
3. M. Baroncini, S. Silvi, and A. Credi, *Chem. Rev.*, **2019**, DOI: 10.1021/acs.chemrev.9b00291.
4. H. S. Tang, N. Zhu, and V. W. W. Yam, *Organometallics*, **2007**, *2*, 22–25.
5. S. Wang, X. Li, W. Zhao, *et al.*, *J. Mater. Chem. C*, **2017**, *5*, 282–289.
6. V. Lemieux and N. R. Branda, *Org. Lett.*, **2005**, *7*, 2969–2972.
7. J. Kuhni and P. Belser, *Org. Lett.*, **2007**, *9*, 1915–1918.
8. M. S. Vollmer, T. D. Clark, C. Steinem, and M. R. Ghadiri, *Angew. Chem. Int. Ed.*, **1999**, *38*, 1598–1601.
9. M. Yamamura, Y. Okazaki, and T. Nabeshima, *Chem. Commun.*, **2012**, *48*, 5724–5726.
10. P. Bortolus and S. Monti, *J. Phys. Chem.*, **1987**, *91*, 5046–5050.

11. A. M. Sanchez and R. H. de Rossi, *J. Org. Chem.*, **1996**, *61*, 3446–3449.

12. M. Takeshita, N. Kato, S. Kawauchi, T. Imase, J. Watanabe, and M. Irie, *J. Org. Chem.*, **1998**, *63*, 25, 9306–9313.

13. E. Arunkumar, C. C. Forbes, and B. D. Smith, *Eur. J. Org. Chem.*, **2005**, *2005*, 19, 4051–4059.

14. M. Å. Petersen, B. Rasmussen, N. N. Andersen, *et al.*, *Chem. Eur. J.*, **2017**, *23*, 67, 17010–17016.

15. M. Lohse, K. Nowosinski, N. L. Traulsen, *et al.*, *Chem. Commun.*, **2015**, *51*, 48, 9777–9780.

16. G. Baggi, L. Casimiro, M. Baroncini, S. Silvi, A. Credi, and S. J. Loeb, *Chem. Sci.*, **2019**, *10*, 19, 5104–5113.

17. M. Irie, T. Fukaminato, K. Matsuda, and S. Kobatake, *Chem. Rev.*, **2014**, *114*, 12174–12277.

18. M. Irie, *Chem. Rev.*, **2000**, *100*, 5, 1685–1716.

19. H. Tian and S. Wang, *Chem. Commun.*, **2007**, *8*, 781–792.

20. N. Noujeim, K. Zhu, V. N. Vukotic, and S. J. Loeb, *Org. Lett.*, **2012**, *14*, 10, 2484–2487.

21. K. Zhu, V. N. Vukotic, and S. J. Loeb, *Angew. Chem. Int. Ed.*, **2012**, *51*, 9, 2168–2172.

22. K. Zhu, V. N. Vukotic, N. Noujeim, and S. J. Loeb, *Chem. Sci.*, **2012**, *3*, 11, 3265–3271.

23. N. Farahani, K. Zhu, N. Noujeim, and S. J. Loeb, *Org. Biomol. Chem.*, **2014**, *12*, 27, 4824–4827.

24. N. Farahani, K. Zhu, and S. J. Loeb, *Chem. Phys. Chem.*, **2016**, *17*, 12, 1875–1880.

25. K. Zhu, G. Baggi, V. N. Vukotic, and S. J. Loeb, *Chem. Sci.*, **2017**, *8*, 5, 3898–3904.

26. K. Zhu, G. Baggi, and S. J. Loeb, *Nat. Chem.*, **2018**, *10*, 6, 625–630.

27. V. N. Vukotic, K. J. Harris, K. Zhu, R. W. Schurko, and S. J. Loeb,

Nat. Chem., **2012**, *4*, 456–460.

28. K. Zhu, V. N. Vukotic, C. A. O'Keefe, R. W. Schurko, and S. J. Loeb, *J. Am. Chem. Soc.*, **2014**, *136*, 20, 7403–7409.

29. K. Zhu, C. A. O'Keefe, V. N. Vukotic, R. W. Schurko, and S. J. Loeb, *Nat. Chem.*, **2015**, *7*, 514–519.

30. G. Gholami, K. Zhu, J. S. Ward, P. E. Kruger, and S. J. Loeb, *Eur. J. Inorg. Chem.*, **2016**, *2016*, 27, 4524–4529.

31. H. B. Cheng, H. Y. Zhang, and Y. J. Liu, *J. Am. Chem. Soc.*, **2013**, *135*, 10190–10193.

32. H. Zhang, X.-X. Kou, Q. Zhang, D.-H. Qu, and H. Tian, *Org. Biomol. Chem.*, **2014**, *9*, 4051–1056.

33. Z. Li, X. Han, H. Chen, *et al.*, *Org. Biomol. Chem.*, **2015**, *13*, 7313–7322.

34. T. Nakashima, Y. Kajiki, S. Fukumoto, *et al.*, *J. Am. Chem. Soc.*, **2012**, *134*, 19877–19883.

35. J. P. Calupitan, T. Nakashima, Y. Hashimoto, and T. Kawai, *Chem. Eur. J.*, **2016**, *22*, 10002–10008.

36. T. Kawai, T. Nakashima, K. Atsumi, *et al.*, *Chem. Mater.*, **2007**, *19*, 3479–3483.

37. C. Coudret, T. Nakagawa, T. Kawai, and J.-C. Micheau, *New J. Chem.*, **2009**, *33*, 1386–1392.

38. R. Kanazawa, T. Nakashima, and T. Kawai, *J. Phys. Chem. A*, **2017**, *121*, 1638–1646.

39. P. Gilli, L. Pretto, V. Bertolasi, and G. Gilli, *Acc. Chem. Res.*, **2009**, *42*, 33–44.

40. T. Nakashima, M. Goto, S. Kawai, and T. Kawai, *J. Am. Chem. Soc.*, **2008**, *130*, 14570–14575.

Chapter 3.

Molecular locking of photochromism in azobenzene-derivatized fullerenes

3.1 Introduction and aim

From their discovery between late 1980s and 1990s,[1,2] carbon allotropes, such as fullerenes and nanotubes, have been extensively studied due to their interesting electronic properties and, moreover, to their easiness of functionalization. In the last decades, their chemistry and reactivity have been deeply elucidated. The peculiar truncated icosahedral structure of fullerene **C_{60}** arises from a different bond length between the six- and five-membered aromatic rings, which eventually leads to a non-planar structure. Specifically, *5,6* bonds, *i.e.*, bonds shared between five- and six-membered rings, are 1.45 Å long, whereas the *6,6* bonds, *i.e.*, those shared between two benzenic rings, are 1.38 Å long. This difference is related to a more pronounced double-bond character of the *6,6* bonds, and for this reason, it shows a higher reactivity. Many studies on fullerene have been devoted to its functionalization, producing a large variety of reactions, from nucleophilic addition/substitution, to electrophilic addition, to cycloadditions. Among these reactions, the two most known are the Prato reaction and the Bingel reaction (figure 3.1). The Prato reaction[3] is a *1,3*-dipolar cycloaddition where the *6,6* bond of the fullerene reacts with an azomethine ylide to yield a pyrrolidinofullerene, as reported in figure 3.1. On the other hand, the Bingel reaction[4] is a cyclopropanation reaction of the *6,6* bond to give a methanofullerene, upon reaction between **C_{60}** and a bromomalonate in presence of a base strong enough to give the corresponding enolate (figure 3.1). Instead of using malonates, the same reaction can be conducted using disubstituted carbenes, as they carry a lone pair comparable to the enolic one and able to give the same nucleophilic addition on the **C_{60}**.

Prato reaction

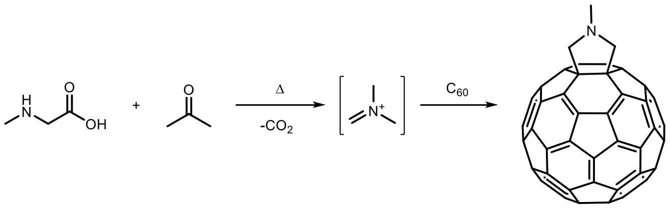

Bingel reaction

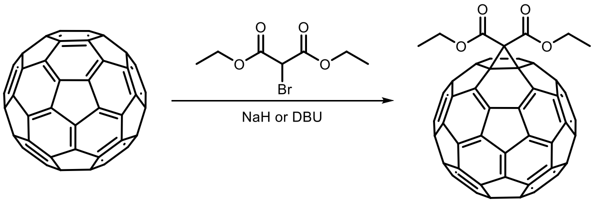

Figure 3.1: Reaction schemes for Prato (top) and Bingel (bottom) reactions as reported in 1993.[3,4]

Fullerene can be further functionalized,[5,6] although after the first functionalization, the remainder bonds are not equivalent anymore. In this regard, 9 different regioisomers can be produced depending on the position of the second substituent with respect to the first one.[7] Precisely, if the first functionality is placed on one pole of the sphere, the bisadduct is named *cis* if the second functionality is in the same hemisphere, *equatorial* if it is on the equator, or finally *trans* if it is on the opposite hemisphere or on the opposite pole. A total of 9 regioisomers can be obtained, as schematically represented in figure 3.2.

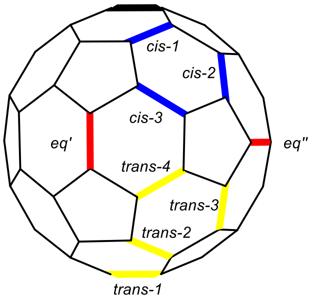

Figure 3.2: Cis (blue bonds), equatorial (red bonds) and trans (yellow bonds) regioisomers, with respect to the black bond, of a **C_{60}** *bisadduct (double bonds have been omitted for clarity).*

The mixture of regioisomers is usually composed of a larger amount of *equatorial* or *trans* isomers, especially *eq''* and *trans-3*. This is due mainly to statistical reasons (one possibility for a *trans-1* attack, two for the *equatorial* positions, and four possibilities for each of the other *trans* and *cis*) and to the fact that *cis-* isomers are usually disfavoured for steric reasons.[7] However, the composition of each isomer in the mixture can be tuned by changing the reaction conditions, for example, by linking the two tethers to a stiff scaffold as in the tether-directed remote functionalization reported by Diederich et al. in 1994.[8] For the sake of simplicity, the adducts formed by the covalent linking between the fullerene and the two tethers of the same molecule will be called "bisadducts" as well.

An interesting example of a supramolecular tuning of the regioselectivity has been provided by Prato and coworkers.[9] In this work, a molecular axis of a rotaxane is endowed with a terminal fulleropyrrolidine and an amide as stoppers, whereas the ring is a benzylic amide macrocycle. This macrocycle can shuttle between two distant sites, giving rise to two translational isomers, according to the solvent polarity. In non-polar solvents, such as $CHCl_3$, the ring shuttles towards the amidic end, in order to maximize the hydrogen bonding. Conversely, in polar solvents like DMSO or DMF, with a higher competition on the hydrogen bonds, the macrocycle prefers to encircle the fullerenic unit. As a result, when a benzylamine is added as a reactant for a second functionalization on the fullerene stopper, the regioselectivity is dictated by the proximity of the macrocycle. Indeed, in non-polar solvents, the ratio between the regioisomers is similar to that obtained with non-tethered compounds. Conversely, in DMF, the macrocycle is on the fullerene and allosterically influences the regioselectivity, leading to a mixture of regioisomers richer in *cis* and poorer in *trans* isomers.

The aim of the work here reported is to investigate if and how the regioselectivity of a cyclopropanation reaction can be affected by the different geometries of a switchable scaffold holding two tethers and *vice versa*. For this purpose, an azobenzene unit, able to photoswitch between the *E* and the *Z* isomer, was functionalized with two ethylmalonate tethers either in *p,p'* positions (**3.1**), or in *m,m'* positions (**3.2**), as reported in figure 3.3.

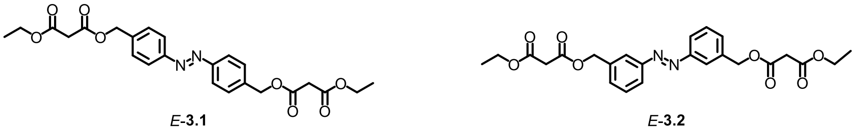

E-**3.1**

E-**3.2**

Figure 3.3: Structures of the two precursors for the synthesis of azobenzene-C_{60} bisadducts.

In addition, this work aims to investigate if and how the photochemical behaviour of the azo- moiety covalently bound to the fullerene differs from that of the precursor.

3.2 Bis-ethylmalonate derivatives of azobenzene

The photochemical and photophysical characterization of the precursors was conducted in distilled toluene (PhMe), as it is the solvent of choice for the cyclopropanation reactions.

Compound **3.1** shows the typical absorption spectrum of azobenzene derivatives (figure 3.4, table 3.1): a low absorbing n-π* band centred at 450 nm, with a molar absorption coefficient (ε) of 660 M^{-1} cm^{-1} and a more intense π-π* band in the UV region, centred at 328 nm and with an ε of 27000 M^{-1} cm^{-1}. The two bands are well resolved, confirming that the two groups in *para* position do not affect the electronic structure of the photochromic unit.

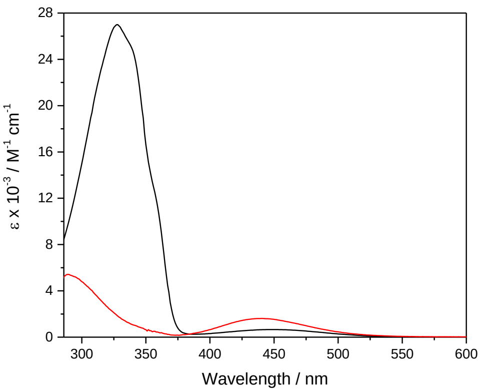

*Figure 3.4: Absorption spectrum of E-**3.1** (black) and Z-**3.1** (red) in PhMe.*

Irradiation of **3.1** at 313 nm or 365 nm produces a strong decrease in the UV absorption band and an increase of the n-π^* band (see figure 3.5), that is ascribable to an *E-Z* isomerization, until a photostationary state (*PSS*) is achieved. The composition of the *PSS* was determined according to the Fischer method[10] and resulted to be 97:3 *Z:E* at 365 nm and 68:32 *Z:E* at 313 nm. With the same method it was possible to obtain mathematically the absorption spectrum of the *Z* isomer (figure 3.4). The quantum yields for the isomerization, measured upon irradiation at 365 nm were found to be $\Phi_{EZ} = 0.14$ and $\Phi_{ZE} = 0.24$.

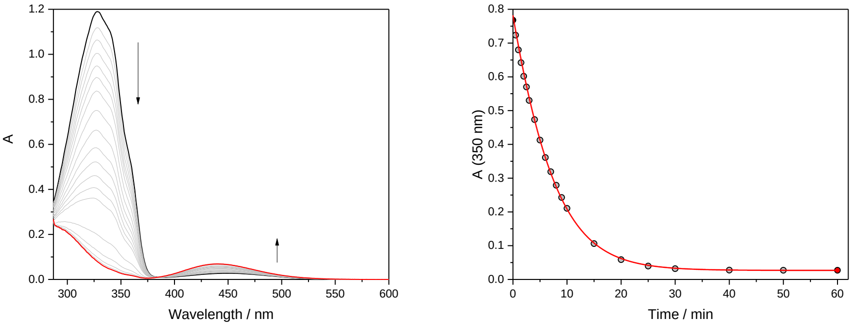

*Figure 3.5: Left: absorption spectra of **3.1** upon irradiation at 365 nm; right: absorbance variations at 350 nm and fitting (red line) according to equation (E8).*

Upon irradiation at 436 nm of a solution previously exhaustively irradiated at 365 nm to reach the *PSS*, back *Z-E* photoisomerization occurs, until a *PSS* of 86:14 *E:Z* is afforded.

The thermal isomerization was measured by observing over several days the absorption changes of a UV-irradiated solution kept in the dark at room temperature. The data could be satisfactorily fitted according to a first order kinetic law, giving a rate constant of 2.7×10^{-6} s^{-1}. Since the reaction with fullerene has to be conducted at 0°C for 2 hours, the thermal process was monitored at this temperature, and the amount of *E*-isomer recovered by means of this process was found to be negligible in 1 hour.

Compound **3.2** showed an absorption spectrum similar to compound **3.1** (figure 3.6, table 3.1), but with an overall lower absorption.

The n-π* band is centred at 450 nm, with a molar absorption coefficient ε of 500 M^{-1} cm^{-1} whereas the π-π* band is blueshifted of 6 nm with respect to **31**, centred at 322 nm and with an ε of 22000 M^{-1} cm^{-1}.

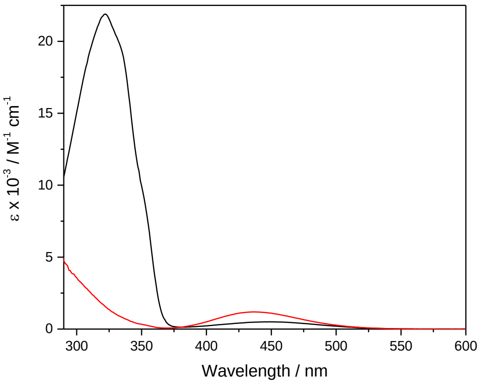

*Figure 3.6: Absorption spectrum of E-**3.2** (black) and Z-**3.2** (red) in PhMe.*

Irradiation of **3.2** in the UV induces a *E*-*Z* isomerization (figure 3.7), but resulting in photostationary states less rich in *Z*-isomer with respect to **3.1**. As in the previous case, the *PSS* obtained upon irradiation at 365 nm and 313 nm were employed to extrapolate the spectrum of the pure *Z* isomer according to the Fischer method.[10] The percentage of *Z* at the *PSS* resulted to be 92% upon irradiation at 365 nm and 83% upon irradiation at 313 nm. The quantum yields for the *E*-*Z* photoisomerization at 365 nm were found to be $\Phi_{EZ} = 0.18$ and $\Phi_{ZE} = 0.26$.

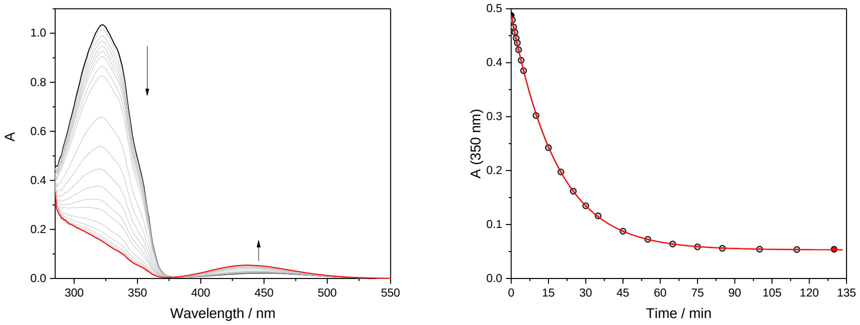

*Figure 3.7: Left: absorption spectra of **3.2** upon irradiation at 365 nm; right: absorbance variations at 350 nm and fitting according to equation (E8).*

Irradiation in the visible region converts preferentially the *Z*-form into the *E*, leading to a photostationary state composed of 15% of *Z* isomer. The thermal back isomerization, in this case, possesses a rate constant of 1.4×10^{-6} s^{-1}. For this compound, the thermal process is slower than for compound **3.1**, and even in this case, it was proven to be negligible in the reaction conditions (0°C, 2 hours). However, the *PSS* reached by irradiation with UV light resulted to have a larger amount of *E* isomer, and this represents a drawback for the synthesis of the corresponding bisadduct.

3.3 Photochromism of azobenzene-C_{60} bisadducts

The synthesis of molecular bisadducts between **C_{60}** and **3.1** or **3.2** was conducted in collaboration with Dr. Luka Dordevic (University of Trieste), according to the procedure reported by Diederich et al. in 2005.[11] A concentrated solution of the corresponding azobenzene precursor was reacted with **C_{60}** at 0°C in PhMe for 2 hours, in presence of I_2 and DBU. For reactions between **C_{60}** and the *Z* isomer of the azobenzene precursor, the solution of the latter was previously exhaustively irradiated up to the photostationary state. After deprotonation of the acidic protons, the malonate groups react with the double bond of **C_{60}**, giving cyclopropanation Bingel reaction.[4,7] As mentioned above, the thermal back isomerization is negligible in the reaction timescale, therefore the amount of *E* isomer of the reactant is approximately given by the *PSS* composition.

Reaction between *Z*-**3.1** and **C_{60}** produces the equatorial bisadduct *Z*-**3.3** (yield 30%) and a small percentage of **3.3b**, that was isolated from the reaction mixture but not in a sufficient amount to allow a full characterization (figure 3.8). The same reaction performed with *E*-**3.1** gave a mixture of different regioisomers. On the other hand, both the reactions of *E*-**3.2** and *Z*-**3.2** with **C_{60}** gave the same *equatorial* bisadduct *E*-**3.4** (figure 3.8), although in different yields (32% for *E*-**3.2** and 28% for *Z*-**32**). The isomer of each of the products was determined via ^{1}H-NMR, ^{13}C-NMR and XRD analyses (figure 3.8). A possible explanation of this results could be that the *equatorial* regioisomer is favoured in any of the cases, and therefore the configuration of the azo moiety is dictated by the attack on the fullerene. In the first case, the linear structure of *E*-**3.1** prevents the regioselectivity of the reaction, whereas Z-**3.1** possesses the right geometrical and sterical features to allow the attack in *equatorial* position in a good yield and with a good selectivity. Conversely, in the second case, only the *E* isomer possesses the right features for the anchoring, thus when *Z*-**3.2** reacts with fullerene, its configuration is changed accordingly.

By trans-esterification of *Z*-**3.3** or *E*-**3.4** with EtOH in presence of K_2CO_3 the equatorial bis-diethylmalonate **C_{60}** (**3.5**) is eventually obtained, as already reported in literature (figure 3.8).[12]

As reported by Hirsch et al., the different regioisomers of a **C_{60}** bisadduct possess a peculiar absorption spectrum.[7] Thus, absorption spectroscopy was used as a tool to further confirm the nature of the regioisomers obtained from the reaction. As for the precursors, the photochemical and photophysical characterization of the bisadducts was conducted in distilled PhMe.

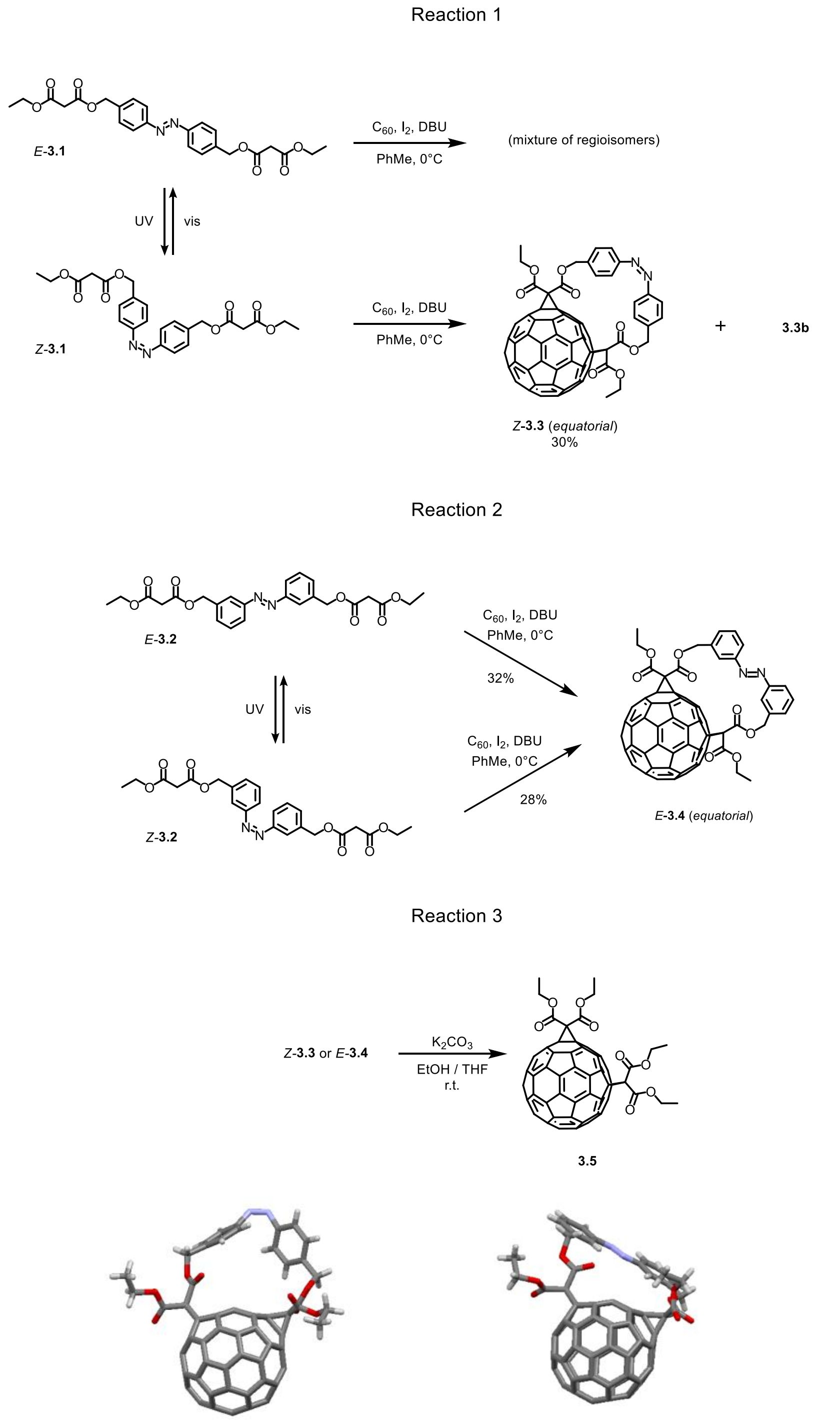

*Figure 3.8. Top: reaction scheme for the synthesis of bisadducts Z-**3.3** and E-**3.4** and for the bisesther **3.5**; bottom: crystal structure of Z-**3.3** (left) and E-**3.4** (right, courtesy of Dr. N. Demitri, University of Trieste).*

Bisadduct *Z*-**3.3** showed an absorption spectrum (figure 3.9, table 3.1) coherent with a **C$_{60}$** bis-functionalized in *equatorial* position. Moreover, the spectrum is consistent with the mathematical sum of the absorption spectra of the parent *Z*-**3.1** and the bisesther compound **3.5** (taking into account that the malonate residuals are counted twice). This result confirms that in *Z*-**3.3** the azobenzene moiety is in *Z* configuration.

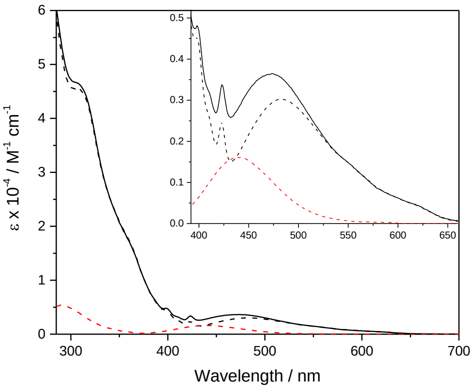

*Figure 3.9: Left: absorption spectrum of Z-**3.3** (black straight line) in PhMe, compared with those of Z-**3.1** (red dashed line) and **3.5** (black dashed line).*

To understand whether the azobenzene moiety is photoreactive when covalently linked to the fullerene, compound *Z*-**3.3** was irradiated in the visible region at 436 nm. The absorption spectrum displays little changes, namely an increase of the absorbance in the UV region, and a decrease in the visible. An isosbestic point is displayed at 385 nm, at the same wavelength of the isosbestic point between *E*- ad *Z*-**3.1**. Such a behaviour could be ascribed to a *Z*-*E* isomerization, with an estimated quantum yield of 0.11.

The photochemical and thermal reversibility of this process was proven as follows: a solution of the sample was consecutively irradiated at 436 nm, 365 nm, 436 nm and finally left in the dark (figure 3.10, left). The initial state is restored both after irradiation at 365 nm and after several minutes in the dark, confirming that the photoisomerization is reversible. Upon fitting of the absorbance changes over time in the dark, according to a first-order model, a kinetic constant of 1.0×10^{-3} s^{-1} was found (figure 3.10, right).

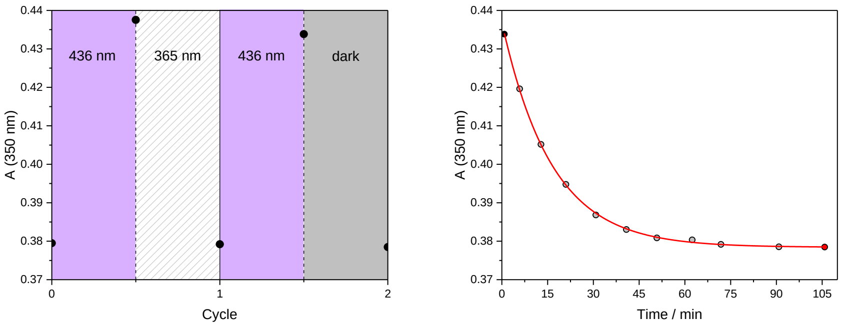

Figure 3.10: Left: absorbance variations upon alternated irradiations at 436 nm and 365 nm, and in the dark; right: absorbance variations in the dark of a solution irradiated at 436 nm with fitting (red line).

In order to assess whether energy transfer occurs from the lowest state of $\mathbf{C_{60}}$ to the n-π^* state of the photochromic moiety, a solution of *Z*-**3.3** and a mixture of *Z*-**3.1** and **3.5** were irradiated at 375 nm (figure 3.11), where the absorption coefficient of *Z*-**3.1** is lower than 200 M^{-1} cm^{-1}, whereas the absorption of *Z*-**3.3** is mainly due to the $\mathbf{C_{60}}$. The two samples show no appreciable variations, even after prolonged irradiation times (except for the thermal isomerization of *Z*-**3.1** in the mixture), proving that the energy absorbed by the fullerene is not transferred to the n-π^* state of azobenzene.

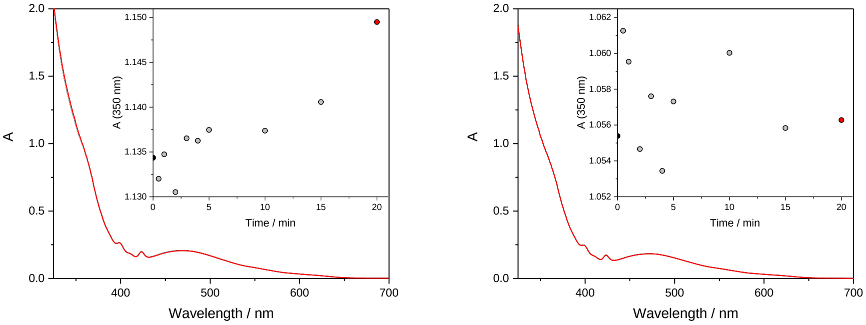

*Figure 3.11: Absorption spectra and absorbance variations at 350 nm (inset) upon irradiation at 375 nm of a mixture of Z-**3.1** and **3.5** (left) and of a sample of Z-**3.3**.*

Interestingly, the data here reported suggest that the anchorage of the photochromic moiety on a scaffold causes a strong stabilization of the metastable *Z* form of the precursor that ultimately becomes the most stable configuration in the bisadduct *Z*-**3.3**. Moreover, the *E*-form reverts back to the *Z*-configuration with a rate constant that is three orders of magnitude faster than in the precursor. It can be argued that, once the photochromic unit is attached to the fullerene, its configuration is retained because of the strain exerted by the covalent linking. Nevertheless, the cavity of the macrocycle formed by the azobenzene and the **C_{60}**, seems to be large enough to allow a *Z-E* photoisomerization. As it happens in cyclic azo-derivatives,[13] most likely the photoisomerization follows a rotation mechanism instead of an inversion, as it requires less free volume and the outer bonds are practically unchanged in length during the process.

The co-product **3.3b**, obtained from the reaction between **3.1** and **C_{60}**, does not shows an absorption spectrum compatible with an *equatorial* bisadduct (figure 3.12). The peaks at 418, 630 and 690 nm would suggest, instead, that the fullerene is derivatized in *trans-4* position.[7] Moreover, since the corresponding fullerene is not available as a model, in order to assess whether the azobenzene is attached in *E*- or *Z*-configuration, compound **3.3b** was irradiated at 365 nm. Under these conditions, the absorption spectrum shows a decrease of the absorbance in the UV region and an increase in the visible region, in line with a *E-Z* photoisomerization. The process is reversible if the solution is left in the dark. Nevertheless, the amount of solid obtained from the reaction mixture (below 0.5 mg) was not enough to allow a full photochemical characterization.

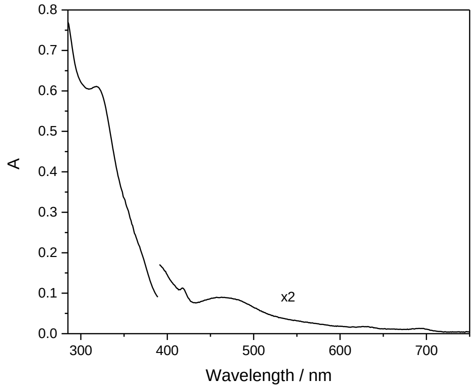

*Figure 3.12: Absorption spectrum of **3.3b**.*

Adduct *E*-**3.4** showed an absorption spectrum (figure 3.13, table 3.1) coherent with a **C60** di-functionalized in equatorial position and superimposable with the mathematic sum of the absorption spectra of the parent *E*-**3.2** and the bisesther compound **3.5**, confirming that the reaction occurred between the *E*- isomer and the **C60**.

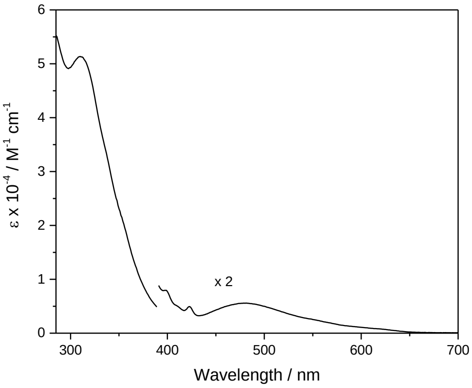

*Figure 3.13: Absorption spectrum of E-**3.4** in PhMe.*

Irradiation of *E*-**3.4** at 365 nm (figure 3.14) produces no appreciable variations, even at prolonged irradiation times. A flash-photolysis experiment, where the third harmonic of a Nd:YAG (355 nm) was used as photoisomerization trigger, showed no appreciable variations in the timescale of 200 ns. In addition, prolonged laser irradiation lead to a partial photodegradation of the sample.

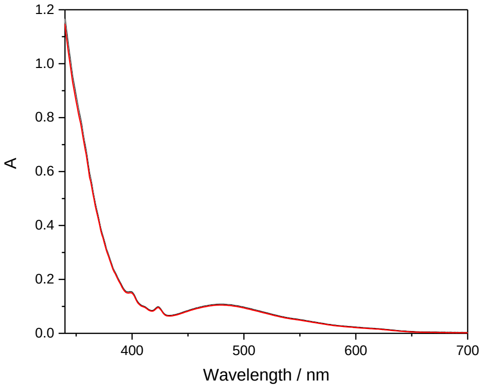

*Figure 3.14: Initial (black line) and final spectrum (red line) after prolonged irradiation (20 minutes) of **3.4** at 365 nm. The two spectra are overlapped.*

The absence of an appreciable *E*-*Z* photoisomerization could be due either to the suppressed photoreactivity of the azo-unit (*i.e.,* very low quantum yield) or to a very fast (below hundreds of nanoseconds) *Z*-*E* back reaction. Both cases can be presumed to be a consequence of the connection of the azobenzene to the fullerene via the malonate tethers, which may constrain the former in the *E* configuration and to the consequent absence of a sufficient free volume for the isomerization. It cannot be excluded, however, that the behaviour of this particular compound is determined by electronic interactions between the two molecular units.

Species	*ε / M^{-1} cm^{-1} (λ_{max} / nm)*	*$\Phi_{E\text{-}Z}$ (365 nm)*	*$\Phi_{Z\text{-}E}$ (365 nm)*	*Z:E at 365 nm*	*$\Phi_{E\text{-}Z}$ (436 nm)*	*$\Phi_{Z\text{-}E}$ (436 nm)*	*Z:E at 436 nm*	*k_{Δ} / s^{-1}*
E-**3.1**	27000 (328) 660 (450)	0.14	0.24	97:3	0.27	0.51	14:86	2.7×10^{-6} *(Z-E)*
Z-**3.3**	47000 (305) 3400 (423) 3600 (473)	*N.A.*	*N.A.*	*N.A.*	0.11	*N.A.*	*N.A.*	1.0×10^{-3} *(E-Z)*
E-**3.2**	22000 (322) 500 (450)	0.18	0.26	92:8	0.44	0.64	15:85	1.4×10^{-6} *(Z-E)*
E-**3.4**	51000 (310) 2500 (423) 2800 (479)	*N.A.*	*N.A.*	*N.A.*	*N.A.*	*N.A.*	*N.A.*	*N.A.*

Table 3.1: Photophysical and photochemical parameters in PhMe of the precursors and the bisadducts.

3.4 Conclusion

The work here reported was devoted to the study of two functionalized azobenzenes able to react with fullerene to give ciclopropanated bisadducts whose regioselectivity dictates the *E* or *Z* configuration of the azo- moiety. The two precursors showed a similar photochemical behaviour, although a slightly minor *E*-*Z* photoconversion upon UV irradiation (365 nm) is observed for compound **3.3**. Both of them revert back thermally to the *E* form with rate constants in the order of 10^{-6} s^{-1} at room temperature. In the reaction conditions, *i.e.*, at 0°C, below 2 hours, the thermal process can be neglected, thus it can be assumed that it does not increment the amount of *E* isomer already present in the *PSS* conditions. Reaction of the *p*-derivative *Z*-**3.1** with **C_{60}** yields the *equatorial* bisadduct *Z*-**3.3** and a small fraction of compound **3.3b**. In compound **3.3** the azo-bond retains the *Z* configuration from the reactant, and, moreover, this form is the most thermodynamically favoured isomer. The photochromic unit switches to the *E* isomer when irradiated with visible light (436 nm), and reverts to the *Z* in several minutes, in dark conditions. In compound **3.4**, the azobenzene is anchored to the fullerene in *equatorial* position, and therefore the photochromic moiety is locked in the *E* configuration, regardless of the reactant isomer, and shows no photoisomerization. In conclusion, since both reactions yield almost exclusively the equatorial adduct, it can be stated that the azobenzene configuration changes accordingly, thus compounds **3.3** and **3.4** can be considered as two examples of how the photochromism can be locked by means of covalent chemistry.

3.5 References

1. H. W. Kroto, J. R. Heath, S. C. O'Brien, R. F. Curl, and R. E. Smalley, *Nature*, **1985**, *318*, 162–163.
2. S. Iijima, *Nature*, **1991**, *354*, 6348, 56–58.
3. M. Maggini, G. Scorrano, and M. Prato, *J. Am. Chem. Soc.*, **1993**, *115*, 21, 9798–9799.
4. C. Bingel, *Chem. Ber.*, **1993**, *126*, 8, 1957–1959.
5. F. Diederich and R. Kessinger, *Acc. Chem. Res.*, **1999**, *32*, 6, 537–545.
6. C. Thilgen, S. Sergeyev, and F. Diederich, *Top. Curr. Chem.*, **2004**, 1–61.
7. G. Schick, A. Hirsch, H. Mauser, and T. Clark, *Chem. Eur. J.*, **1996**, *2*, 8, 935–943.
8. L. Isaacs, R. F. Haldimann, and F. Diederich, *Angew. Chem. Int. Ed. Eng.*, **1994**, *33*, 22, 2339–2342.
9. M. Carini, T. Da Ros, M. Prato, and A. Mateo-Alonso, *Chem. Phys. Chem.*, **2016**, *17*, 12, 1823–1828.
10. E. Fischer, *J. Phys. Chem.*, **1967**, *71*, 11, 3704–3706.
11. S. Sergeyev, M. Schär, P. Seiler, O. Lukoyanova, L. Echegoyen, and F. Diederich, *Chem. Eur. J.*, **2005**, *11*, 8, 2284–2294.
12. A. Hirsch, I. Lamparth, and H. R. Karfunkel, *Angew. Chem. Int. Ed. Eng.*, **1994**, *33*, 4, 437–438.
13. H. M. D. Bandara and S. C. Burdette, *Chem. Soc. Rev.*, **2012**, *41*, 5, 1809–1825.

Chapter 4.

Single- and multi-component photochromic and luminescent DCM derivatives

4.1 Introduction and aim

The continuous growth in the field of photoactive molecules, gradually coupled in the last decades with the advances of functional nanoscaled materials, has led to a wide range of applications, particularly in the field of optoelectronics, molecular nanoprobes, photo-responsive multifunctional devices, or super-resolution imaging.[1–5] For these purposes, a proper design and synthesis of new fluorescent molecular components, aimed to fulfil specific optical or chemical requests, is of pivotal importance. In such a context, the 4-dicyanomethylene-2-methyl-6-(p-dimethylaminostyryl)-4H-pyran (**DCM**, figure 4.1) provides an excellent prototype. **DCM** is a well-known fluorophore, displaying strong red emission.[6] Moreover, its charge transfer character from the electron-donating amine to the electron-withdrawing cyano-pyranyl moiety, confers to this dye a strong solvatochromism,[7–11] and, therefore, the possibility to tune the absorption and the emission by means of solvent polarity. For all these reasons, **DCM** has found many applications as chemo- or biosensors,[2,12–16] as dopants or hosts for OLEDs,[17–20] in non-linear optics materials,[21,22] or in supramolecular photoactive architectures[23–25] and logic gates.[26–29] Interestingly, due to the presence of an ethylenic central bond, **DCM** can in principle undergo *E*/*Z* photoisomerization, *i.e.*, behave as a photochrome. This photoswitching ability would be extremely appealing, since it would disclose new routes of fine tuning the optical properties of the fluorophore. However, only a limited number of qualitative studies have been reported on this phenomenon.[9,30,31] Furthermore, for each of the two configurational isomers, *i.e.*, *E* and *Z*, the molecule can in principle exist in two conformers, obtained by rotation around the single bond in position *6* on the pyranyl moiety. Thus, depending on the reciprocal position of the two double bonds, four isomers, namely *s-trans-E*, *s-cis-E*, *s-trans-Z*, *s-cis-Z*, can be defined (figure 4.1). It can be assumed that each of them possesses peculiar features and contributes in a different way to the overall properties. However, the aspects related to the conformational isomerism have never been deeply elucidated in studies reported so far.

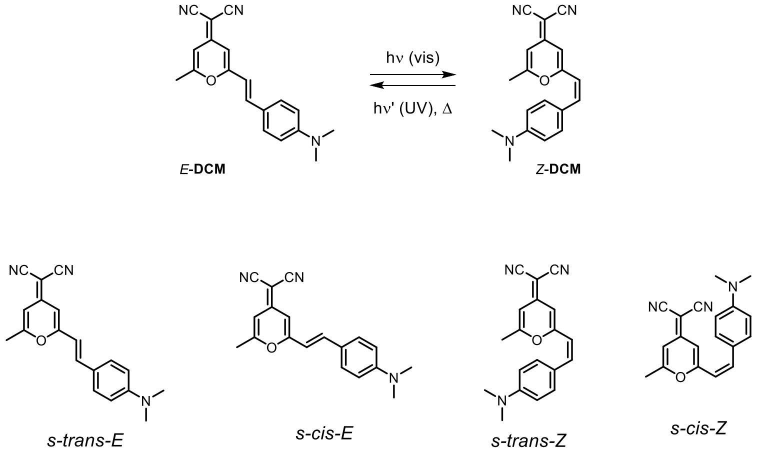

Figure 4.1: Photoisomerization reaction (top) and conformers (bottom) of ***DCM****.*

The work herewith reported aims to study new **DCM** derivatives (figure 4.2), in order to extend the knowledge about the photoisomerization process and to investigate the relationship between the photochromic and the fluorophoric behaviour, with a particular emphasis on the solvent effect. For this purpose, three derivatives of **DCM** were characterized. The pyranyl unit has been endowed either with a *t*-butyl group or fused to a benzenic ring, in order to improve the solubility in organic solvents, whereas the anilinic nitrogen atom has been functionalized with a propargyl or a diphenyl unit. Moreover, a multicomponent structure, namely a mannose scaffold bearing three **DCM** units linked by means of click chemistry, was also studied, in order to elucidate if and how the photochromic/fluorophoric groups are photophysically and photochemically independent.

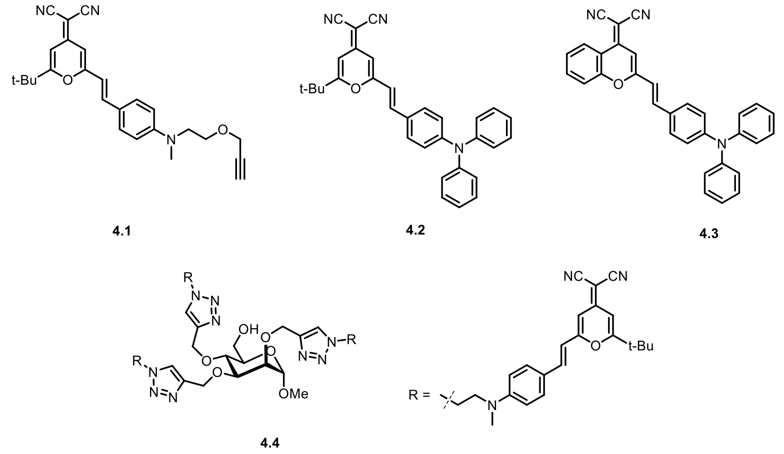
4.1 4.2 4.3

4.4

*Figure 4.2: Molecular structures of the studied **DCM** derivatives.*

4.2 Single component DCM derivatives

Compound **4.1** was synthesized in the group of Dr. R. Métivier and Prof. J. Xie (ENS - École Normale Supérieure Paris-Saclay), according to previously reported procedures.[25] The NMR spectra confirmed that, in the dark, compound **4.1** exists exclusively in the *E* configuration. Moreover, XRD measurements obtained on a single crystal clearly show that in the solid state the molecule assumes the *s-trans-E* configuration. In order to investigate the solvent effect on the photochemical properties of **4.1**, an exhaustive spectroscopic characterization was carried out in acetonitrile, tetrahydrofuran (THF) and toluene (PhMe). The absorption spectra gathered in figure 4.3 show the typical features of **DCM** derivatives:[6,7,11,24,25] an intense absorption band centred in the visible region and a weaker and more structured band located in the medium UV range. As the polarity decreases, the main band is only slightly shifted, with maxima at 465 nm, 467 nm and 463 nm in CH_3CN, THF and PhMe, respectively, and the vibrational structure becomes gradually more pronounced. The molar absorption coefficient ε resulted to be rather non-sensitive to the solvent, with values comprised between 54 000 M^{-1} cm^{-1} in CH_3CN and 47 800 M^{-1} cm^{-1} in PhMe (figure 4.3, table 4.1). As previously reported for **DCM**-based compounds,[6,32] even **4.1** was found to be a good emitter in the visible region, exhibiting, in addition, a marked fluorescence solvatochromism:[6,7,11,13,20,24,25] the emission band is strongly blueshifted as the polarity decreases, and the maximum wavelength moves from 620 nm in CH_3CN to 550 nm in PhMe, spanning a range of 70 nm and consequently resulting in a shortening of the Stokes shift (table 4.1).

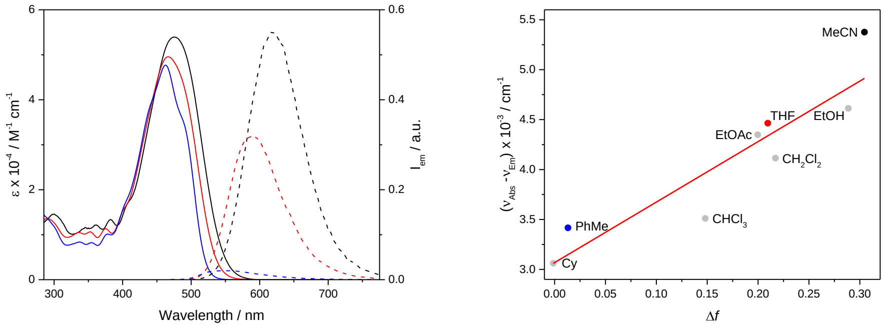

*Figure 4.3: Left: absorption (full line) and emission (dashed line) spectra of E-**4.1** in CH_3CN (black), THF (red) and PhMe (blue); right: Lippert-Mataga plot.*

Solvent	***Absorption***		***Emission***		
	λ_{abs} / nm	***ε / $M^{-1}cm^{-1}$***	***λ_{em} / nm***	***Stokes shift / 10^3 cm^{-1}***	***Φ_{em}***
CH_3CN	465	54 000	620	5.38	0.55
THF	467	50 000	590	4.46	0.28
PhMe	463	47 800	550	3.42	0.02

*Table 4.1: Photophysical parameters of E-**4.1** determined in CH_3CN, THF and PhMe.*

A comprehensive spectroscopic investigation as a function of the solvent was conducted, including a wide range of polarity levels. The resulting Lippert-Mataga plot[9] (figure 4.3) provides an enhancement of the dipolar moment between the ground and excited state $\Delta\mu$ as high as 14.4 D (see Experimental section, equations *(E2)*, *(E3)*). In a similar manner, the emission quantum yield Φ_{em} was found to be affected by the solvent polarity, showing values from 0.02 in PhMe up to 0.55 in CH_3CN (table 4.1).

Emission decay curves were recorded by the time-correlated single-photon counting (TCSPC) technique (figure 4.4, table 4.2). As reported in table 4.2, the emission decay was found to be mono-exponential in PhMe, but showed a bi-exponential behaviour in CH_3CN and THF, involving a main component τ_1 with a fraction of intensity $f_1 > 0.97$, and a short component τ_2 with a minor contribution to the emission intensity ($f_2 < 0.03$) and a decreasing weight at longer emission wavelengths (figure 4.4, table 4.2). Therefore, the major component τ_1, that drastically decreases moving to non-polar solvents, namely from 2.31 ns (in CH_3CN) to 0.14 ns (in PhMe), was assigned to the lifetime of the most stable form *s-trans-E* of **4.1**.[31,32] The minor component τ_2 could be ascribable, in first instance, to the presence of a very small fraction of *s-cis-E* isomer.

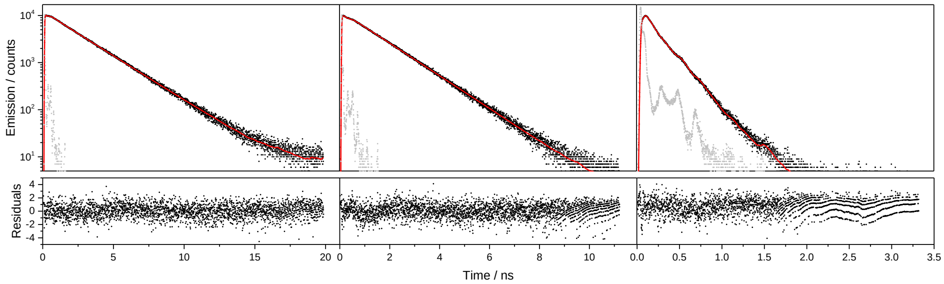

*Figure 4.4: Emission decays (black dots), internal response (grey dots) upon excitation at 400 nm, and fit (red line) of E-**4.1** in CH_3CN (left, λ_{em} = 620 nm), THF (centre, λ_{em} = 590 nm) and PhMe (right, λ_{em} = 550 nm).*

		Before irradiation			***After irradiation***		
Solvent	***λ_{em} / nm***	***τ_1 (β_1, f_1)^a***	***τ_2 (β_2, f_2)***	***τ_3 (β_3, f_3)***	***τ_1 (β_1, f_1)^a***	***τ_2 (β_2, f_2)***	***τ_3 (β_3, f_3)***
CH_3CN	580	2.31±0.01 (0.84,0.97)	0.43±0.04 (0.16,0.03)	--	2.31±0.01 (0.85,0.97)	0.43±0.04 (0.15,0.03)	--
	620	2.31±0.01 (0.89,0.98)	0.43±0.04 (0.11,0.02)	--	2.31±0.01 (0.89,0.98)	0.43±0.04 (0.11,0.02)	--
	660	2.31±0.01 (0.92,0.98)	0.43±0.04 (0.08,0.02)	--	2.31±0.01 (0.93,0.99)	0.43±0.04 (0.07,0.02)	--
THF	550	1.25±0.01 (0.86,0.97)	0.22±0.02 (0.14,0.03)	--	1.25±0.01 (0.84,0.97)	0.23±0.02 (0.16,0.03)	--
	590	1.25±0.01 (0.90,0.98)	0.22±0.02 (0.10,0.02)	--	1.25±0.01 (0.90,0.98)	0.23±0.02 (0.10,0.02)	--
	650	1.25±0.01 (0.93,0.99)	0.22±0.02 (0.07,0.01)	--	1.25±0.01 (0.92,0.99)	0.23±0.02 (0.08,0.01)	--
PhMe	500	1.6±0.1 (<0.01,0.01)	0.14±0.01 (0.79,0.97)	<0.01 (0.21,0.02)	1.7±0.1 (<0.01,0.01)	0.14±0.01 (0.76,0.97)	<0.01 (0.24,0.02)
	550	0.14±0.01 (1.00,1.00)	--	--	0.14±0.01 (1.00,1.00)	--	--
	590	0.14±0.01 (1.00,1.00)	--	--	0.14±0.01 (1.00,1.00)	--	--

Table 4.2: Lifetimes and contributions for each solvent at different observation wavelengths, upon excitation at 400 nm. ^{a} β_i*: pre-exponential factors;* f_i*: fractions of intensity* $f_i = \beta_i\tau_i/\Sigma(\beta_j\tau_j)$*.*

The photochromism of compound **4.1** was investigated in deaerated solvents. Irradiations in the visible range induced, in all the three solvents, appreciable variations of the absorption spectra, namely a decrease of the main band in the visible range and the uprising of the band comprised in the range 300-400 nm (figure 4.5, left). The isosbestic point observed between 395 and 400 nm suggests a clean transformation between two species. At the same time, the emission intensity decreases upon irradiation. These spectral changes are consistent with a photoinduced isomerization, from the most stable *E* form to the metastable *Z* form, as preliminarily reported in previous works.[9,31,32]

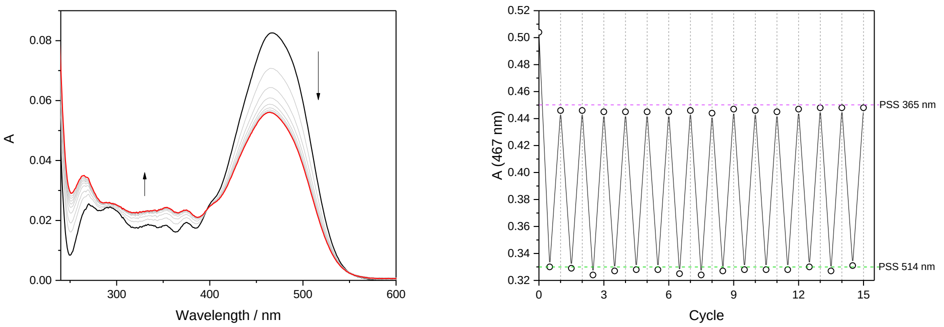

Figure 4.5: Left: absorption changes of a solution 1.6 × 10^{6} M of ***4.1*** *in THF upon irradiation at 514 nm; right: fatigue resistance of a solution of* ***4.1*** *in THF upon alternate irradiations at 514 nm and 365 nm.*

In order to test the reversibility and the fatigue resistance of the photoisomerization process, compound **4.1** was irradiated alternatively at 514 nm and 365 nm. The absorbance values showed, indeed, that the system can be photoswitched between the two isomers in a reversible manner and without any noticeable degradation at least after 15 cycles (figure 4.5, right). Since the *E* isomer is known to be the thermodynamically stable form, a spontaneous *Z-E* thermal isomerization could be expected after the irradiation. However, when the illuminated sample was kept in the dark, no appreciable variation of the absorbance was detected over a long period of time (1 day), suggesting that the thermal *Z-E* back-reaction is extremely slow, with half-life values $t_{1/2}$ spanning from approximatively few weeks (in THF) to more than one year (in PhMe). Therefore, compound **4.1** can be considered as an efficient bi-stable P-type photochromic compound.

Since the absorption spectra of the two configurational isomers *E* and *Z* extend over the same spectral range (*vide infra*), a prolonged illumination leads to a photostationary state (PSS), characterized by a degree of photoconversion $\alpha_Z(\lambda_{irr})$, *i.e.*, the fraction of *Z* form obtained under irradiation at a given λ_{irr}. Thanks to the difference in polarity and the good thermal stability of both *E* and *Z* isomers, the exact composition of the PSS obtained by irradiation at 514 nm was quantified by HPLC, as reported in table 4.3. It is worth noting that the highest *E-Z* photoconversion extent was obtained in THF at 514 nm ($\alpha_Z = 0.45$).

Consequently, the absorption spectra of the *Z* isomer in the three solvents were obtained from the corresponding spectra of the *E* isomer and the PSS, as displayed in figure 4.6, according to the equation:

$$A_z(\lambda) = A_E(\lambda) + \frac{A_{PSS}(\lambda) - A_E(\lambda)}{\alpha_z}$$

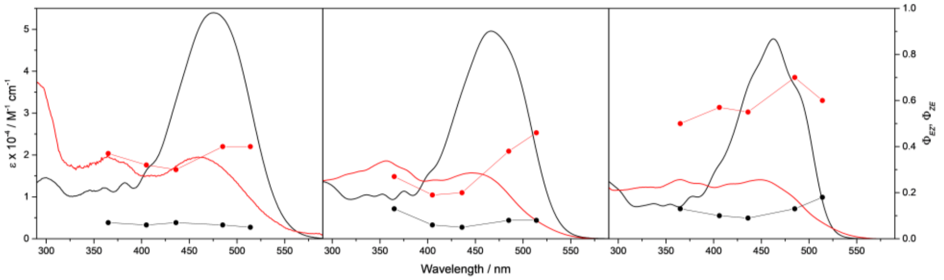

Figure 4.5: Absorption spectra of the E (black line) and Z (red line) isomers and photoisomerization quantum yields (line and dots) Φ_{EZ} (black) and Φ_{ZE} (red) of ***4.1*** *in CH_3CN (left), THF (centre) and PhMe (right).*

λ_{irr} / nm	CH₃CN			THF			PhMe		
	α_Z ᵃ	Φ_{EZ} ᵇ	Φ_{ZE} ᶜ	α_Z ᵃ	Φ_{EZ} ᵇ	Φ_{ZE} ᶜ	α_Z ᵃ	Φ_{EZ} ᵇ	Φ_{ZE} ᶜ
313	0.18	--	--	0.17	--	--	0.12	--	--
334	0.14	--	--	0.16	--	--	0.12	--	--
365	0.15	0.07	0.37	0.15	0.13	0.26	0.11	0.13	0.50
405	0.23	0.07	0.34	0.25	0.06	0.20	0.20	0.10	0.57
436	0.31	0.06	0.31	0.35	0.05	0.21	0.31	0.09	0.55
463	0.36	--	--	0.43	--	--	0.37	--	--
485	0.41	0.06	0.42	0.46	0.07	0.38	0.40	0.13	0.70
514	0.40ᵈ	0.05	0.43	0.45 ᵈ	0.07	0.43	0.43ᵈ	0.18	0.60
543	0.32	--	--	0.37	--	--	0.09	--	--
575	0.23	--	--	0.34	--	--	N.A.	--	--

Table 4.3: Photochemical parameters of ***4.1*** *in CH_3CN, THF and PhMe. ᵃ photoconversion at the PSS. ᵇ E-Z photoisomerization quantum yield. ᶜ Z-E photoisomerization quantum yield. ᵈ determined via HPLC methods.*

Photokinetic experiments on compound **4.1** under different irradiation wavelengths were carried out in CH_3CN, THF and PhMe, in order to quantify the photoisomerization quantum yields for the *E*-*Z* (Φ_{EZ}) and *Z*-*E* (Φ_{ZE}) reactions (table 4.3). For a given solvent, the value of Φ_{EZ} resulted to be weakly dependent on the irradiation wavelength, whereas the value of Φ_{ZE} showed a strong wavelength-dependence with a noticeable increase when irradiation in the red side of the absorption spectrum was employed.

Moreover, the solvent plays a key role in the photochromic reactivity of **4.1**.[9,31,32] The Φ_{EZ} quantum yield is similar between THF and CH_3CN (0.05 - 0.07) but improved in PhMe (0.09 - 0.18). The backward Φ_{ZE} quantum yield is much lower in THF (0.20 - 0.43) compared to CH_3CN and PhMe (up to 0.70). These photoisomerization quantum yields are consistent with the slightly larger values of conversion yields α_Z obtained in THF (large Φ_{EZ} but low Φ_{ZE}) compared to CH_3CN and PhMe.

To investigate the emission properties of *Z*-**4.1**, a correlation between the intensity of emission and the degree of photoconversion α_Z was performed. In all the three solvents, the fluorescence quenching represents exactly the conversion yield α_Z. Extrapolation of the data to total conversion suggests that the *Z* isomer is not emissive (figure 4.7, left). Moreover, the excitation spectra of the pure *E* form and of a solution of *E* and *Z* at the PSS are superimposable (figure 4.7, right), meaning that the emission is due to the sole *E* isomer. Finally, the absence of variations in the decay times and pre-exponential factors before and after irradiation (table 4.2) suggests that the measured values are ascribable to the *E* forms only, namely the *s-trans-E* and *s-cis-E* isomers, as already discussed.

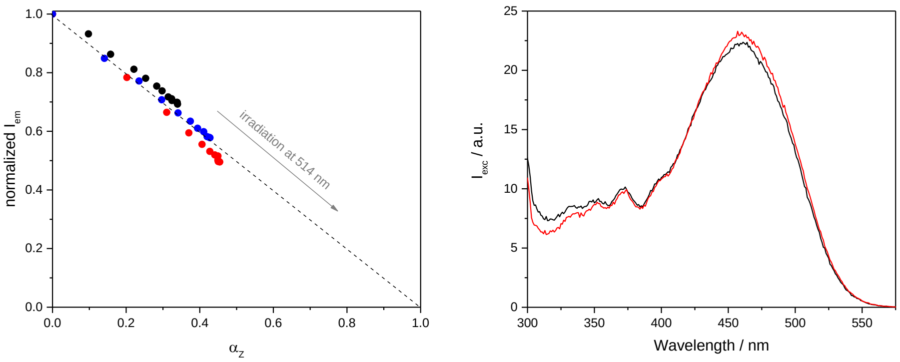

*Figure 4.7: Left: correlation plot of the normalized emission intensity and the photoconversion α_Z of **4.1** upon irradiation at 514 nm in CH_3CN (black dots), THF (red dots) and PhMe (blue dots); right: excitation spectra (λ_{em} = 600 nm) in THF of a solution of **4.1** before (black line) and after (red line) exhaustive irradiation at 514 nm.*

Assuming that the Φ_{em} and τ_1 are related to the main *s-trans-E* isomer, the deactivation rate constants can be determined (table 4.4). The magnitude of the radiative rate constant (k_r) is almost unchanged in the three solvents (1.4 - 2.6 × 10^8 s^{-1}), meaning that the electronic structure of the emissive state does not critically depend on the solvent polarity. Conversely, the non-radiative deactivation rate constant (k_{nr}), which includes the photoreaction processes, increases dramatically from polar to non-polar solvents, namely from 2.0 × 10^8 s^{-1} in CH_3CN to 7.0 × 10^9 s^{-1} in PhMe. This effect can be attributed both to the intrinsic vibrational relaxation of the excited state and the solvent-dependent *E*-*Z* photoreactivity (vide infra).

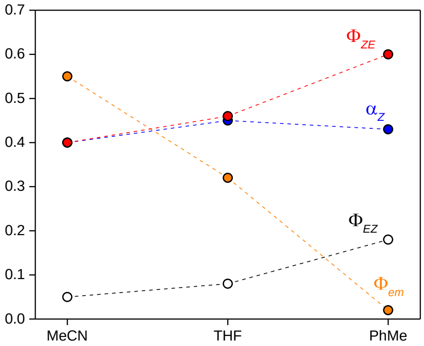

*Figure 4.8: Comparison between the photoconversion α_Z at 514 nm (blue), the photoconversion quantum yields at 514 nm (white and red) and the fluorescence quantum yield (orange) of **4.1** in the three solvents.*

Solvent	k_r / s^{-1}	k_{nr} / s^{-1}
MeCN	2.3 × 10^8	2.0 × 10^8
THF	2.2 × 10^8	5.8 × 10^8
PhMe	1.4 × 10^8	7.0 × 10^9

*Table 4.4: Radiative (k_r) and non-radiative (k_{nr}) constants of **4.1** in the three solvents.*

In terms of fluorescence photoswitching,[33] the THF appears to be the most suitable solvent for compound **4.1**, since it represents the best compromise between a good *E*/*Z* photoconversion under visible light and a still appreciable fluorescence quantum yield of the *E* isomer, as summarized in figure 4.8.

Theoretical calculations were carried out to elucidate the number and geometry of the different isomeric states of **4.1** as well as their absorption spectra. DFT and TD-DFT computations were performed with a PBE0 functional and a 6-311G+(d,p) basis set, including the IEFPCM solvent model for THF. The geometry optimizations provided the conformation, ground state energies and the dipolar moments of the four isomers identified: *s-trans-E*, *s-cis-E*, *s-trans-Z*, *s-cis-Z* (figure 4.9). As expected, the *s-trans-E* form is the most stable form, whereas the *s-cis-E* is only 1.8 kcal mol^{-1} less stable than the former. Based on these relative energies, the Boltzmann distribution provides a thermal population of *s-trans-E* : *s-cis-E* around 95:5, which is consistent with the small fraction of the component β_2 observed by time-resolved fluorescence (*vide infra*). On the contrary, both the *Z* isomers are much higher in energy: the *s-cis-Z* isomer resulted to be 7.7 kcal mol^{-1} higher than the *s-trans-E*, and slightly more stable (by 0.6 kcal mol^{-1}) than the *s-trans-Z*. The dipole moments are comparable between the two *E* isomers (19 D) and the *s-trans-Z* (17 D), while that of the *s-cis-Z* is much lower (12 D), most likely due to the strongly folded geometry adopted in this conformer.

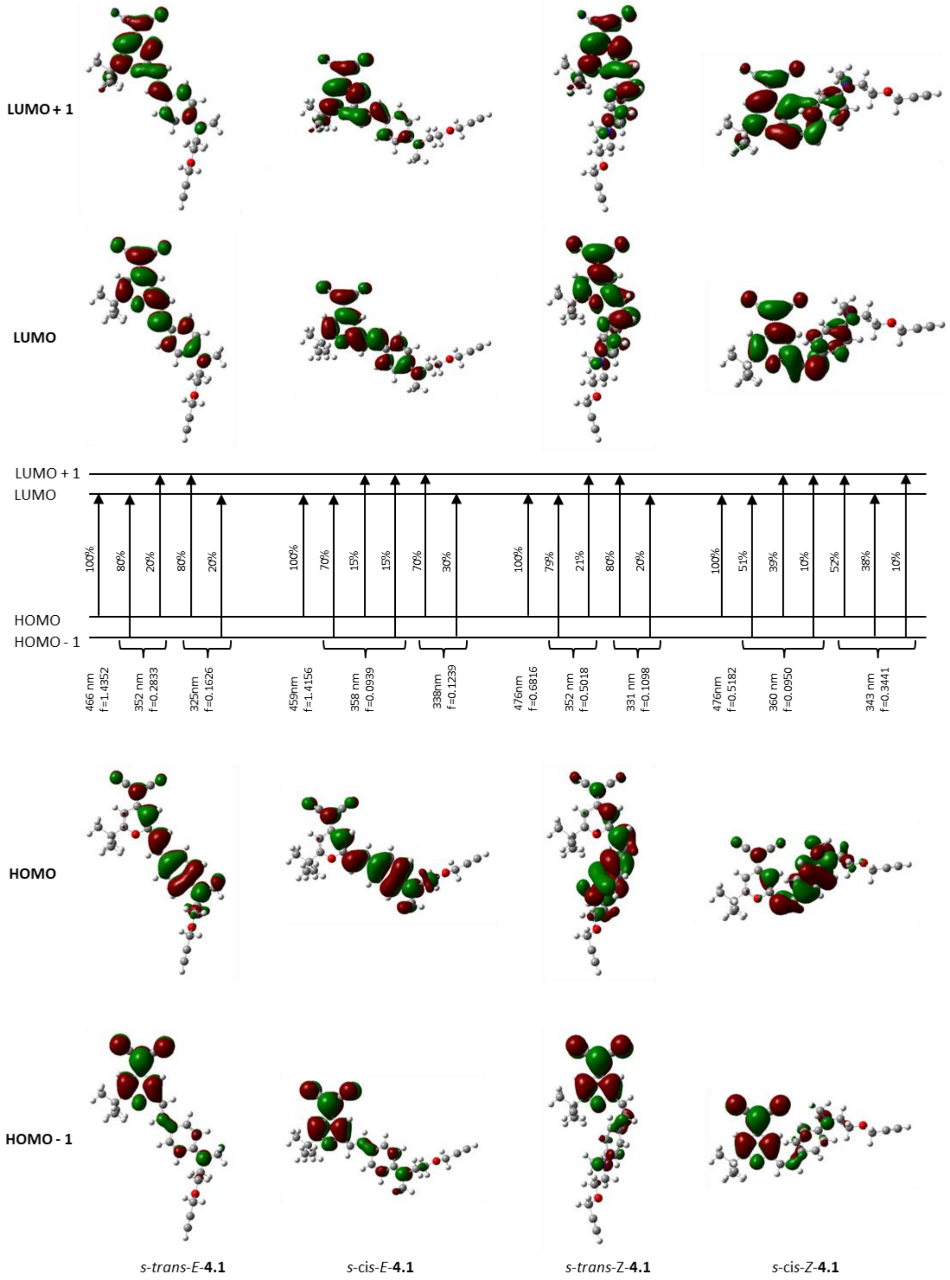

Figure 4.9: Schematic representation of the first three electronic transitions, with the related oscillator strengths (f), and of the involved molecular orbitals as computed in THF.

The simulated absorption spectra are in good agreement with the experimental results and confirm that each of the four isomers contributes to the overall absorption spectrum (figure 4.10). For the four isomers, the first electronic transition corresponds to a pure HOMO-LUMO transition (figure 4.9), showing a π-π* character and a clear intramolecular CT character from the electron-donating phenylamino fragment to the electron-withdrawing dicyanomethylenepyran fragment.[11] Therefore, the basic topology of the frontier orbitals can explain the solvatochromism and photoisomerization properties of compound **4.1**.

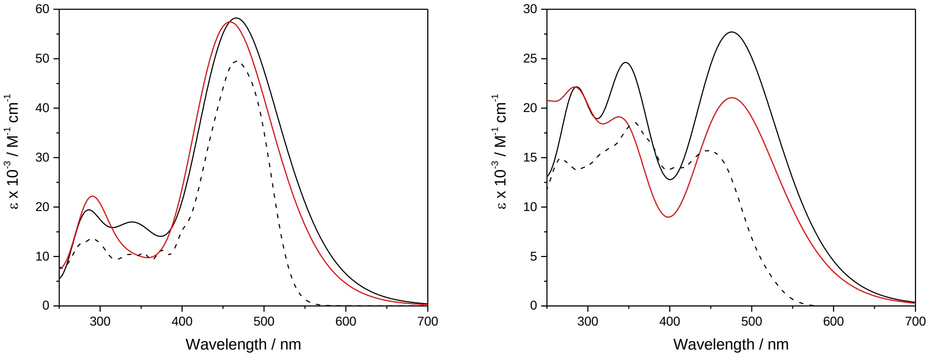

Figure 4.10: Computed absorption spectra of the s-trans (full black lines) and s-cis (full red lines) conformers and experimental spectra (dashed black lines) of the configurational isomers E (left) and Z (right) in THF.

Compound **4.2** was synthesized with the same procedure as for compound **4.1**, with a triphenylamino substituent on the double bond. The absorption spectrum in THF shows a main band, centred at 458 nm and with ε = 54000 M^{-1} cm^{-1}, and a minor band in the UV region, centred at 301 nm and with ε = 31000 M^{-1} cm^{-1} (figure 4.11).

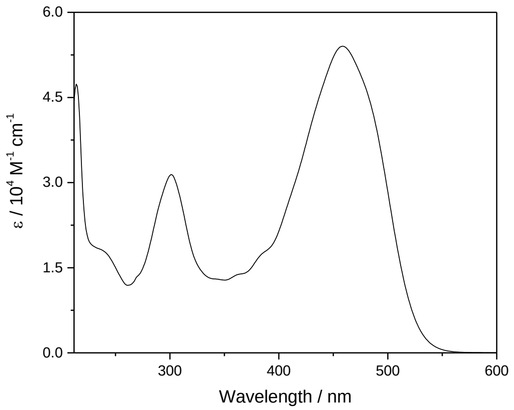

Figure 4.11: Absorption spectrum of ***4.2*** *in THF.*

Irradiation of compound **4.2** at different wavelengths produced absorption variations compatible with a *E*/*Z* photoisomerization, albeit with a lower photoconversion with respect to compound **4.1** (figure 4.12).

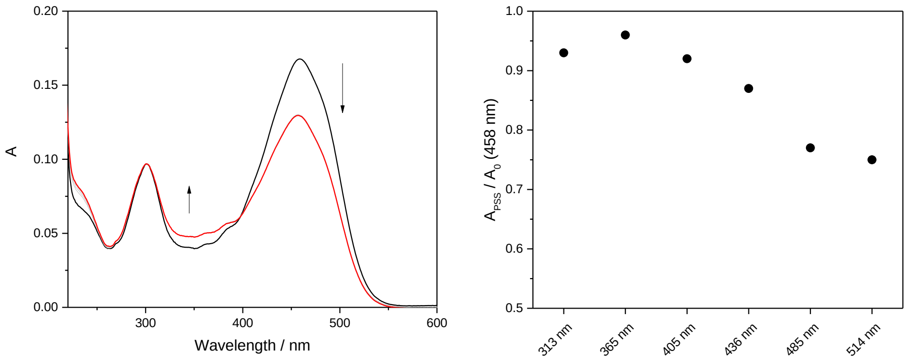

Figure 4.12: Left: Absorbance changes of a solution of ***4.2*** *upon irradiation at 485 nm; right: absorbance ratios at the PSS obtained upon irradiation at different wavelengths.*

Nevertheless, spectra recorded on a solution of **4.2** kept in the dark, over several days, revealed a large absorbance increase in the UV region (figure 4.13), suggesting that, indeed, the compound is not stable in time. Moreover, these changes are not compatible with those related to the photoinduced process and cannot be ascribed to a thermal *Z*-*E* isomerization.

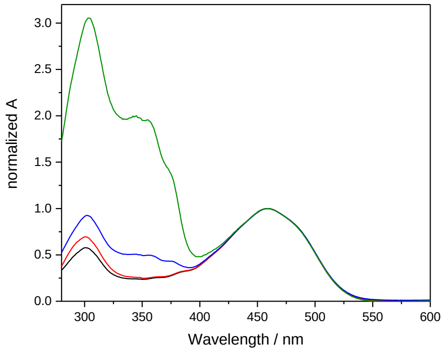

*Figure 4.13: Normalized absorbance changes of a solution of **4.2** after 1 day (red line), 3 days (blue line), 15 days (green line).*

Compound **4.3** differs from compound **4.2** in the pyranil moiety, which has been replaced with a benzopyranil unit. Its absorption spectrum in THF (figure 4.14) displays three main bands, namely one main band at 494 nm, with ε = 41000 M^{-1} cm^{-1}, and two bands in the UV region, one at 302 nm and the other between 380 and 400 nm.

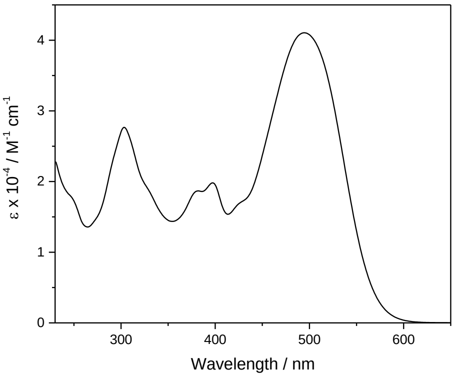

*Figure 4.14: Absorption spectrum of **4.3** in THF.*

Surprisingly, irradiation of **4.3** in the visible region did not produce any appreciable variation in the absorption spectrum. Conversely, when irradiated for long time intervals in the UV, the absorption spectrum of **4.3** displays little variations (figure 4.15).

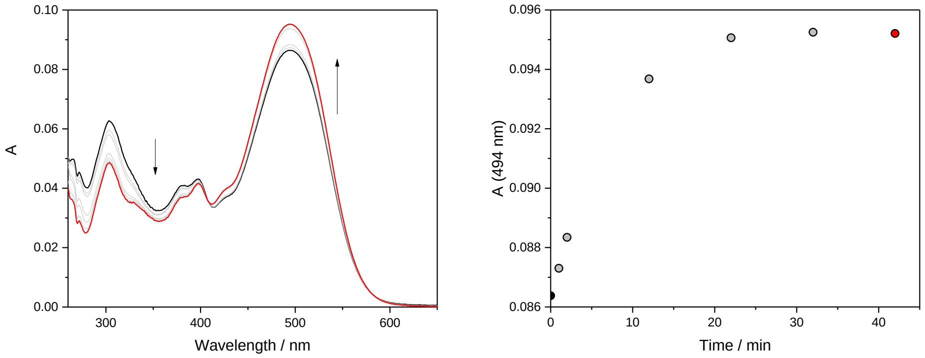

Figure 4.15: Left: absorption changes of a solution of ***4.3*** *upon irradiation at 365 nm; right: absorbance changes at 494 nm.*

These preliminary studies on the unexpected photochemical behaviour of this compound would suggest that isomerization does not occur, and the absorbance variations upon prolonged energetic irradiation are caused instead by a photodegradation of the compound. Further investigations on the reversibility of the process and on its stability are currently ongoing in the research group.

4.3 Multi-component DCM derivatives

Compound **4.4** was synthesized by means of click chemistry, starting from a mannose derivative bearing three propargyl groups on the oxygens in *2*, *3* and *4*-positions and an azido derivative of **DCM**. The resulting structure is a mannopyranose with one **DCM** moiety in axial position and two in equatorial position. The absorption and emission spectra of **4.4** in THF possess the same spectral features of the monomer **4.1** (figure 4.16). The main absorption band in the visible region takes place at 458 nm, only marginally blueshifted with respect to the parent compound **4.1**, and with a molar absorption coefficient of 148000 M^{-1} cm^{-1}, in line with the presence of three chromophoric units. The emission spectrum is slightly blueshifted with respect to **4.1** as well.

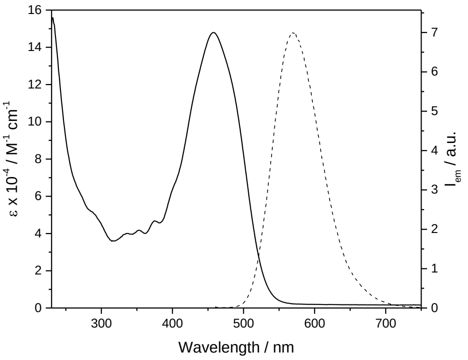

*Figure 4.16: Absorption (full line) and emission (dashed line) of **4.4** in THF.*

The emission quantum yield Φ_{em} of **4.4** is 0.10, one third of the Φ_{em} of **4.1**. The reduced efficiency of the luminesce in the multicomponent structure can be due to additional non-radiative deactivation paths. The emission decay of **4.4** is multiexponential, with 4 decay time components (figure 4.17 and table 4.5).

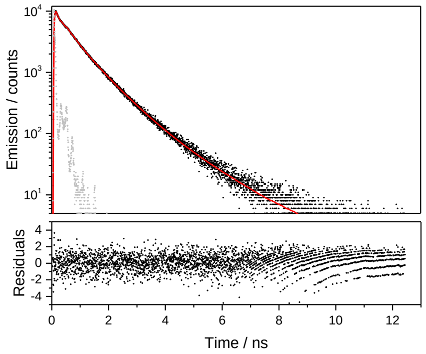

*Figure 4.17: Emission decays (black dots), internal response (grey dots) upon excitation at 400 nm, and fit (red line) of EEE-**4.4** in THF (λ_{em} = 570 nm).*

Absorption		***Emission***		***Lifetimes***			
λ_{abs} / nm	***ε / M^{-1} cm^{-1}***	***λ_{em} / nm***	***Φ_{em}***	***τ_1 / ns (β_1, f_1)^a***	***τ_2 / ns (β_2, f_2)***	***τ_3 / ns (β_3, f_3)***	***τ_4 / ns (β_4, f_4)***
458	148000	570	0.10	1.80 (0.05, 0.15)	0.82 (0.47, 0.66)	0.31 (0.32, 0.17)	0.07 (0.16, 0.02)

*Table 4.5: Photophysical properties of **4.4** in THF. ^{a} β_i: pre-exponential factors; f_i: fractions of intensity $f_i = \beta_i\tau_i/\Sigma(\beta_j\tau_j)$*

The photochemical behaviour of **4.4** is comparable with that of its subunit **4.1**: irradiation with UV or visible light produces spectral changes ascribable to the *E*/*Z* photoisomerization. However, the extent of photoconversion in **4.4** is apparently much lower with respect to **4.1**.

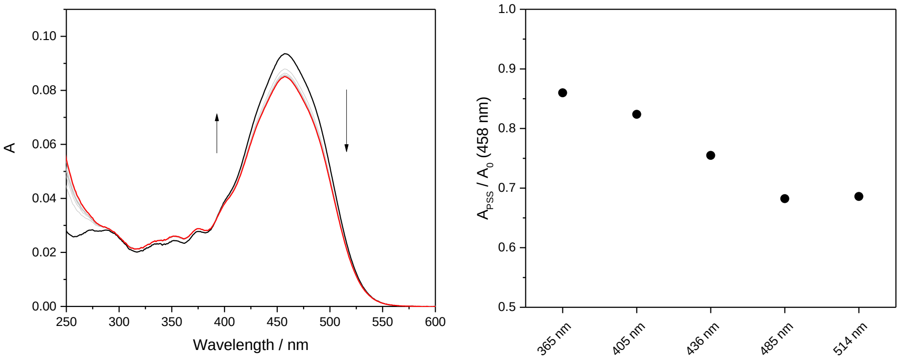

Figure 4.17: Left: Absorbance changes of a solution of ***4.4*** *upon irradiation at 514 nm; right: absorbance ratios at the PSS obtained upon irradiation at different wavelengths.*

The correlation plot between the evolution of the emission and the absorption during the irradiation with visible light is a straight line as in the case of compound **4.1**. In the same manner, the Mauser plot[34] obtained from the absorbance values of the same absorption spectra gives a straight line. These two plots would suggest that no cooperative effects are exerted by the photoisomerization process, *i.e.*, the photochemistry of each **DCM** unit does not depend on the configuration of the two reminder ones, and the multicomponent structure photoisomerizes as an ensemble of isolated photochromes.

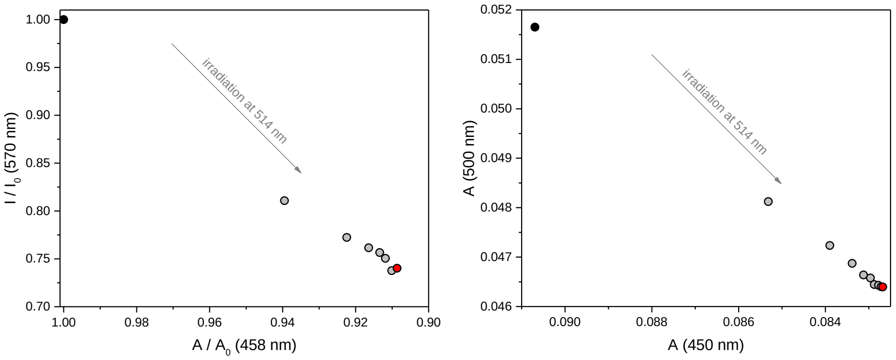

Figure 4.18: Left: correlation plot between the emission and the absorbance variations upon irradiation at 514 nm; right: Mauser plot of the absorbance variations (500 nm vs 450 nm) upon irradiation at 514 nm.

Since the three **DCM** units are bound to the same scaffold, it is reasonable to assume that homo-energy transfer could take place. In this regard, steady-state and time-resolved anisotropy measurements were carried out on the single and multicomponent structures. A steady-state excitation anisotropy experiment was conducted by monitoring the emission anisotropy value (r), collected at the λ_{max} of the emission spectrum, upon scanning of the excitation wavelength. The value of r of **DCM** in frozen propylene glycol (figure 4.19, top left) approaches 0.4 on the main visible band. However, on the same band of compound **4.4**, the polarization is lost and the anisotropy drops to 0.2, but approaches higher values on the red edge of the spectrum. This lower value is compatible with an energy transfer process, that becomes gradually less efficient at lower excitation energies (Weber's red edge effect).[35,36] The time-resolved measurements on compound **4.4**, in propylene glycol at room temperature, evidenced a lower initial value of r and slower decay time ($\phi = 19.2$ ns) than for compound **4.1** ($\phi = 8.3$ ns). The simplest hypothesis is that the loss of polarization caused by the energy transfer occurs in sub-picosecond timescales, whereas the loss of polarization caused by brownian motion, responsible for the slower decay time, takes place in longer timescales on account of the larger molecular weight of the multicomponent structure. However, due to the multiple values of emission and anisotropy decay times, the data treatment is non-trivial and requires further investigations.

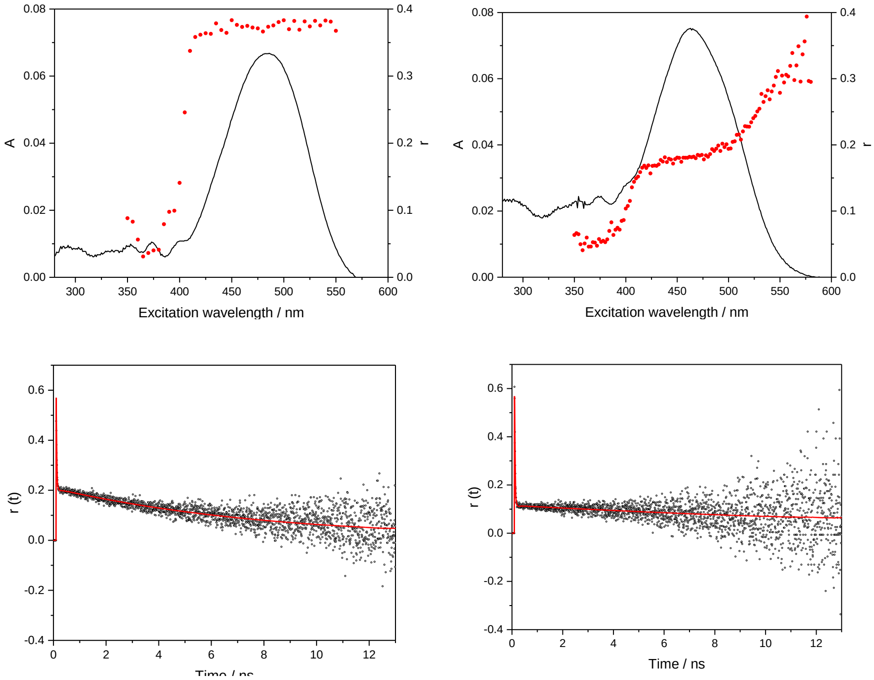

Figure 4.19: Top: absorption (full lines) and anisotropy values for each excitation wavelength (red dots) of ***4.1*** *(left, -45°C) and* ***4.4*** *(right, -57°C) in propylene glycol; bottom: anisotropy decays (dots) and fitting (red line) of* ***4.1*** *(left) and* ***4.4*** *(right) in propylene glycol at r.t.*

As it happened for compound **4.2**, compound **4.4** resulted to be unstable over large timescales (several days) and in a non-reproducible behaviour. In particular, an uprising of a band around 350 nm is evidenced, that eventually leads to a bleaching of the solution. Studies on the stability of this multicomponent structures and of the possible degradation products are underway in the research group.

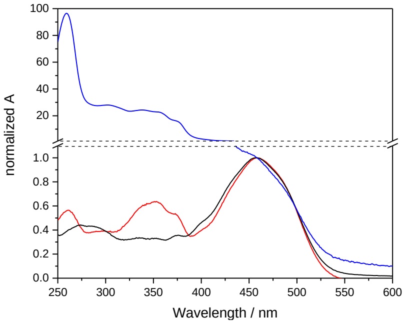

Figure 4.20: Absorbance variations in time of two solutions of ***4.4*** *after two weeks (red line) and three days (blue line) with respect to a fresh solution (black line).*

4.4 Conclusion and perspectives

In conclusion, single and multicomponent fluorescent and photochromic **DCM**-based derivatives have been reported. Compound **4.1** undergoes *E*/*Z* photoisomerization under UV-vis irradiation. The *E* and *Z* isomers have been separated by HPLC methods, thus allowing a precise determination of the conversion yield. The fluorescence of the *E* form resulted to be strongly sensitive to the solvent, especially in terms of emission colour and quantum yields. The *E* isomer exists mostly in its *s-trans-E* form, as determined by single crystal XRD, but also in a small fraction of *s-cis-E* form, as demonstrated by time-resolved spectroscopy and theoretical calculations. The *Z* isomer is not emissive and thermally stable in the typical experimental timescales. The detailed investigation of the photochromic quantum yields Φ_{EZ} and Φ_{ZE} of the compound **4.1** highlights the great sensitivity of its photoreactions to solvent polarity and irradiation wavelength. Compounds **4.2** and **4.3**, both bearing a triphenylamino substituent in the electron-donating portion of the molecule and different degrees of substitution on the pyranyl moiety, were also studied. Compound **4.2** can undergo *E*/*Z* photoisomerization with lower photoconversion but it is not stable over time. On the other hand, compound **4.3** shows absorption changes only under prolonged irradiation in the UV region, that could be ascribed to a photodegradation. Compound **4.4** is composed of a mannose scaffold decorated with three **4.1** units. Preliminary studies suggest that the three **DCM** units behave independently both photochemically and photophysically, albeit with more efficient deactivation paths, that result in reduced photoisomerization and fluorescence quantum yields. Moreover, anisotropy measurements revealed that homo-energy transfer could take place between the three **DCM** moieties. However, this compound is not stable over time, and it is currently still under study in the research group. Considering the wide range of applications involving the **DCM** fluorophore, such an insight into the photochemical and photophysical properties of its single and multicomponent fluorophoric and photochromic derivatives is expected to open important perspectives in terms of photo-responsive molecular probes and materials.

4.5 References

1. V. Balzani, A. Credi, and M. Venturi, *Molecular Devices and Machines– A Journey into the Nano World*. Wiley-VCH, Weinheim, **2004**.
2. B. L. Feringa and W. R. Brown, *Molecular Switches*, 2nd ed. Wiley-VCH, Weinheim, **2011**.
3. H. Dong, H. Zhu, Q. Meng, X. Gong, and W. Hu, *Chem. Soc. Rev.*, **2012**, *41*, 1754–1808.
4. Z. Tian and A. D. Li, *Acc. Chem. Res.*, **2013**, *46*, 269–279.
5. M. E. Gemayel, K. Borjesson, M. Herder, *et al.*, *Nat. Commun.*, **2015**, *6*, 6330.
6. P. R. Hammond, *Opt. Commun.*, **1979**, *29*, 3, 331–333.
7. M. Meyer and J. C. Mialocq, *Opt. Commun.*, **1987**, *64*, 3, 264–268.
8. J. Bourson and B. Valeur, *J. Phys. Chem.*, **1989**, *93*, 9, 3871–3876.
9. M. Meyer, J. C. Mialocq, and B. Perly, *J. Phys. Chem.*, **1990**, *94*, 1, 98–104.
10. A. J. Van Tassle, M. A. Prantil, and G. R. Fleming, *J. Phys. Chem. B*, **2006**, *110*, 38, 18989–18995.
11. I. D. Petsalakis, D. G. Georgiadou, M. Vasilopoulou, *et al.*, *J. Phys. Chem. A*, **2010**, *114*, 5580–5587.
12. Y. Suzuki and K. Yokoyama, *J. Am. Chem. Soc.*, **2005**, *127*, 50, 17799–17802.
13. W. Zhu, X. Huang, Z. Guo, X. Wu, H. Yu, and H. Tian, *Chem. Commun.*, **2012**, *48*, 12, 1784–1786.
14. Y. Zheng, M. Zhao, Q. Qiao, H. Liu, H. Lang, and Z. Xu, *Dye. Pigment.*, **2013**, *98*, 3, 367–371.
15. X. Wu, X. Sun, Z. Guo, *et al.*, *J. Am. Chem. Soc.*, **2014**, *136*, 9, 3579–3588.

16. S. Chen, Y. Fang, Q. Zhu, W. Zhang, X. Zhang, and W. Lu, *RSC Adv.*, **2016**, *6*, 85, 81894–81901.

17. C. Ma, B. Zhang, Z. Liang, *et al.*, *J. Mater. Chem.*, **2002**, *12*, 6, 1671–1675.

18. Q. Peng, Z. Y. Lu, Y. Huang, *et al.*, *Macromolecules*, **2004**, *37*, 2, 260–266.

19. M. K. Leung, C. C. Chang, M. H. Wu, *et al.*, *Org. Lett.*, **2006**, *8*, 12, 2623–2626.

20. Y. S. Yao, J. Xiao, X. S. Wang, Z. B. Deng, and B. W. Zhang, *Adv. Funct. Mater.*, **2006**, *16*, 5, 709–718.

21. W. Ballet, I. Picard, T. Verbiest, A. Persoons, and C. Samyn, *Macromol. Chem. Phys.*, **2004**, *205*, 1, 13–18.

22. R. Andreu, L. Carrasquer, J. Garín, *et al.*, *Tetrahedron Lett.*, **2009**, *50*, 24, 2920–2924.

23. L. Jullien, J. Canceill, B. Valeur, *et al.*, *J. Am. Chem. Soc.*, **1996**, *118*, 23, 5432–5442.

24. K. Ouhenia-Ouadahi, R. Métivier, S. Maisonneuve, *et al.*, *Photochem. Photobiol. Sci.*, **2012**, *11*, 11, 1705–1714.

25. S. Maisonneuve, R. Métivier, P. Yu, K. Nakatani, and J. Xie, *Beilstein J. Org. Chem.*, **2014**, *10*, 1471–1481.

26. Z. Guo, W. Zhu, L. Shen, and H. Tian, *Angew. Chem. Int. Ed.*, **2007**, *46*, 29, 5549–5553.

27. Z. Guo, P. Zhao, W. Zhu, X. Huang, Y. Xie, and H. Tian, *J. Phys. Chem. C*, **2008**, *112*, 17, 7047–7053.

28. Z. Guo, W. Zhu, Y. Xiong, and H. Tian, *Macromolecules*, **2009**, *42*, 1448–1453.

29. Z. Guo, W. Zhu, and H. Tian, *Chem. Commun.*, **2012**, *48*, 49, 6073–6084.

30. J. M. Drake, M. L. Lesiecki, and D. M. Camaioni, *Chem. Phys. Lett.*, **1985**, *113*, 6, 530–534.

31. M. Meyer, J. C. Mialocq, and M. Rougée, *Chem. Phys. Lett.*, **1988**,

150, 484–490.

32. J. M. Drake, M. L. Lesiecki, and D. M. Camaioni, *Chem. Phys. Lett.*, **1985**, *113*, 6, 530–534.

33. B. Shao, M. Baroncini, H. Qian, *et al.*, *J. Am. Chem. Soc.*, **2018**, *140*, 12323–12327.

34. H. Mauser, *Z. Naturfosch*, **1968**, *23b*, 1025–1030.

35. G. Weber, *Biochem. J.*, **1960**, *75*, 2, 345–352.

36. J. R. Lakowicz, *Principles of fluorescence spectroscopy*, 3rd ed. Springer US, **2006**.

Part B

Electro-responsive supramolecular devices

Chapter 5.

New geometries for calixarene-bipyridinium rotaxanes and pseudorotaxanes

5.1 Introduction and aim

In the last decades, calix[6]arenes have been widely exploited as macrocyclic receptors for host-guest chemistry.[1,2] Their molecular structure is composed by six arenic units, linked by methylenic bridges, which, in most of the cases, arrange in a stiff peculiar goblet-like structure (hence the name), with two rims: the "upper" rim, whose diameter is the largest and the "lower" rim, with a smaller diameter. However, the arenic units can arrange also in *alternate* conformations, thus an alternative nomenclature, *i.e.*, "wide" and "narrow" rim, is preferred, since it has the advantage of being orientation-independent.[3] The cavity is non-polar and π-rich, therefore calixarenes are able to bind, with high stability constants, non-polar π-poor guests. On the basis of these considerations, in 2000, Arduini et al. developed the first examples of pseudorotaxanes formed by calix[6]arenes and N,N′-dialkyl-4,4′-bipyridinium (henceforth called "viologen") salts (figure 5.1).[4] For this purpose, the upper rim of the calixarene had been decorated with three phenylureido groups, as receptors for the counterions of the viologen salt.[5–7] In such supramolecular adducts, the viologen unit occupies the calixarene cavity and it is stabilized by π-π charge transfer (CT) from the six electron-rich rings of the macrocycle to the electron-poor bipyridinium. This CT interaction is eventually responsible for the characteristic red colour of the solutions of such pseudorotaxanes.

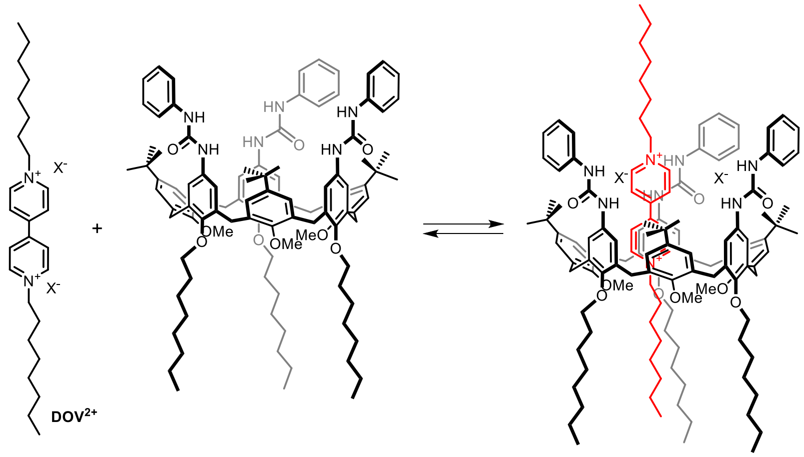

Figure 5.1: Pseudorotaxane formation between ***DOV***$^{2+}$ *and calix[6]arene, as reported by Arduini and coworkers.*[4]

Following studies,[8] conducted on dioctylviologen (**DOV**$^{2+}$) axles with different counterions, were devoted to elucidate the kinetics and thermodynamics of the pseudorotaxane formations. It was demonstrated that the threading process and the stability constant are largely affected by the nature of the guest counterions. Indeed, when the guest threads, its counteranions remain paired to the ureido receptors on the upper rim of the calixarene. Therefore, the stronger is this binding, the more stable is the complex. Moreover, since the bipyridinium moiety loses the counterions prior to the threading in the calixarene, the overall formation of the supramolecular complex is in competition with the guest ion pairing.[5,6] It has also been supposed that the threading of the viologen follows a transition state where the counteranions surround no more the guest, but they are already interacting with the calixarene.[8]

Since the calixarene is a non-symmetrical host, a directionality in the threading motion can be defined. It was found out that the threading occurs exclusively from the upper rim, because the counterions have to bind to the phenylureas prior to the threading and, moreover, the alkoxy chains appended to the lower rim are oriented inside the cavity, closing, as a matter of fact, the access from this gate.[11] Moreover, the shorter is the alkyl chain of the axle, the faster is the threading. Thus, in presence of non-symmetrical viologen salts, with two extremities of different length, only one orientational isomer is eventually yielded (figure 5.2).[12] In other words, the calixarene is capable of self-sorting both intramolecularly (*i.e.*, the shortest extremity of the axle threads) and intermolecularly (*i.e.*, the axle bearing the shortest chains threads).[12]

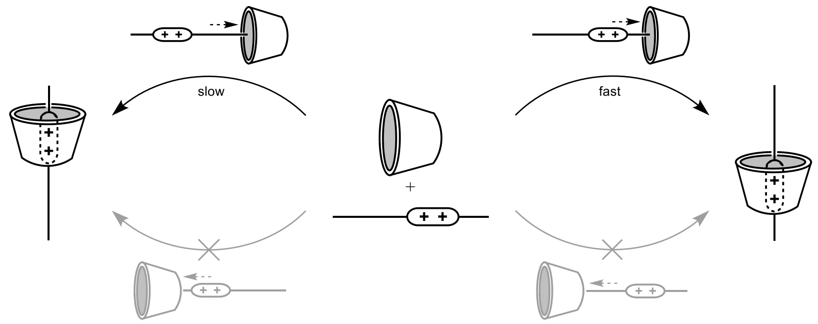

Figure 5.2: Schematic representation of the possible orientational isomers obtained upon assembly of a calixarene and a non-symmetrical bipyridinium axle. The processes depicted by grey arrows do not occur.

Due to the electroactivity of the bipyridinium unit, supramolecular structures based on the calix[6]arene-viologen recognition pattern can behave as molecular devices or machines, operated by an electronic stimulus. The dicationic bipyridinium moiety can be mono- or bi-reduced at negative potential. Moreover, when the bipyridinium is inside the calixarene, and therefore it is involved in a CT interaction, the reduction processes occur at more negative potentials. Usually, the stability constant of the complex drops significantly after the first reduction, forcing the calixarene to move apart from the viologen. In terms of molecular machinery, such a behaviour represents an example of electron-triggered movement.[13–16] Examples of shuttling in rotaxanes and rotation in catenates, with one component (the axle or one ring) endowed with one bipyridinium and one ammonium stations, have been reported.[17,18]

The work herewith presented aims to the characterization of new geometries of calixarene-viologen supramolecular structures. In particular, a new calix[6]arene decorated with two phenylureido groups instead of three, as in previously reported similar compounds, will be investigated in its free form and in related supramolecular structures. This study is of high interest in exploring new molecular hosts and in further understanding the mechanism and energetics of the assembly process.[19] A second study will focus on the investigation of a [*c1*] scorpionate compound, *i.e.*, a calixarene-viologen hermaphroditic pseudorotaxane where the axle is both covalently linked and self-threaded into the macrocycle. Such molecular arrangement, sometimes called also "molecular lasso" or "molecular ouroboros",[20] is the simplest modulus of the [c*n*]daisy-chain architectures, where *n* represents the number of monomers in the assembly. The study on its electrochemical behaviour can form the basis of new daisy-chain polymers able to give mechanical motions, like extension-contraction in molecular muscles.[16]

5.2 Diphenylureido-calixarenes as hosts for rotaxanes and pseudorotaxanes

Compound **5.1** was synthesized in the group of Prof. A. Arduini and Prof. A. Secchi (University of Parma). The arenic units in position *1* and *4* bear a N-phenylureido group and an octyloxy chain, in *para* position with respect to the former (figure 5.3, top). From detailed NMR studies conducted in $CDCl_3$, it has been shown that this macrocycle can adopt three possible conformations in solution, namely one *cone* and two *1,2,3-alternate* conformations (figure 5.3). In the *cone* conformation, the two phenylureido groups are arranged on the same rim of the cavity, whereas in the *alternate* conformations, they are oriented in opposite directions. The two *alternate* conformers differ by the reciprocal orientation of the remainder arenic units. Furthermore, it has been demonstrated that **5.1** prefers to adopt an *alternate* conformation both in solution and in the solid state.

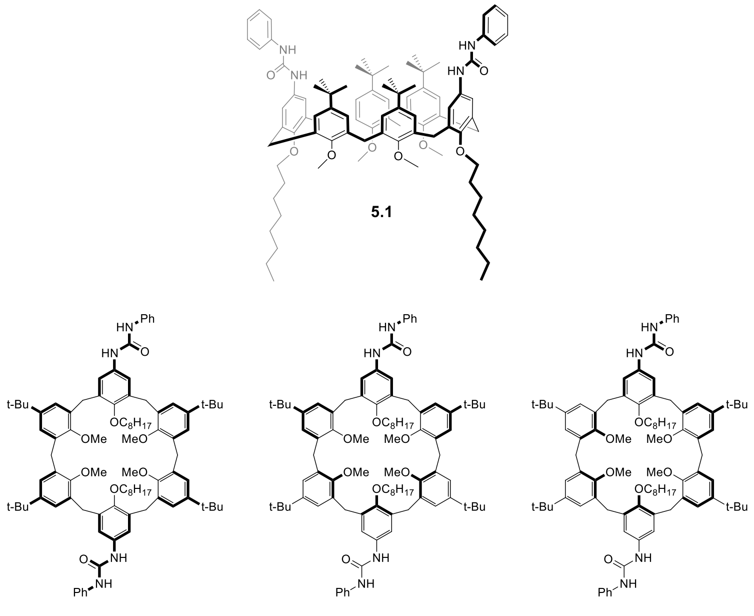

5.1

cone *1,2,3-alternate*-1 *1,2,3-alternate*-2

Figure 5.3: Top: molecular structure of ***5.1****; bottom: cone and alternate conformations.*

Pseudorotaxane **5.2** can be obtained, in suitable non-protic solvents such as CH_2Cl_2, by addition of **DOVTsO**$_2$ (*1,1′*-dioctyl-*4,4′*-bipyridinium ditosylate salt) to **5.1**, in equimolar amounts. The different conformations assumed by the calixarene are maintained in the pseudorotaxane, which shows several sets of NMR signals, that were assigned to the different supramolecular co-conformers, *i.e.*, adducts with the calixarene either in *alternate* and *cone* conformations (figure 5.4). Rotaxane **5.3** was synthesized by threading the di-hydroxydodecylviologen dication in the calixarene **5.1**, followed by the stoppering of the two ends of the axle with diphenylacetic units. Even in this case, the macrocycle was shown to adopt the already mentioned co-conformations (figure 5.4).

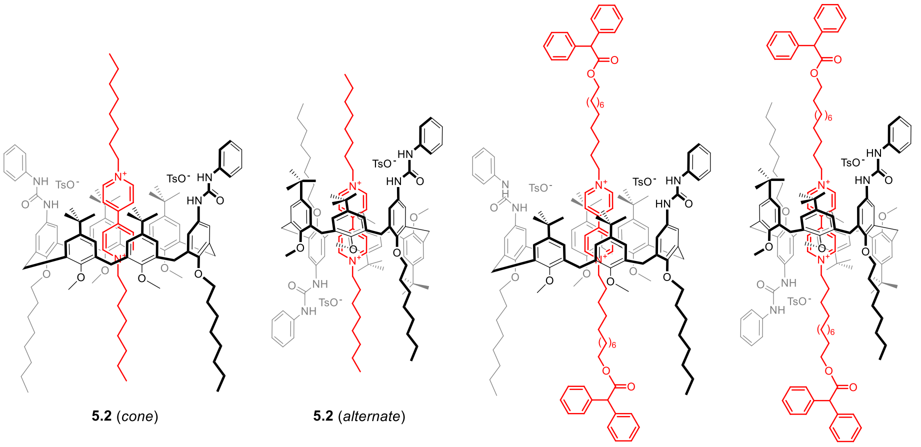

5.2 (*cone*) **5.2** (*alternate*) **5.3** (*cone*) **5.3** (*alternate*)

Figure 5.4: Molecular structures of the cone and alternate conformers of ***5.2*** *(left) and* ***5.3*** *(right). The axles are represented in red for clarity.*

The molecular components and the interlocked structures were characterized by UV-vis spectroscopy in CH_2Cl_2. The absorption spectrum of calixarene **5.1** (figure 5.5, left) consists in an intense band in the UV, centred at 260 nm and with an absorption coefficient of 38000 M^{-1} cm^{-1}. This band is redshifted and less intense with respect to the parent calix[6]arene bearing three phenylureido moieties.[8] The difference in the absorption can be due either to the lack of one chromophoric unit or to the different conformations assumed by the molecule in solution.

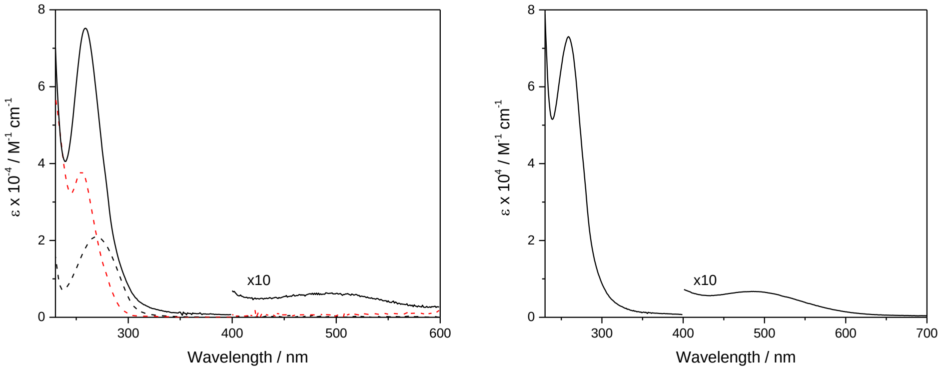

Figure 5.5: Left: absorption spectra of ***DOVTsO₂*** *(black dashed line), calixarene* ***5.1*** *(red dashed line) and pseudorotaxane* ***5.2*** *(black solid line) in CH_2Cl_2; right: absorption spectrum of rotaxane* ***5.3*** *in CH_2Cl_2.*

For pseudorotaxane **5.2**, the encapsulation of **DOV**$^{2+}$ in the macrocycle is confirmed by a CT band at 490 nm with $\varepsilon = 630$ M^{-1} cm^{-1}, which confers the characteristic red colour to the solution (figure 5.5, right). This peculiar band is commonly observed in similar supramolecular adducts based on calixarenes and viologens, as a result of a charge transfer interaction between the six electron-rich arenic units of the host and the electron-deficient bipyridinium unit of the guest. Rotaxane **5.3** displays the same spectroscopic features of the pseudorotaxane: an intense band in the UV at 260 nm with $\varepsilon = 73000$ M^{-1} cm^{-1} and a weak and broad band in the visible region of the spectrum, centred at 490 nm and with $\varepsilon = 670$ M^{-1} cm^{-1}. As reported above for calixarene **5.1**, the absorption coefficient of the main band in the UV is lower with respect to related rotaxanes bearing a tris-phenylureido calixarene as a macrocycle.[2,3]

The stability constant of the pseudorotaxane was determined upon titration of the host with the guest (figure 5.6, left). The absorbance changes, fitted according to a 1:1 binding model, provided a value of 3.2×10^6 M^{-1}. Indeed, this value is comparable with the one reported for similar compounds,[8] suggesting that the number of phenylurea moieties does not affect the stability of the pseudorotaxane. The dynamics of the threading process was investigated by stopped-flow kinetics. **DOV**$^{2+}$ and **5.1** were mixed in equimolar amounts and the absorption changes were followed in the UV and visible regions (figure 5.6, right). The kinetic traces were then fitted with a mixed order kinetics model (second-order threading, first-order dethreading), under the constraint that the ratio between the two kinetic constants must equal the equilibrium constant, determined upon titration. The rate constants for threading and dethreading resulted to be 3.4 × 10^3 M^{-1} s^{-1} and 1.1 × 10^{-3} s^{-1}, respectively. These values are three orders of magnitude lower with respect to the parent pseudorotaxane.[1,3] In the present case, the threading is likely to be slower due to the lack of one phenylurea, and this result would support the hypothesis that the phenylureido units are responsible for the stabilization of the transition state. Moreover, since, before the threading, the two counterions must leave the axle and bind to the phenylureido receptors, it is reasonable that when the calixarene is in the *alternate* conformation, *i.e.*, with the two phenylureas on the opposite rims, the threading process is disfavoured.

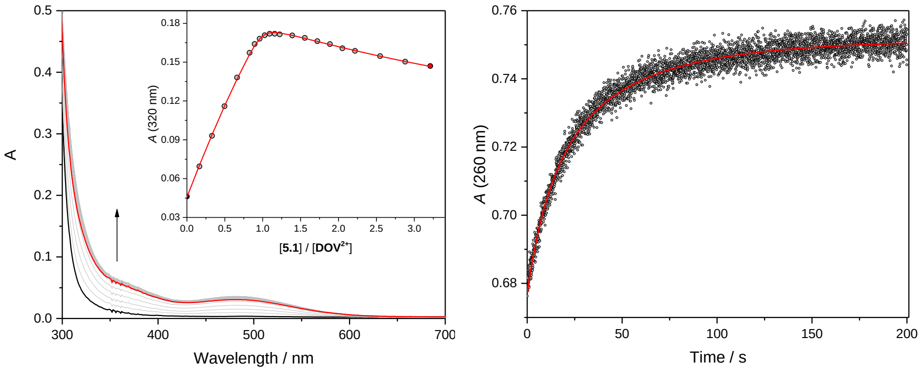

Figure 5.6: Left: Absorption spectra and absorbance variations at 320 nm (inset, fitting in red) upon titration of a 7.3 × 10^{-5} M solution of ***DOVTsO$_2$*** *with concentrated* ***5.1****; right: absorption changes at 260 nm upon rapid mixing of equimolar amounts at* ***DOVTsO$_2$*** *and* ***5.1****, with fitting (red). The concentrations of the two reactants after mixing is 1.3 × 10^{-5} M.*

As the electrochemical experiments were performed in the presence of a 100-fold excess of tetrabutylammonium hexafluorophosphate (TBAPF$_6$) (*vide infra*), spectrophotometric titrations were also performed in these experimental conditions. The obtained value of the stability constant is 7.0 × 10^4 M^{-1}, about 50-fold lower than in absence of the salt. An effect of the concentration and the nature of the anions on the stability of the pseudorotaxane is not unexpected, considering that the formation of the pseudorotaxane is in competition with the ion-pairing between the bipyridinium ion and its counteranions.[4,5]

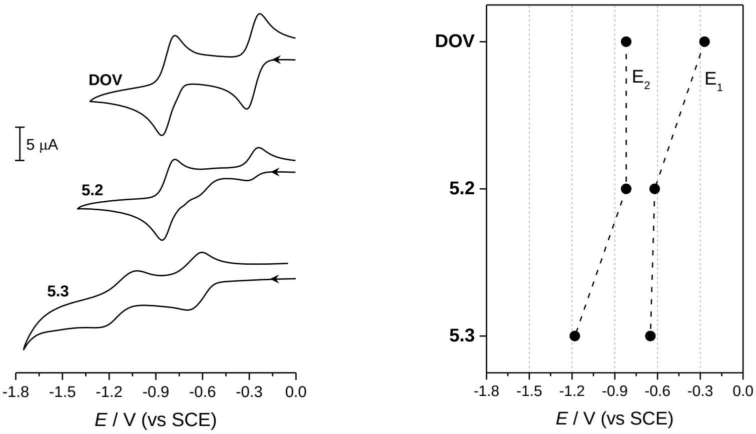

Figure 5.7: Cyclic voltammograms (left, c = 1-3 × 10^{-4} M, CH_2Cl_2, 100-fold $TBAPF_6$, scan rate 100 mV/s) and genetic diagram (right) for the first (E_1) and second (E_2) reduction of the bipyridinium in ***DOVTSO$_2$****,* ***5.2*** *and* ***5.3****.*

Electrochemical experiments on the molecular components and on the supramolecular systems were performed in dry CH_2Cl_2, in the presence of a 100-fold excess of $TBAPF_6$ as supporting electrolyte (figure 5.7). Calixarene **5.1** does not show any reversible process. As a model compound of the free bipyridinium moiety, which is the electroactive unit, electrochemical experiments were also performed on **DOVTsO$_2$.** The cyclic voltammetry (CV) of **DOV^{2+}** is characterized by two reversible monoelectronic waves at negative potentials, at $E_{1/2}' = - 0.27$ V and $E_{1/2}'' = - 0.83$ V. When the viologen is included in the cavity of a calix[6]arene macrocycle, the two processes are shifted to more negative potential values, on account of the host-guest electron transfer interactions (Figure 5.7).[2,3] Indeed, the cyclic voltammetric curves of rotaxane **5.3** display two quasi-reversible waves, with $E_{1/2}' = - 0.65$ V and $E_{1/2}'' = - 1.18$ V. As observed for related rotaxanes,[8] these processes are affected by slow heterogeneous electron-transfer kinetics. The pseudorotaxane **5.2**, obtained by mixing **5.1** and **DOVTsO$_2$** in equimolar amounts, shows the typical cyclic voltammetry curves described by an electrochemical process followed by a chemical reaction (EC square scheme, figure 5.8).[1,4,5] A fraction of free **DOV^{2+}** is still present in solution, as evidenced by the small cathodic process around - 0.3 V. This is not unexpected, due to the lower association constant in the presence of an excess of PF_6^- ions and to the effect of the ion pair dissociation on the formation of the complex.[6,7] Indeed, the intensity of this signal decreases on increasing the concentration of **5.1**. On the other hand, the first reduction of the bipyridinium occurs at - 0.65 V, as it is encapsulated in the calixarene, whereas the second reduction is displayed at - 0.83 V, as in the free **DOV^{2+}**. Upon re-oxidation, only the processes of free **DOV^{2+}** are observed, and this ultimately leads to a large separation between the cathodic and anodic peaks of the first process. Such a behaviour can be rationalized by means of an EC square scheme mechanism. The first reduction occurs when the bipyridinium is encircled by the calixarene, thus at the same potential as in the rotaxane. After the first reduction, the electronic interaction between the host and the guest is drastically reduced, and the system dethreads rapidly. As a result, the second reduction occurs on the free bipyridinium. When the potential is reversed, the first re-oxidation occurs on the free bipyridinium, but the threading of the radical-cation is slow, thus the second re-oxidation is observed at the same potential as for the free species as well.[1,4,5]

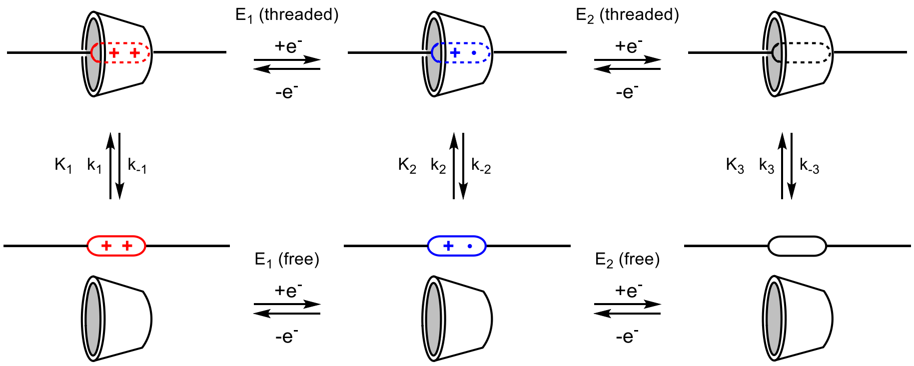

*Figure 5.8: EC square scheme for the assembly/disassembly (vertical processes) and redox processes (horizontal) of pseudorotaxane **5.3**.*

Therefore, in analogy with parent systems, pseudorotaxanes based on the **5.1** calixarene can be disassembled by electrochemical reduction of the bipyridinium axle. Indeed, the results of the electrochemical and spectroscopic investigations suggest that the two different conformers behave in a similar way and the *1,2,3-alternate* and the *cone* conformation assumed by the interlocked structure cannot be distinguished in our experimental conditions. On the other hand, UV-vis and electrochemical experiments evidenced the cardinal role played by the number, orientation and reciprocal arrangement of the phenylureidic groups in the threading mechanism and stability of interwoven structures.

5.3 Pseudorotaxanes and rotaxanes with scorpiand-like motifs

Compounds **5.4** and **5.5** (figure 5.9, top) were synthesized in the group of Prof. A. Arduini and Prof. A. Secchi (University of Parma), through a supramolecularly assisted reaction. This approach, already reported for similar systems[25–27], is based on the insertion of an anchoring group on the upper rim of the calixarene, which eventually reacts with one extremity of the axle threaded in the cavity. In this case, the calix[6]arene was synthesized with a methyl ester group on one phenylureido moiety. After the threading of a dihexyloxy-bipyridinium ditosylate salt, the anchoring group undergoes a transesterification process with the hydroxyl group of the thread that protrudes from the upper rim of the cavity, to yield the scorpionate [*c1*]**5.4**. The corresponding rotaxane [*c1*]**5.5** is eventually obtained by stoppering the remainder hydroxyl terminus with a diphenylacetate group. Interestingly, NMR experiments performed on solutions of **5.4** in non-polar solvents, with concentrations above 2×10^{-2} M, evidenced a notable amount of a [*c2*] dimeric species, *i.e.*, where two molecules of **5.4** interact by interpenetrating each other (figure 5.9, bottom).[10,11] Nevertheless, it was found out that, either in diluted (3×10^{-3} M) or in concentrated (3×10^{-2} M) solutions, the stoppering reaction occurred always on the [*c1*] form, suggesting that, indeed, this reaction is entropically driven.

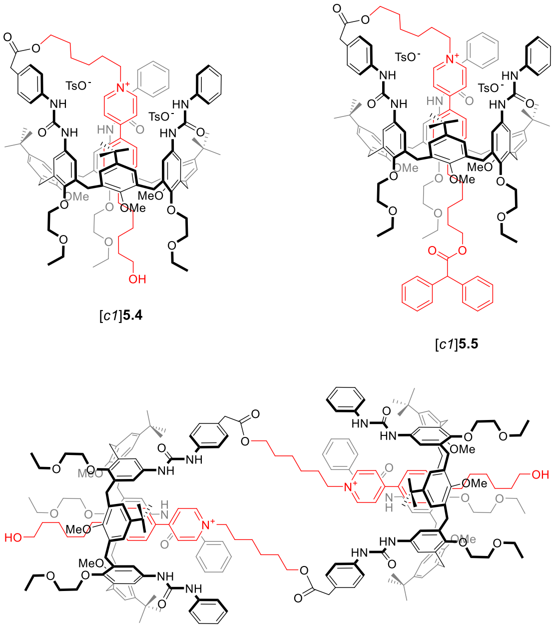

[*c1*]**5.4**

[*c1*]**5.5**

[*c2*]**5.4**

*Figure 5.9: Molecular structures of pseudorotaxanes [c1]**5.4** (top left) and [c2]**5.4** (bottom) and of rotaxane [c1]**5.5** (top right).*

UV-vis absorption spectra were recorded in CH_2Cl_2 and CH_3CN, at concentrations around 2×10^{-4} M, to assure that the intramolecular self-threaded form [*c1*]**5.4** is the only species present in solution. The spectra are similar in both solvents, as observed in related systems,[2,4] and are characterized by a main absorption band in the UV, centred between 257 and 260 nm and with a molar absorption coefficient close to 9×10^5 M^{-1} cm^{-1}. A weaker and broader CT band around 460 nm, with $\varepsilon = 500$ M^{-1} cm^{-1}, is indicative of the encapsulation of viologen unit inside the macrocycle (figure 5.10). The similarity of the spectra of [*c1*]**5.4** in the two solvents suggests a high stability, *i.e.*, a high ratio between the threaded and dethreaded complex, regardless of the solvent.[1,4]

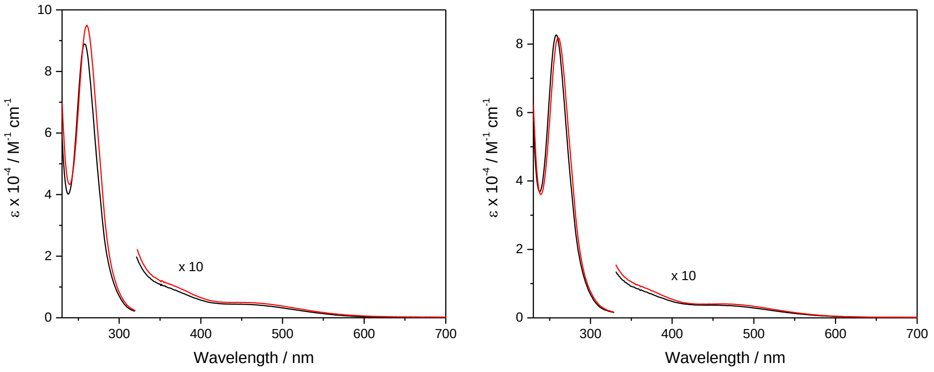

Figure 5.10: Absorption spectra of ***5.4*** *(left) and* ***5.5*** *(right) in CH_3CN (black) and CH_2Cl_2 (red).*

The electrochemical investigations were performed using cyclic voltammetry and differential pulse voltammetry (DPV) on CH_2Cl_2 and CH_3CN solutions of **5.4** and **5.5**, at concentrations around 2×10^{-4} M. The results of the electrochemical experiments are reported in table 5.1 and figure 5.11. As in the previous case, **DOVTsO$_2$** was taken as a model of the free bipyridinium electroactive unit. The [*c1*]rotaxane **5.5** displays the typical electrochemical behaviour of related [2]rotaxanes:[2,3,5] the two reduction waves of the bipyridinium moiety are shifted to more negative values (table 5.1), on account of the CT interaction between the host and the guest, and regardless of the solvent.[8,21,22] The electrochemical features of [*c1*]**5.4** are different with respect to **5.5**, on account of the fact that the bipyridinium unit can dethread from the macrocycle, and they are solvent dependent.

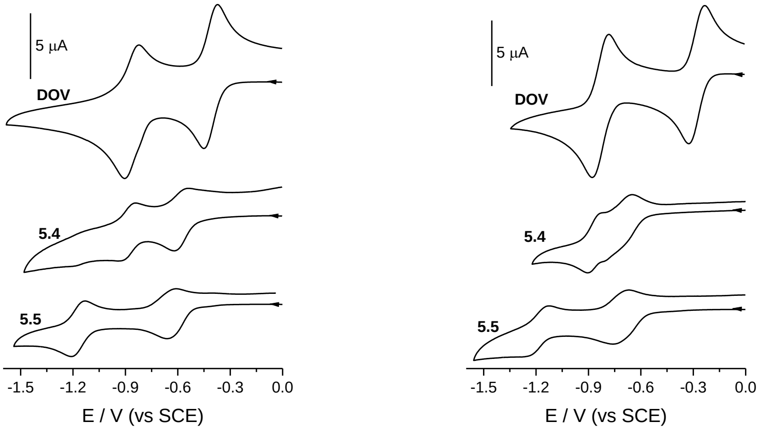

Figure 5.11: CV curves in CH_3CN (left) and CH_2Cl_2 (right) of ***DOVTsO$_2$*** *($c = 2.4 \times 10^{-4}$ M in CH_3CN and 3.0×10^{-4} M in CH_2Cl_2), [c1]**5.4** ($c = 1.5 \times 10^{-4}$ M) and [1]rotaxane **5.5** ($c = 1.8 \times 10^{-4}$ M). Scan rate 100 mV/s, 100-fold excess of $TBAPF_6$.*

In CH_3CN the first reduction occurs at a potential about 0.2 V more negative than in the corresponding free axle.[28] The second reduction process occurs at the same potential of the free **DOV^{2+}**, but a minor wave is still present at - 1.2 V, which can be ascribed to the encapsulated axle.[2,3] In CH_2Cl_2, the two voltammetric waves of the bipyridinium unit occur at E_1 = - 0.65 V and E_2 = - 0.86 V. The second reduction process is less negative than the corresponding process in rotaxane **5.5**, but it is also slightly more negative (0.04 V) than the corresponding process in free axle. This value would suggest that the radical cation of the bipyridinium unit is not engulfed anymore inside the calixarene, but the latter still exerts some influence on the bipyridinium axle. It must be remarked that both in **5.4** and **5.5**, the two voltammetric waves are quasi-reversible and separation between the anodic and cathodic peak is larger than 0.1 V. Moreover, on increasing the scan rate, the first process is largely affected: the two peaks move far apart, and a second anodic peak appears, at more positive potential values, close to the free bipyridinium in solution.

	CH_3CN		CH_2Cl_2	
Compound	**E_1 / V vs SCE**	**E_2 / V vs SCE**	**E_1 / V vs SCE**	**E_2 / V vs SCE**
$DOVTsO_2$	-0.41	-0.87	-0.27	-0.82
5.4	-0.60	-0.88	-0.65 [a]	-0.86
5.5	-0.63	-1.18	-0.72	-1.20

*Table 5.1: Reduction potentials vs SCE for the first (E_1) and second (E_2) processes of the bipyridinium unit in **$DOVTsO_2$**, **5.4** and **5.5**. [a] value obtained from DPV.*

Digital simulations of the CV curves were carried out in order to elucidate the kinetics and thermodynamics of the threading and dethreading processes. The voltammetric curves were simulated with the mechanism reported in the EC square scheme reported in figure 5.12, by fixing the values of the reduction potentials E_1 and E_2 of the free and threaded species to the ones of **DOV^{2+}** and **5.5**, respectively. The results of the simulation were compared with the experimental data in CH_3CN for a selected scan rate. The stability constant for the threading of the dicationic species is around 10^3 M^{-1}, and the threading process is fast, with a rate constant $k_1 > 5 \times 10^4$ s^{-1}. On the other hand, the kinetics of the radical cation species are slow (k_2 around 1 s^{-1}, and k_{-2} around 5 s^{-1}), and these values confirm that part of the complexes are still in the self-threaded form after the second reduction. The experimental data do not allow any remark on the kinetics of the processes associated with the neutral species.

Simulation of the experiments performed in CH_2Cl_2 is less straightforward. The cyclic voltammetric curves of [*c1*]**5.4** in CH_2Cl_2 cannot be reproduced by the simulation experiments if **DOV^{2+}** and **5.5** are taken as model compounds for the free and encapsulated electroactive moiety, respectively. Indeed, the value of the second quasi-reversible reduction potential cannot be ascribed neither to the free nor to the encapsulated species. The large positive shift with respect to **5.5** would suggest that the radical cation is not encapsulated anymore inside the cavity of the calixarene; nevertheless, the small negative shift with respect to **DOV^{2+}** would suggest that the monoreduced axle is still affected by the close proximity of the wheel.

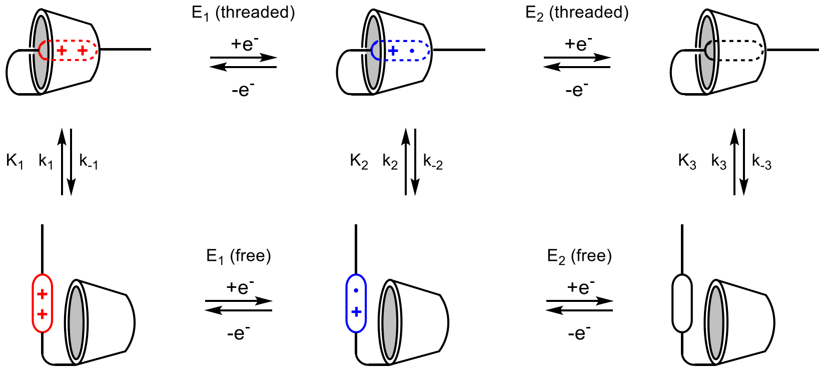

*Figure 5.12: EC square scheme of the threading/dethreading equilibria (horizontal processes) and the redox reactions (vertical processes) of compound [c1]**5.4**.*

In the absence of an adequate model compound, only qualitative considerations can be made, based on the shape of the CV curves. In analogy with the results obtained in CH_3CN, a large association constant of the dicationic complex can be inferred. On the basis of the position and relative separation of the peaks of the first reduction wave, the complex should be even more stable, with a stability constant larger than 10^4 M^{-1}. On the other hand, the values of k_2 and k_{-2} can be modelled on the basis of two experimental observations: i) after the first reduction there is no residual signal of the encapsulated axle and ii) the anodic peak of the monoreduced axle splits in two signals on increasing the scan rate. The first observation implies faster kinetics for the monoreduced bipyridinium (k_2 and k_{-2}) with respect to the corresponding processes in CH_3CN. The second observation would suggest that at relatively slow scan rates the equilibrium between free and complexed monoreduced species is fast enough and a quasi-reversible process is observed, whereas on increasing the scan rate some free monoreduced axle is present. A qualitative simulation suggests that the value for k_2 and k_{-2} could be one or two orders of magnitude larger than in CH_3CN.

Nevertheless, in both solvents, the shift of the first reduction process to more negative potential values with respect to the free **DOV^{2+}** confirms that the electroactive unit is encapsulated in the cavity of the calixarene and involved in charge-transfer interactions. In the scorpionate **5.4**, upon reduction, this interaction is weakened and, as already mentioned, it prompts the dethreading of the supramolecular adduct.

5.4 Conclusion and perspectives

Two new geometries for calix[6]arene-viologen supramolecular systems were studied. Calixarene **5.1**, bearing two phenylureido moieties on the upper rim of the cavity, can assume one *cone* and two *alternate* conformations, which are retained in the corresponding pseudorotaxane and rotaxane formed with a viologen salt, resulting in two different co-conformations of the supermolecules. UV-vis experiments evidenced that the lack of one phenylureido group and the opposite position of the two groups in the *alternate* conformation lead both to a slower threading and to a lower stability constant of the threaded complex. These results are in line with previous studies,[8] which had proven that the phenylureido moieties bind the counterion of the guest and stabilize the transition state of the threading process. Electrochemical investigations evidenced the typical behaviour of similar supramolecular structures: upon reduction, the system disassembles and re-assembles upon re-oxidation.[1,2] These preliminary studies disclose new perspectives on the ability of **5.1** to yield interlocked structures with different spatial orientations of the host and with unusual mechanostereochemical properties.[20] Moreover, the covalent linking between calixarene wheels in the *alternate* conformation can eventually lead to polyrotaxane structures behaving as tubular hosts for polybipyridinium-based threads. Self-threaded structures **5.3** and **5.4**, with a scorpiand-like structure, were also studied. Even in this case, the system can be assembled/disassembled upon electrical stimuli. Therefore, they represent a valid building block for the realization of high-complexity molecular devices. In particular, the peculiar hermaphroditic structure of **5.4**, and its ability to form dimers, can constitute the basis for novel redox-activated molecular muscles, in line with the already reported devices based on daisy-chain motifs.[16] Indeed, in a [*c*2] dimer where each of the two thread consists in two bipyridinium stations with different affinity for the calixarene and different reduction potential, a redox input can induce the extension/contraction of the entire supermolecule. Moreover, the dimeric form can be exploited as a templating strategy to bring the two calixarenes to a proper distance, in order to allow a covalent linking and ultimately the formation of a supramolecular cage able to host poly-bipyridinium threads.

5.5 References

1. L. Mandolini and R. Ungaro, Eds., *Calixarenes in Action*, Imperial College Press, London, **2000**.
2. Z. Asfari, V. Bohmer, J. Harrowfield, and J. Vicens, Eds., *Calixarenes 2001,* Kluwer, Dordrecht, **2001**.
3. J. W. Steed and J. L. Atwood, *Supramolecular Chemistry*, 2nd ed., Wiley, **2009**.
4. A. Arduini, R. Ferdani, A. Pochini, A. Secchi, and F. Ugozzoli, *Angew. Chem. Int. Ed.*, **2000**, *39*, 19, 3453–3456.
5. A. J. Evans, S. E. Matthews, A. R. Cowley, and P. D. Beer, *J. Chem. Soc. Dalt. Trans.*, **2003**, *3*, 24, 4644–4650.
6. L. Pescatori, A. Arduini, A. Pochini, F. Ugozzoli, and A. Secchi, *Eur. J. Org. Chem.*, **2008**, *2008*, 1, 109–120.
7. V. Amendola, L. Fabbrizzi, and L. Mosca, *Chem. Soc. Rev.*, **2010**, *39*, 10, 3889–3915.
8. A. Credi, S. Dumas, S. Silvi, *et al.*, *J. Org. Chem.*, **2004**, *69*, 18, 5881–5887.
9. F. Huang, J. W. Jones, C. Slebodnick, and H. W. Gibson, *J. Am. Chem. Soc.*, **2003**, *125*, 47, 14458–14464.
10. J. W. Jones and H. W. Gibson, *J. Am. Chem. Soc.*, **2003**, *125*, 23, 7001–7004.

11. A. Arduini, F. Calzavacca, A. Pochini, and A. Secchi, *Chem. Eur. J.*, **2003**, *9*, 3, 793–799.

12. A. Arduini, R. Bussolati, A. Credi, *et al.*, *J. Am. Chem. Soc.*, **2013**, *135*, 26, 9924–9930.

13. J. F. Stoddart, *Acc. Chem. Res.*, **2001**, *34*, 6, 410–411.

14. J.-P. Sauvage and C. O. Dietrich-Buchecker, Eds., *Molecular Catenanes, Rotaxanes and Knots*, Wiley-VCH, **1999**.

15. V. Balzani, A. Credi, and M. Venturi, *Molecular Devices and Machines– A Journey into the Nano World*, Wiley-VCH, Weinheim, **2004**.

16. C. J. Bruns and J. F. Stoddart, *Acc. Chem. Res.*, **2014**, *47*, 7, 2186–2199.

17. V. Zanichelli, M. Bazzoni, A. Arduini, *et al.*, *Chem. Eur. J.*, **2018**, *24*, 47, 12370–12382.

18. V. Zanichelli, L. Dallacasagrande, A. Arduini, *et al.*, *Molecules*, **2018**, *23*, 5, 1156.

19. M. Bazzoni, V. Zanichelli, L. Casimiro, *et al.*, *Eur. J. Org. Chem.*, **2019**, 21, 3513–3524.

20. J. F. Stoddart, *Chem. Soc. Rev.*, **2009**, *38*, 6, 1802–1820.

21. A. Arduini, R. Bussolati, A. Credi, *et al.*, *Tetrahedron*, **2008**, *64*, 36, 8279–8286.

22. V. Zanichelli, G. Ragazzon, A. Arduini, *et al.*, *Eur. J. Org. Chem.*, **2016**, 5, 1033–1042.

23. A. J. Bard and L. R. Faulkner, *Electrochemical Methods: Fundamentals and Applications*, 2nd ed., John Wiley & Sons, Ltd, **2000**.

24. A. E. Kaifer, *Supramolecular Electrochemistry*. John Wiley & Sons, Ltd, **2000**.

25. J.-N. Rebilly, A. Hessani, B. Colasson, and O. Reinaud, *Org. Biomol. Chem.*, **2014**, *12*, 39, 7780–7785.

26. N. L. Strutt, H. Zhang, M. A. Giesener, J. Lei, and J. F. Stoddart, *Chem. Commun.*, **2012**, *48*, 11, 1647–1649.

27. J. Rotzler, S. Drayss, O. Hampe, D. Häussinger, and M. Mayor, *Chem. Eur. J.*, **2013**, *19*, 6, 2089–2101.

28. R. Ballardini, A. Credi, M. T. Gandolfi, *et al.*, *Inorg. Chim. Acta*, **2007**, *360*, 3, 1072–1082.

Conclusion

Conclusion

New examples of light- and electro- responsive molecular and supramolecular devices and machines were investigated. The major part of the work was devoted to the characterization of new axles for the supramolecular pump reported by Credi et al. in 2015,[1] in order to improve the efficiency of the system. Photochemical and supramolecular characterizations, supported by kinetic simulations were conducted on a series of molecular axles bearing a different functionalization from the already reported compounds either on the azobenzene, on the pseudostopper or on the position of the linker between the ammonium recognition site and the azobenzene. Eventually, the dissipative behaviour under continuous irradiation of one novel prototype of molecular pump was demonstrated via NMR techniques.

Parallel studies on photochromic pseudorotaxanes and on azobenzenze-C_{60} bisadducts were devoted to elucidate the molecular and supramolecular effects on photochromism. In the first case, it was found out that the poor thermal stability of the closed form of imidazolium-based terarylenes, obtained upon UV irradiation, can be improved in pseudorotaxanes formed with crown ethers. In the case of azobenzene-fullerene bisadducts, the configuration of the azobenzene moiety is dictated by the regiochemistry of the reaction, giving rise either to an inverted photochromism, *i.e.*, a thermodynamically stable *Z* isomer, or to a locking of the photochromism in the *E* form. A parallel study, conducted during the research stay at the ENS Paris – Saclay, was focused on the photochemical investigation of the unravelled *E*/*Z* isomerization of the central double bond of DCM (dicyanomethylenepyran) single and multi-component derivatives.

The second part of the work concerned the study of supramolecular structures behaving as electro-activated molecular devices. New hosts and new geometrical arrangements of calixarene-viologen interlocked structures, namely rotaxanes and pseudorotaxanes based on a new diphenylureido-calix[6]arene and dialkylviologen salts, and self-complexed [*c1*] rotaxanes and pseudorotaxanes were characterized. Ultimately, this research explored new frontiers of smart functional molecular devices and increased the knowledge on the chemical and energetic requirements of their molecular components.

References

1 G. Ragazzon, M. Baroncini, S. Silvi, M. Venturi, and A. Credi, *Nat. Nanotech.*, **2015**, *10*, 70–75.

Experimental section

Experimental section

1. Compounds and solvents

Compounds **1.1-1.14**H$^+$ and **DN24C8** were synthesized and characterized via NMR in the research group by Dr. Jessica Groppi and Dr. Marcello La Rosa. Compounds **2.1-2.3** and their corresponding protonated forms were synthesized and characterized via NMR and XRD in the research group of Stephen Loeb (University of Windsor, Canada) by Dr. Giorgio Baggi. Compounds **3.1-3.5** were synthesized and characterized via NMR and XRD in the group of Maurizio Prato (University of Trieste, Italy) by Dr. Luka Dordevic. Compounds **4.1-4.4** were synthesized and characterized via NMR in the group of Dr. Rémi Métivier and Prof. Juan Xie (ENS - University of Paris-Saclay) by Dr. Stéphane Maisonneuve. Compounds **5.1-5.5** were synthesized and characterized via NMR in the research group of Prof. Arturo Arduini and Prof. Andrea Secchi by Margherita Bazzoni. Crown ethers **24C8** and **DB24C8** were purchased from Sigma Aldrich or TCI, and used without any further purification. Spectroscopic analyses were conducted in spectroscopic grade CH_2Cl_2, CH_3CN (Uvasol) and in distilled toluene (Sigma Aldrich). Electrochemical measurements were performed in dry CH_2Cl_2 and CH_3CN (Sigma Aldrich). Triflic acid (TfOH) and tetrabutylammonium hexafluorophosphate ($TBAPF_6$), were purchased from Sigma Aldrich. Tributylamine (TBA) was purchased from Fluka. Solutions of photochromic compounds were kept in dark conditions.

2. Absorption and luminescence spectroscopy

Absorption spectra were recorded on Cary 5000, Cary 4000 and Cary 300 (Varian - Agilent), lambda750, lambda650 and lambda40 (Perkin Elmer) double beam spectrophotometers, and Cary 50 Bio single beam spectrophotometer. In case of fast processes experiments, a diode array

Avantes coupled to a Hg-lamp was used. 1 cm pathlength quartz cuvettes (Hellma, Starna) were implied. In case of high absorption solutions, 1 mm or 2 mm pathlength cuvettes were used as well. Luminescence spectra were recorded on Cary Eclipse (Varian), FLS980 (Edinburgh), FluoroLog-3 or FluoroMax-3 (Jobin Yvon). Fluorescence decays were measured by the time-correlated single-photon counting (TCSPC) technique on FLS980 (Edinburgh) using a photodiode laser as a source of excitation.

Time resolved spectroscopic measurements at ENS Paris-Saclay were performed with a femtosecond Titanium:Sapphire laser (Tsunami, Spectra-Physics) pumped by a doubled Nd:YVO_4 laser (Millennia Xs from Spectra-Physics). Light pulses at 800 nm from the oscillator were selected by an acousto-optic crystal at a repetition rate of 4 MHz, and then doubled at 400 nm by non-linear crystals. Fluorescence photons were detected at 90°, through a polarizer at the magic angle, by means of a Hamamatsu MCP R3809U photomultiplier, connected to a SPC-630 TCSPC module from Becker & Hickl. The instrumental response function was recorded before each decay measurement with a FWHM (full width at half-maximum) of 23 ps. The fluorescence data were analyzed using the Globals software package developed by the Laboratory for Fluorescence Dynamics at the University of Illinois at Urbana-Champaign, which includes reconvolution analysis and the global non-linear least-squares minimization method.

Emission quantum yields were measured by comparing the integrated emission spectra of the sample with a suitable standard, according to the formula

$$\Phi = \Phi_S \times \frac{A_S}{A} \times \frac{I}{I_S} \times \frac{n^2}{n_S^2} \qquad (E1)$$

where the subscript "s" indicates the standard, A is the absorbance at the excitation wavelength, I the integrated emission value and n the refractive index of the solvent. In order to avoid any correction, an isosbestic point was chosen as excitation wavelength. Quinine sulphate in H_2SO_4 0.05 M (Φ_{em}=0.53)[1] and Coumarine 153 in EtOH (Φ_{em}=0.544)[2] were used as standards.

Lippert-Mataga plots[3] were obtained correlating the energies of the Stokes shifts (ν_{abs}- ν_{em}) with the parameter Δf, calculated from the solvent properties (refraction index n, dielectric constant ε_s), according to the equation:

$$\Delta f = \frac{\varepsilon_s - 1}{2\varepsilon_s + 1} - \frac{n^2 - 1}{2n^2 + 1} \qquad (E2)$$

The resulting plot is a straight line, whose slope m is related to the difference in the dipole moment $\Delta\mu$, through the equation:

$$\Delta\mu = \mu_{exc} - \mu_{gr} = 0.01 \times \sqrt{m \times a^3} \qquad (E3)$$

where a represents the radius in Å of the Onsager spherical cavity. In the present cases, a was approximated to the half of the length of the major axis of the molecule.[3]

Mauser plots[4–6] were employed in the analysis of kinetic and photokinetic processes, to determine how many kinetically independent reactions occur. According to this method, the absorbance evolutions at two arbitrary wavelengths at different times are plotted versus one another. If the resulting plot is linear, then only one reaction takes place, whereas if the plot deviates from linearity more than one reaction occur. In this latter case, a second plot can be obtained by dividing both the absorbances by the absorbance at a third wavelength. If the resulting plot is linear, then two independent kinetics are present, if not more than two. This method can be iterated several times, despite from the third level the scattering of the values results in a severe aberration of the plot.

3. Spectroscopic titrations and kinetics

Spectroscopic titrations were conducted by adding small amounts (1-500 μL) of a concentrated solution of a species to a more diluted solutions of the other species and recording the corresponding absorption spectrum after equilibrium was achieved. Obtained data were then fitted with software SPECFIT,[7] which allows a global analysis of the spectra and provides the corresponding thermodynamic constant related to the process.

Thermal back isomerization kinetics were investigated monitoring the absorbance changes over time in the dark. The obtained data were fitted according to a first order model with software SPECFIT.[7]

In the case of threading of supramolecular species, kinetics were measured monitoring the absorption or emission variations over time after the mixing of two equimolar solutions of the two partners in a dedicated tandem cuvette (which comprises two compartments separated by a wall with a hole for the mixing) or after the addiction of a concentrated solution of one component to a more diluted solution of the other, in order to obtain the desired stoichiometric ratio.

Fast threading kinetics (timescales below tens of seconds) were investigated on air-equilibrated solutions at room temperature using a stopped-flow spectrophotometer equipped with a 1 cm pathlength cell and a driving ram for the mixing system at the N_2 pressure of 8.5 bar. Under these conditions, the time required to fill the cell is lower than 2 ms. The data obtained were fitting with software SPECFIT with a mixed order reaction (second order for threading, first order for dethreading), with the constrain that the ratio between the two constants should equal the thermodynamic constant obtained from titrations.

4. Irradiation conditions

Irradiation experiments were performed on air-equilibrated solutions, thoroughly stirred, at room temperature. HanauQ400 mercury medium pressure lamps (150 W, 125 W) were used. The desired wavelength of irradiation was selected using an appropriate interference filter. The incident photon flux of the mercury lamp (q_0) was measured by means of the ferrioxalate actinometer, according to the procedure reported for its "microversion".[1] Solution of ferrioxalate were irradiated at the desired wavelength, then an excess of *1,10*-phenantroline was added to give complete complexation of the free Fe^{2+} ions. The absorbance values were taken at 510 nm, on the maximum of the $Fe(phen)_3^{2+}$ complex. To avoid the contribution of the thermal release of Fe^{2+}, the absorbance at 510 nm of a non-irradiated solution with phenantroline was recorded and substracted from the irradiated ones. The photon flux is eventually obtained from the equation:

$$q_0 = \frac{\Delta A_{(510\ nm)} \cdot Y}{f \cdot \Delta t} \qquad (E4)$$

Where ΔA is the difference between the absorption of the irradiated and non-irradiated solutions, Y is a constant given for each mercury line, comprehensive of the quantum yield, the volumes and the absorption coefficients, and f is the fraction of absorbed light, linked to the absorbance by the equation

$$f = 1 - 10^{-A} \qquad (E5)$$

In the total absorption regime, *i.e.*, when the absorbance exceeds 2, the exponential term can be neglected and thus $f = 1$. Since the ferrioxalate solution is in the total absorption regime up to 405 nm, the correction for the fraction of absorbed light was considered only in the case of 436 nm irradiations.

Irradiation experiments reported in Chapter 4 were performed at room temperature, on vacuum-deoxygenated solutions. Hamamatsu Hg-Xe lamps LC8 or LC6 – Lightningcure (200 W) were employed as excitation source. The desired wavelengths were selected using appropriate Semrock or Oriel interferential filters. The incident lamp power was measured by means of an Ophir PD300-UV photodiode. NIR contribution was measured and substracted from the total value. Photoisomerization quantum yields and fatigue resistances were determined using a home-made setup, that allows to collect absorption spectra with high rates, under continuous irradiation. A Xenon lamp (75 W) was used as a probing light source, and a Hg/Xe lamp, placed at 90° with respect to the incident beam, was used to induce the photochromic reaction in the sample, placed in a cuvette and thoroughly stirred. Spectra were recorded every 0.2 seconds, with a spectrometer coupled with a CCD (Roper Scientific and Princeton Instruments, respectively).

5. Determination of the absorption spectrum of metastable isomers

For azobenzene derivatives, the absorption spectrum of the *Z-* isomer was obtained mathematically, according to the method reported by E. Fischer in 1967.[8] Let *1* and *2* be two photostationary states obtained upon irradiation at two different wavelengths λ_1 and λ_2. Given the assumption that the ratio of the forward and backward quantum yield is independent of the irradiation wavelength, the ratio between the two photoconversions α_1 and α_2 equals the ratio between the absorbance variations (with respect to the initial spectrum of the pure *E-* form) at a wavelength λ_x chosen where this variation is maximized.

$$n = \frac{\alpha_1}{\alpha_2} = \frac{\Delta \mathrm{A}_{1,\lambda x}}{\Delta \mathrm{A}_{2,\lambda x}} \qquad (E6)$$

The photoconversion at the second photostationary state, α_2 is eventually obtained by the equation *E7*:

$$\alpha_2 = \frac{\left(\frac{\Delta \mathrm{A}}{\mathrm{A}}_{\lambda 1} - \frac{\Delta A}{\mathrm{A}}_{\lambda 2}\right)}{\left[1 + \frac{\Delta \mathrm{A}}{\mathrm{A}}_{\lambda 1} - n\left(1 + \frac{\Delta A}{\mathrm{A}}_{\lambda 2}\right)\right]} \qquad (E7)$$

where $\frac{\Delta A}{\mathrm{A}}_{\lambda 2}$ and $\frac{\Delta A}{\mathrm{A}}_{\lambda 2}$ are the relative absorbance variation at the corresponding irradiation wavelength with respect to the initial spectrum. Once the photoconversion is known, the absorption spectrum can be obtained by substraction from the photostationary state.

For terarylene derivatives, which showed a very fast thermal back isomerization, the absorption spectrum of the closed isomer was estimated from the luminescence spectrum. Since the open isomer is the only emissive form in the visible region, in a mixture open/closed the emission intensity is proportional of the amount of open isomer present in solution. To avoid aberrations due to the fast back isomerization, two cuvettes were irradiated for the same time interval. The first cuvette was used to record the absorption spectrum and the second to record the emission spectrum. The ratio between the final and the initial emission intensity represents the percentage of open isomer, thus the photoconversion is the reminder percentage. As in the previous case, the absorption spectrum of the pure closed isomer was obtained from the absorption spectrum of the irradiated mixture.

6. Quantum yield calculations

For a general photoreaction

$$\mathrm{R} \underset{h\nu_2,\,\Delta}{\overset{h\nu_1}{\rightleftarrows}} \mathrm{P}$$

where both the forms are photoactive, the photokinetics is described by equation (*E6*)[9]*:*

$$\frac{d[R]}{dt} = -\frac{d[P]}{dt} = -\frac{\Phi_{RP}\cdot q_0}{V}\cdot\frac{\varepsilon_{R,\lambda_i}\cdot[R]\cdot f}{(\varepsilon_{R,\lambda_i}\cdot[P]+\varepsilon_{P,\lambda_i}\cdot[Z])} + \frac{\Phi_{PR}\cdot q_0}{V}\cdot\frac{\varepsilon_{P,\lambda_i}\cdot[P]\cdot f}{(\varepsilon_{R,\lambda_i}\cdot[R]+\varepsilon_{P,\lambda_i}\cdot[P])} + k_\Delta\cdot[P] \qquad (E8)$$

where Φ_{RP} and Φ_{PR} represent the quantum yields of *R-P* and *P-R* isomerization, respectively, ε_{λ_i} are the absorption coefficients of *R* and *P* at the irradiation wavelength λ_i, f is the fraction of absorbed light calculated from the absorbance of the mixture at the irradiation wavelength λ_i

$$f = 1 - 10^{-A_{\lambda_i}} = 1 - 10^{-(\varepsilon_{R,\lambda_i}\cdot[R]+\varepsilon_{P,\lambda_i}\cdot[P])} \qquad (E9)$$

and $k_\Delta\cdot[P]$ is the contribution of the thermal process (the optical path of the cuvette is considered 1 cm and henceforth it will be omitted for clarity). It should be noted that, in this equation, *f* represents the absorbed light fraction, whereas the ratio between the absorption coefficients and the concentrations represents the contribution of each isomer to the absorbed light, *i.e.*, how the light is distributed between the two isomers. It is worth to remark also that both the concentrations and the absorbances are time-dependent.

Photoisomerization quantum yields were calculated through fitting of the absorbance values over time, using either the software Berkeley Madonna[10] or with a numerical iterative fitting method, implemented in an Igor procedure (Wavemetrics). In any case the software fitted the absorbance values at the irradiation light to compute the fraction of absorbed light and the concentrations. Another set of absorbances, at a wavelength with a larger variation, was added to the fit to minimize the error. The parameters to be optimized were Φ_{RP} and Φ_{PR} and the absorption coefficients of the *P* form, considering that a better fitting can be provided by minor adjustments on these values, that fall inside the error due the mathematical treatment to obtain the *P* spectrum.

7. Electrochemical methods

Cyclic voltammetry (CV) and differential pulse voltammetry (DPV) experiments were carried out in argon-purged dry solvents with an Autolab 30 multipurpose instrument interfaced to a PC. The working electrode was either a glassy carbon electrode (Amel, diameter 3 mm) or a Pt (Amel, diameter 1 mm) carefully polished with an alumina-water slurry on a felt surface, immediately before use. A Pt, separated from the solution by a frit, was employed as counter electrode, whereas an Ag wire was used as a quasi-reference electrode. Ferrocene or decamethylferrocene was added as an internal standard. The supporting electrolyte was added in a 100-fold proportion with respect to the sample concentration. Cyclic voltammograms were obtained at sweep rates varying from 0.05 to 5 V s^{-1}. Differential pulse voltammograms were recorded with a rate of 0.02 V s^{-1} and a peak height of 0.075 V. The IR compensation implemented within the software was employed to minimize the resistance of the solution. In any instance, the full electrochemical reversibility of the voltammetric wave of ferrocene was taken as an indicator of the absence of uncompensated resistance effects.

8. Separation methods

High-performance liquid chromatography (HPLC) analyses on compound **4.1** were performed on previously irradiated solutions, with an analytical HPLC chain from Shimadzu Prominence UFLC, equipped with two LC-20AD pumping modules, a CTO-20AC oven, a thermostatically controlled SPD-M20A module, a photodiode array (190-800 nm) for UV-Vis detection, and a CBM-20A communication module. The injection was carried out using a 5μL injection loop and a Rheodyne 7725i valve. The separation was carried out at 40°C using a C-18 grafted silica chromatographic column, Phenomenex Kinetex Evo-C18 column (particle size 5 μm, pores size 100 Å, length 250 mm, internal diameter 4.6 mm). The eluent mixture was MeOH:H_2O 75:25, with a flow rate between 1.5 mL/min (pressure 161 bar) and 2 mL/min (pressure 201 bar). The amount of the two isomers was determined from the integer of the elution peaks displayed at the isosbestic point (i.e. 396 nm) determined for the eluting solvent. The data were acquired with the LabSolutions V 5.71 SP2 software from Shimadzu Corporation.

Large scale separation of the two isomers was performed with a Teledyne CombiFlash Rf+ equipped of a photodiode array for UV-Vis absorption and a gradient pump for the eluent mixture. A 120 g RediSep Rf silica column chromatography cartridge was used.

9. References

1. M. Montalti, A. Credi, L. Prodi, and M. T. Gandolfi, *Handbook of Photochemistry*, 3rd ed, CRC Press, Boca Raton, **2006**.
2. K. Rurack and M. Spieles, *Anal. Chem.*, **2011**, *83*, 4, 1232–1242.
3. M. Meyer and J. C. Mialocq, *Opt. Commun.*, **1987**, *64*, 3, 264–268.
4. H. Mauser, *Z. Naturfosch*, **1968**, *23b*, 1025–1030.
5. H. Mauser, *Formale Kinetik*, Bertelsmann Universitatsverlag, Dusseldorf, **1974**.
6. H. Rau, *Photoisomerization of Azobenzenes*, in *Photoreactive Organic Thin Films*, Z. Sekkat and W. Knoll, Eds. Academic Press, San Diego, **2002**, 3–47.
7. R. A. Binstead, *SPECFIT*, Spectrum Software Associates, Chapel Hill, USA, **1996**.
8. E. Fischer, *J. Phys. Chem.*, **1967**, *71*, 11, 3704–3706.
9. K. Stranius and K. Börjesson, *Sci. Rep.*, **2017**, *7*, 41145.
10. *https://berkeley-madonna.myshopify.com*.

Appendix

Appendix A.

Dimethylazobenzene as a chemical actinometer

Chemical actinometers are widely employed by photochemists in the measurement of the photon flux of a light source, essential for quantitative analysis on photoreactions. Azobenzene[1,2] has been extensively used as an actinometer,[3] due to its high performances and good fatigue resistance. However, it shows not complete photoconversion upon UV irradiation, and the spectrum of the pure *Z* isomer cannot be easily obtained.[4] Herewith the photochemical characterization of a *p,p′*-dimethylazobenzene (**ABMe$_2$**, figure A1 left), displaying a clear and efficient *E*-*Z* isomerization, approaching total conversion at 365 nm, will be reported. This compound can be used as a chemical actinometer for the UV and visible region up to 436 nm, with easiness of handling and data treatment.

Absorption spectra were recorded in air-equilibrated acetonitrile (MeCN) solutions at room temperature. The molar absorption coefficient (ε) of *E*-**ABMe$_2$** was obtained through several measurements on fresh solutions. The absorption spectrum of *E*-**ABMe$_2$** in MeCN (figure A1, right) shows the typical two bands of azobenzene derivatives: a high-absorbing band centred at 332 nm and with an ε of 23900 M^{-1} cm^{-1}, attributed to the π-π* transition, and a low-absorbing band, centred at 430 nm and with an ε of 900 M^{-1} cm^{-1}, that corresponds to the forbidden n-π* transition. These two bands are both well resolved and smooth, as it is expected from an azobenzene-type.[1,2]

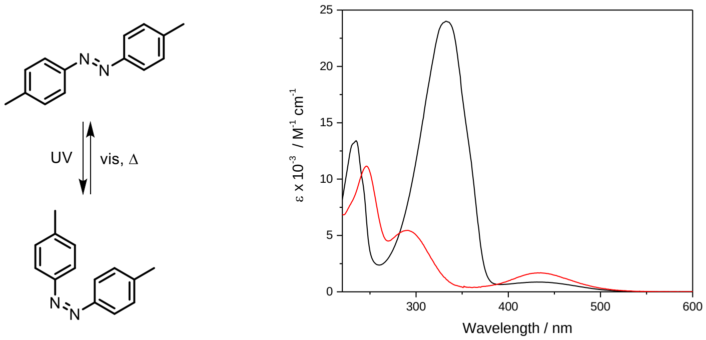

*Fig. A1: Left: molecular structure and isomerization process of **ABMe$_2$**; right: absorption spectra of the E (black line) and Z (red line) isomers of **ABMe$_2$** in MeCN.*

Upon irradiation of **ABMe$_2$** with UV light, the absorbance of the π-π* band is deeply decreased, whereas that of the n-π* arises, until the achievement of a photostationary state (PSS) (figure A2). This behaviour is ascribable to the well known *E*-*Z* photoisomerization of the central azo bond. When left in the dark, previously irradiated solutions showed a thermally accessible back-isomerization process, with a complete recovery of the *E* isomer in several days. By fitting of the absorbance values over time, the rate constant k_Δ of the thermal back-isomerization was found to be 1.6×10^{-6} s^{-1}, suggesting this process is substantially negligible in the experimental timescale.

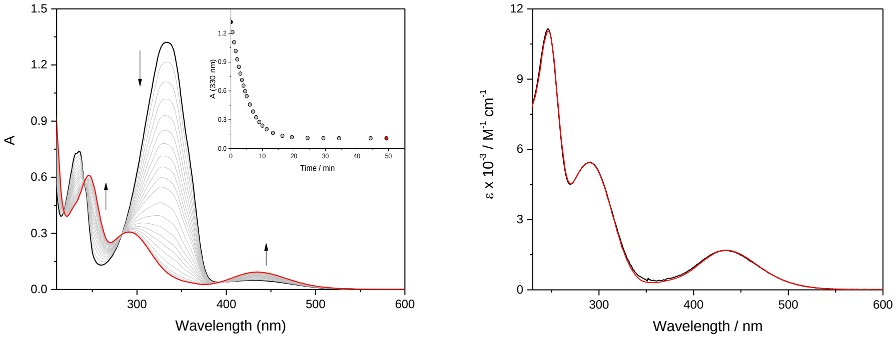

*Figure A2: Left: absorption spectra of **ABMe$_2$** upon irradiation at 365 nm; right: absorption spectra of Z-**ABMe$_2$** obtained with the Fischer Method (black line) and by subtraction (red line, see text for details).*

Determination of the spectrum of the *Z* isomer

Since the absorption spectra of the two isomers are overlapped in the whole range of wavelengths, a total conversion to the *Z* isomer is never afforded. Nevertheless, the absorption spectrum of *Z*-**ABMe$_2$** can be mathematically obtained, since irradiation at 365 nm yields a PSS approaching total conversion *(vide infra)*, through the equation (*EA1*)

$$A_{tot}^{PSS} = A_E^{PSS} + A_Z^{PSS} \qquad (EA1)$$

Where A_{tot}^{PSS} represents the absorbance of the mixture and A_E^{PSS} and A_Z^{PSS} the contribution of each isomer to the spectrum of the photostationary state. Since the amount of the two isomers is linked through the degree of photoconversion α, it can be written

$$A_{tot}^{PSS} = A_E \times (1 - \alpha) + A_Z \times \alpha \qquad (EA2)$$

where A_E and A_Z represent the absorption spectra of the pure *E* or *Z* isomer at the same analytical concentration of the experiment. A coarse estimation of α can be performed by subtracting from the *PSS* the starting spectrum (A_E) multiplied for an arbitrary value of (1 – α). When the chosen value exceeds the real value, the difference spectrum displays negative values. Thus, this method provides an upper estimation of the amount of *E*- form in the irradiated mixture. As an example, it can be stated that, upon irradiation at 365 nm, the amount of *E* form does not exceed the 5%. Subsequently, the molar absorption values can be obtained dividing the absorption spectrum by the corresponding molar fraction of the *Z* form.

Even though the above-mentioned procedure is easily and immediately applicable, it only provides an estimation of the lower limit of the photoconversion degree. Nevertheless, this value can be obtained by comparison of two photostationary states arising from irradiations at two different wavelengths, as reported by Fischer.[5] Such a method can be applied to photochromes with sufficient photo- and thermal stability, and in the sole case where the ratio between the forward and backward quantum yields is maintained at different irradiation wavelengths, within the same electronic level. Since **ABMe$_2$** displays a clean and reversible photoreaction without any evidence of irreversible photoproducts and a thermal isomerization negligible in the experimental timescales of irradiation, and, moreover, the ratio of the quantum yields is substantially unchanged in the same band this method can be applied with success. The results obtained with this procedure, applied to the photostationary states upon irradiation at 313 and 334 nm are reported in figure A2, right, and compared with the spectrum obtained through equation (*EA2*).

Determination of the photoisomerization quantum yields

Photoisomerization quantum yields of **ABMe$_2$** were calculated through fitting of the absorbance values over time, using the software Berkeley Madonna,[6] according to the photokinetic equation (*E8*).[7] The incident photon flux of the mercury lamp (q_0) was measured by means of the ferrioxalate actinometer in its "microversion",[8] as it gives reliable results both in the UV and in the visible region up to 450 nm. Fittings were carried out at the same time on the absorbance values at the irradiation wavelength, in order to compute the fraction of absorbed light, and at a wavelength where the absorbance displays large variations. Since the absorption spectrum of the *Z* form has been obtained through a mathematic data treatment and could be affected by error, the values of the absorption coefficient were allowed to be adjusted by fitting, within the experimental error. The values, measured for the three main lines of a medium-pressure mercury lamp, are reported in table A1.

λ_{irr} / nm	ε_E / M^{-1} cm^{-1}	ε_Z / M^{-1} cm^{-1}	Φ_{EZ}	Φ_{ZE}	Φ_{EZ} / Φ_{ZE}	α_Z
313	18100	3400	0.19	0.50	0.38	0.30
365	7700	400	0.18	0.16	1.12	0.95
436	900	1700	0.29	0.58	0.50	0.20

Table A1. Absorption coefficients, photoisomerization quantum yields, and photoconversion at the photostationary states of ***ABMe$_2$*** *for the main lines of a medium pressure mercury lamp.*

Despite the method reported above provides most accurate results, a possible application of **ABMe$_2$** as an actinometer requires a faster and less industrious method, thus quantum yield values were calculated by means of a simpler procedure. Firstly, the thermal process is slow and can be neglected. Moreover, below the 10% of photoconversion, it can be assumed that the amount of *Z* form does not contribute significantly to the photokinetics.[8] In other words, we assume that the *E*- isomer is the only absorbing species and the only process occurring is the *E*-*Z* photoisomerization. According to these assumptions, the equation (*E8*) can be simplified as follows:

$$\frac{d[E]}{dt} = -\frac{\Phi_{EZ} \cdot q_0 \cdot f}{V} \qquad (EA3)$$

where q_0 is the photon flux, f is the fraction of absorbed light at the irradiation wavelength, and V is the volume of the solution. The discrete form of equation (*EA3*) gives:

$$\Delta[E] = -\frac{\Phi_{EZ} \cdot q_0 \cdot \bar{f}}{V} \cdot \Delta t_{irr} \qquad (EA4)$$

where $\bar{f}$ is the mean value of absorbed light fraction and Δt is the time interval of irradiation. In its turn, the concentration can be related to the absorbance at a chosen wavelength λ_x through the difference of the absorption coefficients at the same wavelength, thus

$$\Delta[E] = \frac{\Delta A_{\lambda_x}}{\Delta \varepsilon_{\lambda_x}} = -\frac{\Phi_{EZ} \cdot q_0 \cdot \bar{f}}{V} \cdot \Delta t_{irr} \qquad (EA5)$$

In this way, it is possible to calculate the quantum yield for different intervals of irradiation, considering the difference between the absorbances of two consecutive spectra and the mean value of the two absorbed light fractions ($\bar{f}$) calculated from each spectrum. As the photoconversion increases, the calculated quantum yield decreases, since the fraction of light is not totally absorbed by the sole *E* isomer but also by the *Z*, thus, for this method, an extrapolation to t=0, *i.e.*, to the time when only *E* is present, is required.[8] The quantum yield values calculated according to this procedure are equal within the error to those obtained from the fitting of the photokinetic traces.

In order to obtain the quantum yield values for the *Z*-*E* process, the same procedure can be applied by irradiating a solution of the *Z* isomer. Usually, a complete conversion is not achieved at any wavelength of irradiation, thus the pure *Z* form is not available. In this case, the presence of a non-negligible amount of *E* form already from the starting point must be taken into account in the data treatment. Moreover, if the percentage of *E* isomer in the mixture exceeds the 10%, all the previous considerations cannot be applied. However, in the present case, irradiation at 365 nm affords a conversion larger than 95%, allowing an easier data treatment in case of irradiations at wavelengths where the photostationary states are mostly shifted to the *E*. For example, irradiation of the *Z* isomer at 436 nm produces a larger absorption variation than the irradiation of the *E* form at the same wavelength. The data fitting is simplified as the amount of Z- at the starting point can be neglected.

In summary, this high-performance derivative of azobenzene possesses good spectroscopical features and excellent photochemical properties, and therefore it could be employed as a chemical actinometer. The spectrum of the *Z* isomer was obtained through a reliable method, but it can be roughly estimated with simpler methods. Moreover, short irradiations do not require to take into account the thermal process and the absorption of the *Z* isomer, simplifying the data treatment. The optimization of an operative protocol for the use of **ABMe$_2$** as a chemical actinometer is currently underway in the research group.

References

1. H. M. D. Bandara and S. C. Burdette, *Chem. Soc. Rev.*, **2012**, *41*, 5, 1809–1825.
2. H. Rau, *Photochromism. Molecules and System*, Elsevier, Amsterdam, **1990**.
3. V. Ladányi, P. Dvořák, J. Al Anshori, Ľ. Vetráková, J. Wirz, and D. Heger, *Photochem. Photobiol. Sci.*, **2017**, *16*, 12, 1757–1761.
4. Ľ. Vetráková, V. Ladányi, J. Al Anshori, P. Dvořák, J. Wirz, and D. Heger, *Photochem. Photobiol. Sci.*, **2017**, *16*, 12, 1749–1756.
5. E. Fischer, *J. Phys. Chem.*, **1967**, *71*, 11, 3704–3706.
6. *https://berkeley-madonna.myshopify.com*.
7. K. Stranius and K. Börjesson, *Sci. Rep.*, **2017**, *7*, 41145.
8. M. Montalti, A. Credi, L. Prodi, and M. T. Gandolfi, *Handbook of Photochemistry*, 3rd ed. CRC Press, Boca Raton, **2006**.

Appendix B.

List of symbols and abbreviations

A	Absorbance
λ	Wavelength
ε	Absorption coefficient
τ	Decay time
β	Lifetime pre-exponential factor
f	Lifetime fraction of intensity
r	Anisotropy
ϕ	Anisotropy decay time
Φ	Quantum yield
α	Percentage of photoconversion
k_{Δ}	Kinetic constant of thermal process
$\supset$	Inclusion complex
q_0	Photon flux
J	Net reaction flux

24C8	[24]crown-8
CT	Charge transfer
CV	Cyclic voltammetry
DB24C8	Dibenzo-[24]crown-[8]
DBU	1,5-diazabicyclo(5.4.0)undec-5-ene

DCM	Dicyanomethylenepyran
DN24C8	Dinaphtho-[24]crown-[8]
DOV	Dioctylviologen
DPV	Differential pulse voltammetry
PhMe	Toluene
TBA	Tributylamine
TBA^+	Tetrabutylammonium
TCSPC	Time-correlated single photon counting
TfOH	Triflic acid
THF	Tetrahydrofuran
TsO^-	*p*-toluenesulphonate (tosylate)
UV	Ultraviolet

Appendix C.

List of scientific contributions

Original research papers

- L. Casimiro, S. Maisonneuve, P. Retailleau, S. Silvi, J. Xie* and R. Métivier*,
  “Photochromism and fluorescence of a DCM derivative”
  manuscript in preparation

- G. Orlandini, L. Casimiro, M. Bazzoni, B. Cogliati, A. Credi, M. Lucarini, S. Silvi*, A. Arduini* and A. Secchi*,
  “Synthesis and Properties of a Redox-switchable Calix[6]arene-based Molecular Lasso”
  Org. Chem. Front., **2020**, *accepted manuscript*

- G. Baggi, L. Casimiro, M. Baroncini, A. Credi* and S. Loeb*
  “Threading-gated photochromism in [2]-pseudorotaxanes”
  Chem. Sci., **2019**, 10, 5104-5113 - DOI: 10.1039/c9sc00913b

- M. Bazzoni, V. Zanichelli, L. Casimiro, C. Massera, A. Credi, A. Secchi*, S. Silvi* and A. Arduini*
  “New Geometries for Calix[6]arene-based Rotaxanes”
  Eur. J. Org. Chem, **2019**, 21, 3513–3524 - DOI: 10.1002/ejoc.201900211

- L. Casimiro, J. Groppi, M. Baroncini, M. La Rosa, A. Credi and S. Silvi*,
  “Photochemical investigation of cyanoazobenzene derivatives as components of artificial supramolecular pumps”
  Photochem. Photobiol. Sci., **2018**, 17, 734-740 - DOI: 10.1039/c8pp00062j

Reviews

- M. Baroncini, M. Canton, L. Casimiro, S. Corra, J. Groppi, M. La Rosa, S. Silvi and A. Credi*,
  “Photoactive molecular-based devices, machines and materials: recent

advances"
Eur. J. Inorg. Chem., **2018**, 42, 4589-4603 - DOI: 10.1002/ejic.201800923

- M. Baroncini, L. Casimiro, C. de Vet, J. Groppi, S. Silvi and A. Credi*,
  "Making and operating molecular machines: a multidisciplinary challenge"
  Chemistry Open, **2018**, 7, 169-179 - DOI: 10.1002/open.201700181

Book chapters

- M. Baroncini, M. Canton, L. Casimiro, A. Credi* and S. Silvi*,
  "Mechanically interlocked systems: photoactive rotaxanes and catenanes"
  in *Handbook of Inorganic Photochemistry*, *part E: Supramolecular Systems*, **2020**,
  N. D. McClenaghan, P. Kruger (Eds.), Springer, New York, *in press*

Conferences contributions

2019

- ISOP'2019 – International Symposium on Photochromism (Paris, France)
  "*Molecular and Supramolecular Tuning of Photochromism*", young scientist oral communication

- Giornata della luce (Bologna, Italy)
  "*Nanomacchine a energia solare*", short oral communication

2018

- Journées GDR Photo Electro Stimulation (Rennes, France),
  "*Light Responsive Nanomotors: New Components for the next generation of Supramolecular Pumps*", poster presentation

- 1ère Journée des doctorants du PPSM (Cachan, France),
  "*Light-driven nanomotors: towards new generations of supramolecular pumps*", oral communication

- 6ème Journée Scientifique du LabEx – CHARM$_3$AT (Cachan, France),
  "*Light-responsive nanomotors: new components for the next generation of supramolecular pumps*", poster presentation

- Journées de printemps de la SP2P (Bordeaux, France), "*Light-responsive nanomotors: towards new generations of supramolecular pumps*", oral communication

2017

- IPM2017- Italian Photochemistry Meeting 2017 (Perugia, Italy), "*Supramolecular tuning of photochromism in mechanically interlocked molecules*", oral communication

- XVII Giornata della Chimica dell'Emilia Romagna (Bologna, Italy), "*Supramolecular tuning of photochromism in mechanically interlocked molecules*", poster presentation

- ISNSC9 - 9th International Symposium on Nano and Supramolecular Chemistry (Napoli, Italy), "*Supramolecular tuning of photochromism in mechanically interlocked molecules*", oral communication

- ICP2017 - 28th International Conference on Photochemistry (Strasbourg, France), "*Light powered artificial molecular pumps*", oral communication

- Supramol2017 - XIII Congresso Nazionale di Chimica Supramolecolare (S. Margherita di Pula, Italy), "*Light powered artificial molecular pumps*", short oral communication

A brief Jew tale on Light

Once upon a time, when God created the world, Sun and Moon were equally shiny and used to bright the sky in turn: when Sun set, Moon rose. But Moon was not satisfied of that perpetual daylight: she wanted to reign alone in the sky, without Sun around. So, she walked on the clouds to God sitting in his golden throne. She pulled his vest and said:

- "My Lord, you have created a beautiful and stunning world. And everything in this world, has an opposite side. The man and the woman; the hot and the cold; the fire and the water; the mountains and the seas; the birds flying in the highest skies and the fishes swimming in the deepest oceans. Why, then, should Sun and I be identical? Maybe, one of us could shine less… Maybe Sun, since it was my idea…"

God smiled, pulled his hand, took a handful of Light from her and put it in his pocket. Then he said:

- "Your nice idea will be enough for you."

Moon run away in a great anger, and sat on a cloud to calm down. But when she finally looked up, she was astonished. In the night everything was beautiful: people sleeping peacefully, wolves dedicating her howling that she only could understand, lovers walking hand in hand and saying "have you seen how beautiful is the Moon tonight?". She had become the queen of the night.

But, without Sun, she felt alone. So, she walked back to God, and said:

- "My Lord, I apologize. You gave me a precious present indeed. But now I feel so lonely in the sky…"

God did not reply. He took the handful of Light from his pocket and threw it in the sky. And this is how the Stars were born.

Acknowledgements

I wish to warmly thank Serena Silvi and Alberto Credi, my PhD supervisors, and Rémi Métivier, who hosted me in his group for my research stay.

I am also grateful to Massimo Baroncini, Martina Canton, Jessica Groppi, Marcello La Rosa, Stefano Corrà and Leonardo Andreoni for their help in the experimental activities and for the enjoyable scientific interaction.

Finally, I thank our coworkers Stephen J. Loeb and Giorgio Baggi (University of Windsor), Maurizio Prato and Luka Đorđević (University of Trieste), Stéphane Maisonneuve and Juan Xie (ENS Paris - Saclay), Arturo Arduini, Andrea Secchi and Margherita Bazzoni (University of Parma) for the fruitful collaborations.

Financial support from the European Research Council (H2020 ERC Advanced Grant “Leaps” no. 692981) is gratefully acknowledged.